

METAL COMPLEXES OF ANTI-TUBERCULAR DRUGS

Thesis Presented for the Degree of

DOCTOR OF PHILOSOPHY

By

KHADIJAH TOLULOPE DAUDA (MSc)



Supervisor: Prof. Mino Caira

Co-supervisor: Prof. Graham E. Jackson

In the Department of Chemistry

UNIVERSITY OF CAPE TOWN

November 2017

The copyright of this thesis vests in the author. No quotation from it or information derived from it is to be published without full acknowledgement of the source. The thesis is to be used for private study or non-commercial research purposes only.

Published by the University of Cape Town (UCT) in terms of the non-exclusive license granted to UCT by the author.

DEDICATION

This thesis is dedicated to my husband, Abdulrahman for his support and encouragement during the postgraduate program and the composition of this thesis.

This work is also dedicated to my children, Abdulsalam, Abdulfaraaj and Yusroh for their patience throughout the course and my family for their interest and encouragement.

DECLARATION

I, Khadijah T. Dauda do sincerely and solemnly declare that “Metal Complexes of Anti-Tubercular Drugs” is my own unaided work both in concept and execution and that all sources that I have used and quoted have been indicated and acknowledged using complete and clear references. This thesis is submitted for the Doctor of Philosophy (PhD.) degree, to the Department of Chemistry, Faculty of Science, University of Cape Town, it has not been submitted for any degree or any examination at the University of Cape Town or any other university

Khadijah.T. Dauda

November 2017

ACKNOWLEDGEMENTS

I would like to express my genuine thanks and appreciation to my supervisors Professor Graham E. Jackson and Professor Mino Caira. In particular, I would like to thank them for their invaluable guidance, tremendous support, encouragement and patience throughout the course of this work.

I would also like to extend my thanks to the following:

Dr Hong Su for her invaluable assistance with the crystallographic work.

Members of staff and fellow students in the Chemistry Department (UCT).

Members of the Bio-physical Inorganic and Supramolecular group for their encouragement.

The University of Cape Town and the Faculty of Science for the financial support.

Moreover, above all, all praises and adoration to Almighty Allah (God) for giving me strength and the ability to complete this work.

CONFERENCE PROCEEDINGS

Some of the results in this thesis have been presented in the following conferences;

Proceedings of the International Conference on Pure and Applied Chemistry. Held in Mauritius, July 18th-22nd 2016. **Potentiometric Studies of Cu(II), Ni(II) and Zn(II) Complexes of isoniazid an anti-tubercular drug.**

Western Cape SACI young Chemist Symposium (SU 2016) (24th Oct. 2016) held at Stellenbosch University. **Potentiometric and Spectroscopic Studies of the Cu(II), Ni(II) and Zn(II) Complexes of ethambutol an anti-tubercular drug.**

South African Chemical Institute (SACI Inorganic 2017) (25th-29th 2017) in South Africa. **The Influence of Metals on the Permeability and Lipophilicity Properties of anti-tubercular Drugs.**

ABSTRACT

There is a continuing need to improve anti-tubercular drugs due to the development of resistance towards existing drugs. In some cases, metal complexes are known to improve the bioavailability of drugs. Hence the present study looks at the use of metal complexes of anti-tubercular drugs to improve the permeability and bioavailability of the drugs. The anti-tubercular drugs isoniazid (ISO), ethambutol (EMB), para-aminosalicylic acid (PAS), rifampicin (RFN) and pyrazinecarboxamide (PZA) were used in this study.

Since the solubility and hence permeability and bioavailability of the drugs depend on their solution speciation, the equilibrium constants for the reaction of H^+ , Cu(II), Ni(II) and Zn(II) with the ligands were measured, in aqueous solution, at $25 \pm 0.01^\circ C$ and an ionic strength of 0.15 M (NaCl) using glass electrode potentiometry.

The structures of the complexes with EMB, ISO and PAS were investigated using ultraviolet-visible spectroscopy. The visible spectra obtained for the different species of EMB in solution were typical of Cu(II) and Ni(II) complexes. The spectra found for the various species of ISO and PAS in solution were also characteristic of their Cu(II) complexes. The results from the visible spectra support the structures postulated from the potentiometric data.

This study also considered membrane permeability and absorption using a Franz cell and octanol/water partition coefficients. Partition coefficient studies showed that ISO and PZA and their complexes are hydrophilic while RFN and PAS and their complexes are lipophilic. The incorporation of a metal-ion improves the lipophilicity/hydrophilicity properties of the ligand. The presence of metal greatly enhanced the permeation of ISO through an artificial membrane in the order $Cu(II) > Zn(II) > Ni(II) > ISO$. A significant improvement was also found when Cu(II) was incorporated into the RFN system with an enhancement factor of 20. Zn(II) was

able to improve the permeation of PAS with an enhancement ratio of 2. The incorporation of Cu(II), Ni(II) and Zn(II) does not affect the flux and permeability coefficient of PZA.

Since the drugs are administered in tablet form, attempts were made to synthesise the metal complexes of the drugs in solid form. X-ray crystallography could then be used to confirm the solution structures. Co-precipitation, refluxing and mechanochemical methods (neat and liquid-assisted co-grinding) were employed to synthesise Cu(II), Ni(II) and Zn(II) complexes of the series of anti-tubercular drugs. However, despite exhaustive efforts, all experiments resulted in the formation of only physical mixtures of the reactants, as revealed by chromatographic and X-ray diffraction methods. This impelled the use of the solvothermal method as an alternative technique. ISO and PZA metal complexes were synthesised via this method. Unexpected products were obtained, as indicated unambiguously by single crystal X-ray diffraction, and a probable mechanism for their formation was postulated.

The incorporation of metals into anti-tubercular drugs has a significant influence in improving the permeability of the parent drug. It was found that the presence of Cu(II), Ni(II) and Zn(II) improved the permeability coefficient of ISO, while Cu(II) improved RFN and Zn (II) enhanced that of PAS.

LIST OF ABBREVIATIONS AND SYMBOLS

A	Absorbance
A	Area of exposed membrane
b	Length of the sample cell
C_i	Concentration of ligand in the donor phase
C	Molar concentration of solute
CSD	Cambridge Structural Database
DOTS	Directly observed therapy short course
ϵ	Molar absorptivity
E_{cell}	Electrostatic potential
EMB	Ethambutol
en	Ethylenediamine
ESTA	Equilibrium simulation for titration analysis
FTIR	Fourier transform infrared spectroscopy
GEP	Glass electrode potentiometry
ΔG	Gibbs free energy change
ΔH	Enthalpy change
I	Intensity
I_o	Intensity of light incident upon sample cell

IGRA _s	Interferon gamma release assay
ISO	Isoniazid
ISONIC	Isonicotinate
J	Flux in $\text{g cm}^{-2} \text{h}^{-1}$
K_a	Acid dissociation constant
K_p	Permeability coefficient in cm h^{-1}
K_w	Dissociation constant of water
[L]	Free ligand concentration (mol dm^{-3})
$\text{Log } \beta$	Logarithm (to base 10) of the cumulative equilibrium constant
$\text{Log } K$	Logarithm (to base 10) of the equilibrium constant
$\log K_p$	Logarithm of permeability coefficient
$\log D$	Distribution coefficient
$\log P_{\text{oct/aq}}$	Octanol/water Partition coefficient
λ_{max}	Wavelength of maximum absorption
MDR-TB	Drug resistance microbial strains
NMR	Nuclear magnetic resonance
n-bar	The formation constant
n_p	Number of titration points
n_T	Number of titrations
σ	Standard deviation

ΔP	Difference in pressure at two points
PAS	P-aminosalicylic acid
pH	$(-\text{Log}[\text{H}^+])$ -A measure of acidity or alkalinity
PXRD	Powder X-ray Diffraction
PZA	Pyrazinecarboxamide
PZONIC	2-pyrazinecarboxylate ion
Q	Quantity of ligand/complex
$Q_M\text{-bar}$	The deprotonation function
R	The universal gas constant
R_{lim}^H	The Hamilton R-limit
R_f^H	The Hamilton R-factor
RFN	Rifampicin
ΔS	Entropy change
SC	Stratum corneum
SDR	Single drug resistance
TB	Tuberculosis
T	Temperature
t	Time
T_H	Total proton concentration (mol dm^{-3})
T_L	Total concentration of the metal ion

TST	Tuberculin skin test
U_{obj}	Objective function
UV-Vis	Ultra-violet spectroscopy
WHO	World Health Organisation
XDR	Extreme drug resistance
Z_i	The charge of the ion
$Z_{\text{H-bar}}$	The protonation function
$Z_{\text{M-bar}}$	The metal formation function

LIST OF FIGURES

Figure 1.1: Map indicating TB-affected areas.....	3
Figure 1.2: Schematic representation of the mycobacterial cell wall.	6
Figure 1.3: Structure of Isonicotinic hydrazide	7
Figure 1.4: Structure of Rifampicin	8
Figure 1.5: Structure of Pyrazinecarboxamide	9
Figure 1.6: Structure of Ethambutol	9
Figure 1.7: Structure of p-aminosalicylic acid.....	10
Figure 3.1: Z_H -bar as a function of pH for the protonation of ISO.....	40
Figure 3.2: Distribution curve for the protonation of ISO.....	41
Figure 3.3: Z_M -bar as a function of pA for Cu(II) ISO complex.....	42
Figure 3.4: Q_M -bar as a function of pH for Cu(II) ISO complex.....	43
Figure 3.5: The distribution curve for the Cu(II) ISO complex.	44
Figure 3.6: Z_M -bar as a function of pA for Ni(II) ISO complex.	45
Figure 3.7: Q_M -bar as a function of pH for Ni(II) ISO complex.	45
Figure 3.8: The distribution curve for the Ni(II) ISO complex.....	47
Figure 3.9: Z_M -bar as a function of pA for Zn(II) ISO complex.....	47
Figure 3.10: Q_M -bar as a function of pH for Zn(II) ISO complex.....	48
Figure 3.11: The distribution curve for the Zn(II) ISO complex (metal to ligand ratio 1:1).....	49
Figure 3.12: Possible structures for MLH and ML of Cu(II) ISO system.....	51
Figure 3.13 Z_H -bar as a function of pH for the protonation of Ethambutol.....	52
Figure 3.14: Distribution curve for the protonation of Ethambutol.....	53
Figure 3.15: Z_M -bar as a function of pA for Cu(II) EMB complex.....	54
Figure 3.16: Q_M -bar as a function of pH for Cu(II) EMB complex.....	55
Figure 3.17: The distribution curve for the Cu(II) EMB complex (metal to ligand ratio 1:2).....	56
Figure 3.18: Z_M -bar as a function of pA for Ni(II) EMB complex.....	57

Figure 3.19: Q_M -bar as a function of pH for Ni(II) EMB complex.....	58
Figure 3.20: The distribution curve for the Ni(II) EMB complex (metal to ligand ratio 1:1).....	59
Figure 3.21: Z_M -bar as a function of pA for Zn(II) EMB complex.....	59
Figure 3.22: Q_M -bar as a function of pH for Zn(II) EMB complex.....	60
Figure 3.23: The distribution curve for the Zn(II) EMB complex (metal to ligand ratio 1:2).....	61
Figure 3.24: Possible structures for ML of Cu(II) EMB system.....	64
Figure 3.25: Possible structures for ML_2 , ML_2H_{-1} and ML_2H_{-2} of Cu(II) EMB system.....	64
Figure 3.26: Z_H -bar as a function of pH for the protonation of p-aminosalicylic acid.....	65
Figure 3.27: Distribution curve for the p-aminosalicylic acid.....	66
Figure 3.28: Z_M -bar as a function of pA for Cu(II) PAS complex.....	67
Figure 3.29: Q_M -bar as a function of pH for Cu(II) PAS complex.....	68
Figure 3.30: The distribution curve for the Cu(II) PAS complex (metal to ligand ratio 1:1).	69
Figure 3.31: Possible structures for MLH, ML and MLH_{-1} Cu(II) PAS system.....	70
Figure 4.1: UV-Visible electronic absorption spectra for Cu(II) EMB_2	78
Figure 4.2: UV-spectra of different species for the Cu(II) EMB_2 system	79
Figure 4.3: UV-Visible electronic spectra for Ni(II) EMB_2 at different pH.....	81
Figure 4.4: UV-spectra of different species for the Ni(II) EMB_2 system.....	82
Figure 4.5: UV-Visible electronic absorption spectra for Cu(II) ISO	83
Figure 4.6: Calculated spectra of Cu(II)ISO individual species.....	84
Figure 4.7: UV-Visible electronic absorption spectra for Cu(II) PAS	85
Figure 4.8: Deconvoluted spectra of Cu(II) PAS individual species.	86
Figure 4.9: $\log P_{oct/aq}$ and speciation graph as a function of pH for ISO system.....	89
Figure 4.10: $\log P_{oct/aq}$ and speciation graph as a function of pH for 1:1 Cu ISO system.....	90
Figure 4.11: $\log P_{ct/aq}$ and speciation graph Ni(ISO) system.....	91
Figure 4.12: $\log P_{oct/aq}$ and speciation graph for Zn(ISO) system.....	92
Figure 4.13: $\log P_{oct/aq}$ of RFN and its complexes as a function of pH.	93

Figure 4.14: $\log P_{\text{oct/aq}}$ of PZA and its complexes as a function of pH.....	94
Figure 4.15: $\log P_{\text{oct/aq}}$ and speciation graph as a function of pH for PAS system.....	94
Figure 4.16: $\log P_{\text{oct/aq}}$ and speciation graph Cu(PAS) system.....	95
Figure 4.17: $\log P_{\text{oct/aq}}$ of PAS complexes as a function of pH.....	96
Figure 4.18: A modified Franz diffusion cell apparatus.....	102
Figure 4.19: Variation of ISO vs time through Cerasome 9005 membrane at pH 2.00.....	104
Figure 4.20: Influence of metals on the flux of ISO through Cerasome 9005 membrane	105
Figure 4.21: Effect of metals on the permeability of ISO through Cerasome 9005 membrane.....	105
Figure 4.22: Variation in the amount of RFN vs time through Cerasome 9005 membrane.....	106
Figure 4.23: Influence of metals on the flux of RFN through Cerasome 9005 membrane.....	107
Figure 4.24: Effect of metals on the permeability of RFN through Cerasome 9005 membrane.....	108
Figure 4.25: Variation in the amount of PAS vs time through Cerasome 9005 membrane.....	109
Figure 4.26: Influence of metals on the flux of PAS through Cerasome 9005 membrane.....	110
Figure 4.27: Effect of metals on the permeability of PAS through Cerasome 9005 membrane.....	110
Figure 4.28: Variation in the amount of PZA vs time through Cerasome 9005 membrane.....	111
Figure 4.29: Influence of metals on the flux of PZA through Cerasome 9005 membrane.....	112
Figure 4.30: Effect of metals on the permeability of PZA through Cerasome 9005 membrane.....	112
Figure 4.31: Comparison of the permeability coefficient for the ligands and complexes.....	113
Figure 4.32: $\log K_p$ plotted against logarithm of partition coefficient for ISO	114
Figure 4.33: $\log K_p$ plotted against logarithm of partition coefficient for RFN.....	115
Figure 4.34: $\log K_p$ plotted against logarithm of partition coefficient for PAS.	116
Figure 4.35: $\log K_p$ plotted against logarithm of partition coefficient for PZA.....	116
Figure 4.36: $\log K_p$ plotted against $\log P$ for all ligand and complexes.....	117
Figure 4.37 $\log K_p$ plotted against MW for all ligand and complexes.....	118

Figure 5.1: The molecular structure of $\text{Cu}(\text{ISONIC})_2(\text{H}_2\text{O})_4$, labelling and thermal ellipsoids.....	136
Figure 5.2: Packing diagram illustrating principal H-bonds in $\text{Cu}(\text{ISONIC})_2(\text{H}_2\text{O})_4$	137
Figure 5.3: Experimental PXRD trace for $\text{Cu}(\text{ISONIC})_2(\text{H}_2\text{O})_4$ complex.....	138
Figure 5.4: The IR spectrum of $\text{Cu}(\text{ISONIC})_2(\text{H}_2\text{O})_4$	139
Figure 5.5: The molecular structure of $\text{Cu}(\text{PZONIC})_2$ labelling and thermal ellipsoids.....	142
Figure 5.6: A section of a polymeric unit of $\text{Cu}(\text{PZONIC})_2$	142
Figure 5.7: Layer formation based on hydrogen bonds in $\text{Cu}(\text{PZONIC})_2$	144
Figure 5.8: Experimental PXRD trace for $\text{Cu}(\text{PZONIC})_2$ complex.....	145
Figure 5.9: The IR spectrum of $\text{Cu}(\text{PZONIC})_2$	145
Figure 5.10: UV-Visible spectrum for $\text{Cu}(\text{PZONIC})_2$ in ethanol.....	146
Figure 5.11: The IR spectra of $\text{M}(\text{PZONIC})_2(\text{H}_2\text{O})_2$ complexes.....	150
Figure 5.12: Experimental PXRD trace for $\text{Ni}(\text{PZONIC})_2(\text{H}_2\text{O})_2$ complex.....	151
Figure 5.13: Experimental PXRD trace for $\text{Zn}(\text{PZONIC})_2(\text{H}_2\text{O})_2$	152
Figure 5.14: Catalytic hydrolytic reaction of pyrazinecarboxamide to pyrazine carboxylate.....	152

LIST OF TABLES

Table 3.1: Stability constants ($\log \beta_{pqr}$) for ISO (ISO) $\beta_{pqr} = [M_p L_q H_r] / [M]^p [L]^q [H]^r$, $I = 0.15 \text{ mol dm}^{-3}$ (NaCl), $T = 25 \text{ }^\circ\text{C}$	41
Table 3.2: Stability constants ($\log \beta_{pqr}$) for Cu(II) ISO $\beta_{pqr} = [M_p L_q H_r] / [M]^p [L]^q [H]^r$, $I = 0.15 \text{ mol dm}^{-3}$ (NaCl), $T = 25 \text{ }^\circ\text{C}$	44
Table 3.3: Stability constants ($\log \beta_{pqr}$) for Ni(II)ISO complex $\beta_{pqr} = [M_p L_q H_r] / [M]^p [L]^q [H]^r$, $I = 0.15 \text{ mol dm}^{-3}$ (NaCl), $T = 25 \text{ }^\circ\text{C}$	46
Table 3.4: Stability constants ($\log \beta_{pqr}$) for Zn(II)ISO complex $\beta_{pqr} = [M_p L_q H_r] / [M]^p [L]^q [H]^r$, $I = 0.15 \text{ mol dm}^{-3}$ (NaCl), $T = 25 \text{ }^\circ\text{C}$	49
Table 3.5: Equilibrium constants of the reaction of Cu(II), Ni(II) and Zn(II) with ISO.....	51
Table 3.6: Stability constants ($\log \beta_{pqr}$) for Ethambutol (EMB) $\beta_{pqr} = [M_p L_q H_r] / [M]^p [L]^q [H]^r$, $I = 0.15 \text{ mol dm}^{-3}$ (NaCl), $T = 25 \text{ }^\circ\text{C}$	53
Table 3.7: Stability constants ($\log \beta_{pqr}$) for Cu(II) EMB complex $\beta_{pqr} = [M_p L_q H_r] / [M]^p [L]^q [H]^r$, $I = 0.15 \text{ mol dm}^{-3}$ (NaCl), $T = 25 \text{ }^\circ\text{C}$	56
Table 3.8: Stability constants ($\log \beta_{pqr}$) for Ni(II) EMB complex $\beta_{pqr} = [M_p L_q H_r] / [M]^p [L]^q [H]^r$, $I = 0.15 \text{ mol dm}^{-3}$ (NaCl), $T = 25 \text{ }^\circ\text{C}$	59
Table 3.9: Stability constants ($\log \beta_{pqr}$) for Zn(II) EMB complex $\beta_{pqr} = [M_p L_q H_r] / [M]^p [L]^q [H]^r$, $I = 0.15 \text{ mol dm}^{-3}$ (NaCl), $T = 25 \text{ }^\circ\text{C}$	61
Table 3.10: Equilibrium constants of the reaction of Cu(II), Ni(II) and Zn(II) with EMB.....	62
Table 3.11: Stability constants ($\log \beta_{pqr}$) for p-aminosalicylic acid (PAS) $\beta_{pqr} = [M_p L_q H_r] / [M]^p [L]^q [H]^r$, $I = 0.15 \text{ mol dm}^{-3}$ (NaCl), $T = 25 \text{ }^\circ\text{C}$	66
Table 3.12: Stability constants ($\log \beta_{pqr}$) for Cu(II) PAS complex $\beta_{pqr} = [M_p L_q H_r] / [M]^p [L]^q [H]^r$, $I = 0.15 \text{ mol dm}^{-3}$ (NaCl), $T = 25 \text{ }^\circ\text{C}$	68
Table 3.13: Equilibrium constants of the reaction of Cu(II) with PAS.....	69
Table 4.1: UV-Vis spectra ϵ_{max} ($\text{dm}^3 \text{ mol}^{-1} \text{ cm}^{-1}$) and λ_{max} (nm) exp. and calc. values with possible donor groups for Cu(II) EMB complexes.....	80
Table 4.2: UV-Vis spectra ϵ_{max} ($\text{dm}^3 \text{ mol}^{-1} \text{ cm}^{-1}$) and λ_{max} (nm) exp. and calc. values with possible donor groups for Ni(II) EMB complexes.....	82
Table 4.3: Permeability coefficients obtained through human skin ($\log K_p$) and silicone membrane using diffusion cell ($\log K_{p(\text{sil})}$).....	101
Table 4.4: Flux of diffusion J ($\text{mg cm}^{-2} \text{ h}^{-1}$) and permeability coefficient K_p (cm h^{-1}) of ISO.....	104
Table 4.5: Flux of diffusion J ($\text{mg cm}^{-2} \text{ h}^{-1}$) and permeability coefficient K_p (cm h^{-1}) of RFN.....	107
Table 4.6: Flux of diffusion J ($\text{mg cm}^{-2} \text{ h}^{-1}$) and permeability coefficient K_p (cm h^{-1}) of PAS.....	109
Table 4.7: Flux of diffusion J and permeability coefficient K_p of PZA.....	111

Table 4.8: The permeability and partition coefficient values of the ISO	114
Table 4.9: The permeability and partition coefficient values of the RFN	116
Table 4.10: The permeability and partition coefficient values of the PAS	115
Table 4.11: The permeability and partition coefficient values of the PZA	116
Table 5.1: Crystal data and details of refinement.....	134
Table 5.2: Selected bond lengths (Å) and angles (°) for Cu(ISONIC) ₂ (H ₂ O) ₄	136
Table 5.3: Hydrogen bond data (distances in Å, angles in degrees) for Cu(ISONIC) ₂ (H ₂ O) ₄	136
Table 5.4: The frequencies (in cm ⁻¹) and assignments of vibrations of ISONIC and its complex.....	139
Table 5.5: Crystal data and details of refinement.....	141
Table 5.6: Selected bond lengths (Å) and angles (°) for Cu(PZONIC) ₂	143
Table 5.7: Hydrogen bond data (distances in Å, angles in degrees)	144
Table 5.8: FTIR spectra of PZONIC and Cu(PZONIC) ₂	146
Table 5.9: Elem. analy. data for attempted synthesis of Ni ²⁺ and Zn ²⁺ PZA	148
Table 5.10: Comparative crystal data for M(PZONIC) ₂ (H ₂ O) ₂ complexes.....	149
Table 5.11: FTIR frequencies in (cm ⁻¹) and assignments for M(PZONIC) ₂ (H ₂ O) ₂ complexes.....	150

TABLE OF CONTENTS

DEDICATION	ii
DECLARATION	iii
ACKNOWLEDGEMENTS	iv
CONFERENCE PROCEEDINGS	v
ABSTRACT	vi
LIST OF ABBREVIATIONS AND SYMBOLS.....	viii
LIST OF FIGURES.....	xii
LIST OF TABLES.....	xvi
TABLE OF CONTENTS.....	xviii
Chapter 1- Introduction	1
1.1 Introduction	2
1.2 Pathogenesis.....	4
1.3 Diagnosis.....	4
1.4 Anti-Tuberculosis Chemotherapy	5
1.4.1 Isoniazid	7
1.4.1.1 Mechanism of action.....	7
1.4.2 Rifampicin	7
1.4.2.1 Mechanism of action	8
1.4.3 Pyrazinocarboxamide.....	8
1.4.3.1 Mechanism of action	9
1.4.4 Ethambutol	9
1.4.4.1 Mechanism of action	10
1.4.5 P-aminosalicylic acid (PAS).....	10
1.4.5.1 Mechanism of Action	10
1.5.1 Problems of Present Anti-Tubercular Drugs	10
1.5.1.1 Nanoparticles in Anti-TB Delivery:.....	11
1.5.1.2 Immune-Modulator in TB Therapy:	11
1.6 Transition metal complexes in medicine	12
1.7 Aim of the Present Research.....	12
1.8 Objectives.....	12
References:	14
Chapter 2- Literature review.....	19
2.0 Transition metal complexes as potential therapeutic agents:.....	20

2.1 Metal ion complexes of anti-TB agents	20
References:	25
Chapter 3- Glass electrode potentiometry	27
3.1 Glass Electrode Potentiometry	28
3.2 Theory	29
3.3 Data Analysis	32
3.3.1 The Electrode Cell	37
3.4 Experimental	38
3.4.1 Preparation of Solutions	38
3.4.2 Potentiometric Measurement	40
3.5 Results	40
3.5.1 Isoniazid (ISO).....	40
3.5.1.1 Protonation	40
3.5.1.2 Copper complexation.....	42
3.5.1.3 Nickel complexation.....	45
3.5.1.4 Zinc complexation	47
3.5.1.5 Discussion.....	50
3.5.2 Ethambutol (EMB).....	52
3.5.2.1 Protonation	52
3.5.2.2 Copper complexation.....	54
3.5.2.3 Nickel complexation.....	57
3.5.2.4 Zinc complexation	60
3.5.2.5 Discussion.....	62
3.5.3 P-aminosalicylic acid (PAS).....	65
3.5.3.1 Protonation	65
3.5.3.2 Copper complexation.....	67
3.5.3.3 Discussion.....	69
References:	71
Chapter 4- Spectroscopy and Bioavailability Studies.....	74
4.1 UV-Visible spectroscopy.....	75
4.1.1 Introduction	75
4.1.2 Theory	75
4.1.3 Experimental	77
4.1.4 Results and Discussion	77
4.1.4.1 Cu(II) EMB-System	77
4.1.4.2 Ni(II) EMB-System	80

4.1.5.1 Cu(II) ISO-System.....	83
4.1.6.1 Cu(II) PAS-System.....	84
4.2 Dermal Absorption Study.....	87
4.2.1 Introduction	87
4.2.2. Octanol/Water Partition Coefficients	87
4.2.3 Experimental.....	89
4.2.4 Results and Discussion	89
4.2.4.1 Isoniazid	89
4.2.4.2 Cu-Isoniazid Complex.....	90
4.2.4.4 Zn-Isoniazid Complex	91
4.2.4.5 Rifampicin and its Metal Complexes.....	92
4.2.4.6 Pyrazinecarboxamide and its Metal Complexes	93
4.2.4.7 P-aminosalicylic acid	94
4.2.4.8 P-aminosalicylic acid-Cu(II) complex.....	95
4.2.4.9 P-aminosalicylic acid and its Ni(II) and Zn(II) complexes	96
4.3 Conclusion.....	98
4.4 Franz Diffusion Cells.....	99
4.4.1 Introduction	99
4.4.2 Experimental.....	103
4.4.3 Results and Discussion	103
4.4.3.1 Isoniazid and its Metal Complexes.....	103
4.4.3.2 Rifampicin and its Metal Complexes.....	106
4.4.3.3 P-aminosalicylic acid and its Metal Complexes	108
4.4.3.4 Pyrazinecarboxamide and its Metal Complexes	111
4.4.3.5 Comparison of permeability coefficients K_p for the ligands and complexes.	113
4.4 Relationship between logarithm of permeability coefficient $\log K_p$ and octanol/water partition coefficient $\log P_{oct/aq}$ of the ligand and complexes.....	114
4.5 Conclusion.....	120
References:	122
Chapter 5- Solid-state studies.....	128
5.1 Introduction	129
5.2 Methodology.....	130
5.2.1 Elemental analysis.....	130
5.2.2 X-ray Diffraction	130
5.2.2.1 Single crystal X-ray diffraction	130
5.2.2.2 Powder X-ray diffraction (PXRD).....	131

5.3 Fourier transform infrared (FTIR) spectroscopy	132
5.4. UV- Vis Spectroscopy	132
5.5. Attempted synthesis of a Cu-isoniazid complex	132
5.5.1 Synthesis	132
5.5.1.1 X-ray data and structure determination	133
5.5.1.2 PXRD Data	137
5.5.1.3. Infrared Spectral Data	138
5.4. Attempted synthesis of a Cu – pyrazinecarboxamide complex.....	140
5.4.1. Synthesis	140
5.4.1.2 PXRD Data	144
5.4.2 Infrared Spectral Data	145
5.4.3 UV-Visible spectroscopy.....	146
5.5 Attempted Synthesis of Ni ²⁺ and Zn ²⁺ -Pyrazinecarboxamide Complexes.....	147
5.5.1 Infrared Spectral Data	149
5.5.2. PXRD.....	151
5.6 Rationalisation of isolation of unexpected products	152
5.6 Conclusion.....	154
References:	156
Chapter 6- Concluding remark.....	159
6.1 Conclusion.....	160
References:	166

Chapter 1

Introduction

1.1 Introduction

Tuberculosis (TB) is a global health problem that results in several million deaths annually worldwide.¹ It is the leading cause of death by a single treatable infectious disease killing approximately 5000 people per day throughout the world as the World Health Organisation (WHO) reported 1.8 million deaths due to TB in 2008. The burden of TB is particularly high in Africa where the case rate was reported to be 281 per 100 000 people.²

The TB problem is inequitably distributed among men and women. Of the predicted 8.7 million TB cases and 1.4 million deaths caused by TB globally in 2011, about one-third occurred among women (2.9 million TB cases and 0.5 million deaths).¹ The scientific community has recognised that gender-related differences in health may be higher than is acknowledged and thus necessitate the need for routine gender-correlated study.³⁻⁵

The WHO has proposed a framework and priorities for research on sex and TB to address the knowledge gap.⁶ The WHO has also reinforced approaches of analysing the role of gender in health, and to evaluate and address, harmonising gender-related health disparities.⁷

Currently, the question of whether the gaps are due to sex-related difference, social, cultural practices and different social role of men and women or both have been studied.^{8,9} Numerous reviews have studied gender-linked barrier and delay in seeking TB care.¹⁰⁻¹³ According to studies, some of the contributing reasons that make women experience more obstacles and a longer delay than men include individual financial level, stigma and lower health literacy in south-east Asia.

Over 500 000 children were identified with TB in 2012, and 74 000 died.¹⁴ Diagnosing TB is highly challenging in children because of the production of the insufficient sputum sample. Less than 15% of the TB in children are acid-fast smear-positive. 30-40% of the cases are cultured confirmed.¹⁵ The risk of TB is high among the population living in poverty, low

socioeconomic groups, low-income, immune suppressed and extreme age (elderly and children) groups, migrants and people exposed to animals. Much of this morbidity and mortality of TB occurs in children, contributing to the number of TB cases in the future.

In developing countries, TB is a leading cause of death.¹⁶ An important associated problem is the alarming increase of drug resistant microbial strains (MDR-TB) that makes difficult the effective control of the disease. To further complicate the matter, drug-drug interactions between TB medicines and anti-HIV treatments or other chronic illness medications such as those used in people with diabetes should also be considered.¹⁷⁻²¹ This has escalated the treatment of TB in the past decades. Due to this critical situation, innovation in TB drug discovery and evolving strategies to bring a new agent with the best performance is a current health priority.²² Areas in which TB is prevalent are shown in Figure 1.1.

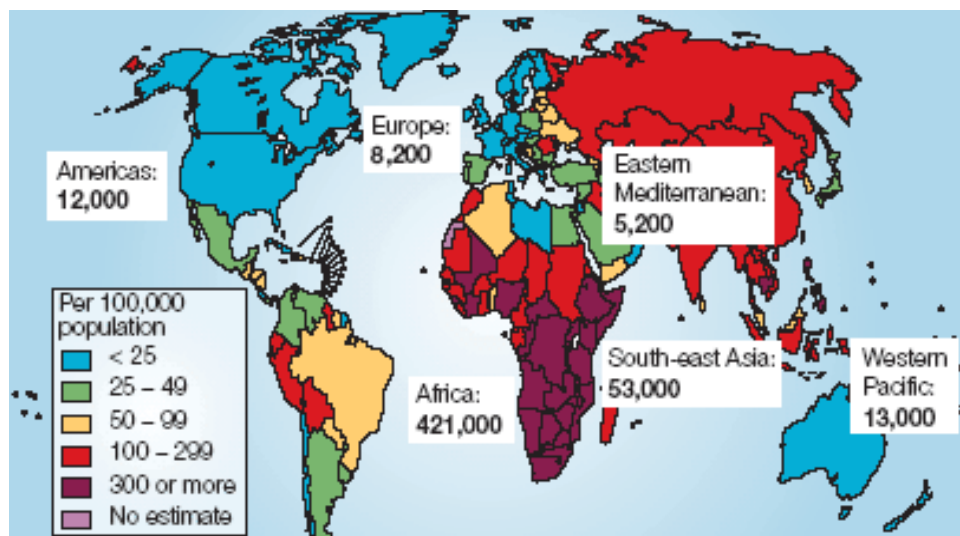


Figure 1.1 Map indicating TB-affected areas.¹

1.2 Pathogenesis

TB is an ancient disease; the causative agent is *Mycobacterium tuberculosis*. It predominantly affects the lungs, but it can also affect organs in the central nervous system, lymphatic system, and circulatory system among others.²³ TB is transmitted mostly through airborne spread via the respiratory route when a patient coughs or sneezes. One strain of TB, *Mycobacterium Bovis*, can be caused by drinking un-boiled milk.²⁴ TB is categorised as being either latent or active. In latent TB, the bacteria are inactive but present in the body. The patient has no symptoms and is not contagious. In active TB, the bacteria make the patient ill and are infectious. About 10% of people with latent TB develop active TB years after the initial infection. This active TB occurs when the immune system is weakened, for example by chemotherapy. The symptoms of TB range from no symptoms (latent TB) to symptoms of active disease. In fact, latent TB is not obvious or detectable until a skin test is done, perhaps during a routine test. Symptoms of active TB include an overall sensation of feeling unwell, cough possibly with bloody mucus, fatigue, shortness of breath, weight loss, slight fever, night sweat and pain in the chest. Symptoms of TB can be confused with symptoms of other diseases. Bloody mucus, for example, can be an indication of bronchitis or pneumonia. An evaluation by a doctor is the key to confirming whether it is latent, active TB or some other condition.

1.3 Diagnosis

Several test methods can be used to detect tuberculosis, depending on the tuberculosis type suspected and the resources available for testing. TB disease is recognised by a positive tuberculin skin test (TST) result, epidemiologic evidence and a well-matched clinical and radiological presentation.²⁵ For years TST was the only test available to diagnose latent TB. Lately, the whole blood interferon-gamma release assay (IGRAs) was introduced. The benefit

of the new technique over the skin test is that only a visit is required, unlike TST, where two visits are essential.

1.4 Anti-Tuberculosis Chemotherapy

The prime goal of anti-tuberculosis treatment includes the rapid killing of actively multiplying bacilli, prevention of acquired drug resistance, and sterilisation of infected host tissue to prevent clinical relapse. One approach to obtaining new antimycobacterial drugs is the development of new molecules by modifying old drugs with the aim to improve the antimycobacterial activity and to obtain better resistance profiles, availability and tolerability, among others.²⁶

The first-line anti-TB drugs, usually administered at the onset of the disease, are isoniazid, rifampicin, streptomycin and pyrazinamide.²⁷ These drugs are effective, but the problem is that the bacterium often develops drug resistance because of spontaneous genetic mutations involving the molecular targets of the drugs.²⁸ The single-drug-resistant (SDR) and multi-drug resistant strains of *M. tuberculosis* have led to the resort of second-line drugs which are ciprofloxacin, ethionamide, kanamycin and p-aminosalicylic acid.²⁹ These drugs, unfortunately, have adverse side effects. Hence there is a need for new or modified drugs which can overcome bacterial resistance and at the same time have fewer side effects. The WHO aims to treat 80% of the MDR-TB cases by 2015. Without unique, simple and inexpensive treatment, this is impossible.

Mycobacteria are organisms that require oxygen to grow (aerobic), non-motile, and they have an outer layer.³⁰ The cell wall of *Mycobacterium* species (Figure 1.2) is very thick, hydrophobic, waxy and rich in mycolic acids. The cell wall comprises the hydrophobic mycolate layer and a peptidoglycan layer held together by a polysaccharide, arabinogalactan.³⁰

The cell wall makes a significant contribution to the rigidity of the bacteria. The biosynthetic pathways of cell components are potential targets for new anti-tubercular drugs.

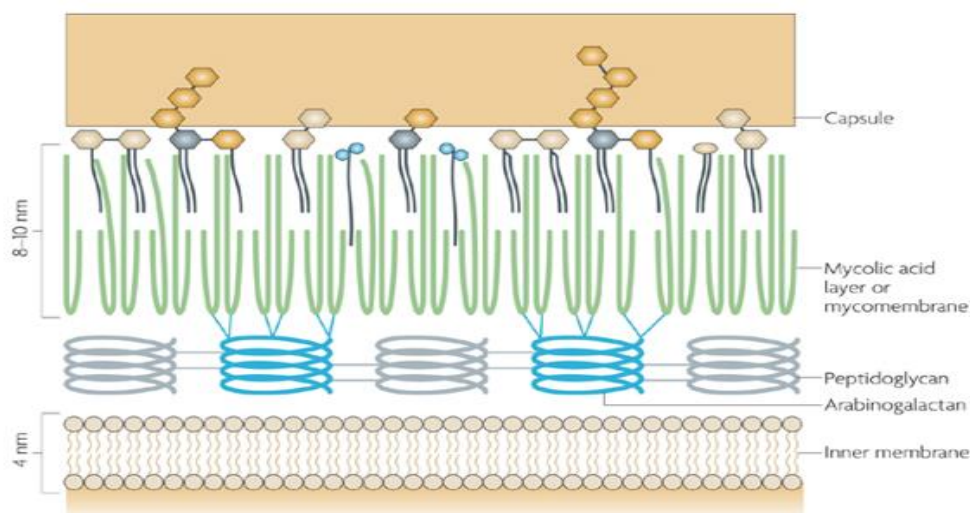


Figure 1.2: Schematic representation of the mycobacterial cell wall.³¹

In the fight against tuberculosis, permeation of chemotherapeutic agents into the cell wall remains a severe and major challenge.³² The lipophilic nature of the cell wall makes the crossing of hydrophilic molecules difficult, which is a major concern as this can lead to drug resistance.³² The directly observed therapy short course (DOTS) developed by the WHO is strategised to optimise response and adherence to TB treatment. The DOT therapy is used for the treatment of TB; it is the combination of first-line drugs such as ISO, EMB, RFN and PZA prescribed for two months, followed by ISO and PZA for the next 4-5 months.³³ The second-line drugs are considered for the reason that includes route of administration, cost, and availability.³⁴ The three broad actions of anti-tuberculosis drugs are bactericidal action, sterilising action and prevention of emergence of bacillary resistance to medication.³⁵ The mechanisms of these widely used drugs are discussed in the following sections.

1.4.1 Isoniazid

ISO (isonicotinic acid hydrazide) is the current first-line medication that has been the most frequently used anti-tuberculosis drug since acknowledgement of its activity in 1952.³⁶ It consists of a pyridine ring and a hydrazide group (Figure 1.3). ISO is a nicotinamide analogue, structurally related to the anti-tuberculosis drugs ethionamide and PZA. Since it has significant bactericidal activity, it has become an important part of the first-line anti-tuberculosis regimens, although in the last two decades resistance to ISO has been reported with increasing frequency.

ISO remains a commonly used active first-line agent for the treatment of latent tuberculosis.³⁷

Its efficacy is more than 90% in latent TB if treatment is completed properly.³⁸

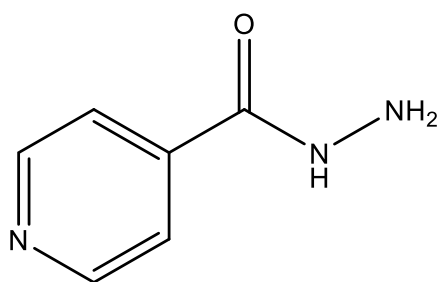


Figure 1. 3: Structure of isonicotinic hydrazide.

1.4.1.1 Mechanism of action

ISO appears to penetrate host cells rapidly³⁹ and diffuses across the *M. tuberculosis* membrane.^{40,41} ISO is a prodrug, requiring oxidative activation by the *M. tuberculosis* catalase-peroxidase enzyme called KatG.⁴² It primarily works by inhibiting the formation of mycolic acid in the cell wall of *M. tuberculosis*. It is active against fast-growing populations of the bacteria.

1.4.2 Rifampicin

Rifampicin (Figure 1.4) was first isolated in 1957 from *Ammycolatopsis* (formally *Streptomyces*) as part of an Italian screening programme.^{43,44} It is a much more complicated molecule and is

used in conjunction with ISO for active TB. Their incorporation into the standard anti-tuberculosis regimen permitted reduction of treatment from 18 to 9 months. Rifampicin is said to bind to DNA-dependent RNA polymerase and hinder initiation of RNA synthesis.⁴⁵

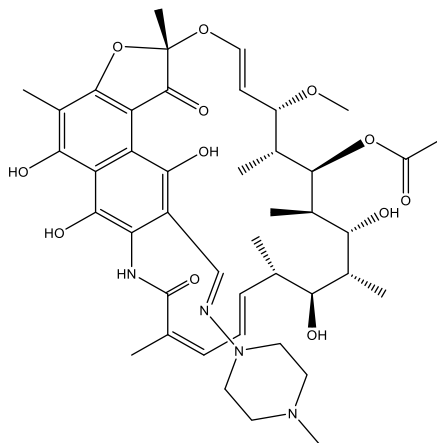


Figure 1.4: Structure of Rifampicin.

1.4.2.1 Mechanism of action

RFN contains an aromatic nucleus linked on both sides by an aliphatic bridge. The rifamycins easily diffuse across the *M. tuberculosis* cell membrane owing to their lipophilic profile.⁴⁶ They are active against bacteria with sprouts metabolism, dominant with irregular short, active period of metabolism or growth. Their bactericidal activity has been ascribed to their ability to encode DNA-dependent RNA polymerase and inhibit initiation of RNA synthesis.

1.4.3 Pyrazinecarboxamide

Since the discovery of pyrazinecarboxamide (PZA, Figure 1.5) in 1952 and its use to treat TB, the duration of treatment essential to attain acceptable relapse rates has been reduced from 9-12 months to the current six months. PZA has bactericidal activity inferior to that of ISO and RFN.⁴⁷ The possible sterilising activity and treatment-shortening potential of PZA are attributed to the drug's exceptional ability to target semi-dominant populations of bacilli

present within an acidic environment.⁴⁸ It is one of the essential medicines needed for basic health.⁴⁹

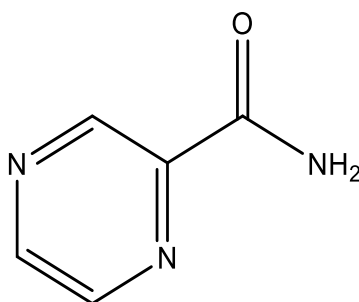


Figure 1. 5: Structure of Pyrazinecarboxamide.

1.4.3.1 Mechanism of action

PZA is a prodrug which inhibits the growth of *M. tuberculosis*. It is an amide derivative of pyrazine-2-carboxylic acid and nicotinamide analogue. PZA diffuses into the granula of *M. tuberculosis* where the pyrazinamidase converts the PZA to the active form pyrazinoic acid. The active form of pyrazinoic acid is linked to the disruption of the energetic membrane and inhibits membrane transport in *M. tuberculosis*.⁵⁰

1.4.4 Ethambutol

Ethambutol (EMB; Dextro-2,2'-(ethylenediimino)-di-1-butanol) was originally reported to have an anti-tuberculosis activity in 1961.⁵¹ EMB together with ISO, RFN, and PZA forms the modern-day short-course for the treatment of drug-susceptible TB. Like ISO, EMB primarily kills actively multiplying bacilli and has poor sterilising activity.⁵² EMB is a synthetic oral antibiotic derivative of ethylenediamine which contains two amine groups and two butanol groups (Figure 1.6).

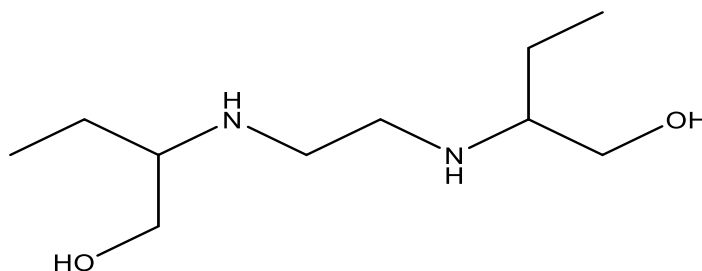


Figure 1.6: Structure of Ethambutol.

1.4.4.1 Mechanism of action

The primary pathway inhibited by EMB is the synthesis of arabinan in the cell wall of *M. tuberculosis*.^{53,54} EMB is active against the fast-growing population and mainly used to minimise ISO resistance.

1.4.5 P-aminosalicylic acid (PAS)

Lehmann discovered p-aminosalicylic acid (Figure 1.7) in 1943. PAS is used primarily as a second-line drug to treat MDR TB.⁵⁵ The emergence of resistance of *M. tuberculosis* to the first-line antibiotics has renewed the interest in second-line anti-tubercular agents.

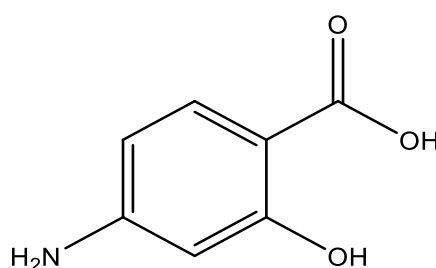


Figure 1.7: Structure of para-aminosalicylic acid.

1.4.5.1 Mechanism of Action

PAS is thought to inhibit folic acid biosynthesis, and uptake of iron.⁵⁶ PAS inhibits the growth of tubercle bacilli by impairment of folate synthesis and inhibition of iron absorption.⁵⁷ It is bacteriostatic against *M. tuberculosis*.⁵⁸

1.5.1 Problems of Present Anti-Tubercular Drugs

There are several major problems related to the presently existing TB treatments, in the first instance the length of time and complexity of therapy resulting in nonadherence to treatment. This leads to suboptimal response, the advent of resistance and continuous spread of the disease.⁵⁹ Secondly, the contrary events in response to anti-TB drugs are common and contribute to the problem of nonadherence.⁶⁰ The third problem is the increasing incidence of multidrug-resistance (MDR; resistance to at least RFN and ISO) and extensive drug-resistance

(XDR; MDR resistance plus resistance to a fluoroquinolone and an aminoglycoside).⁶¹ Fourthly, coinfection of TB and HIV is a problem by itself.⁶²⁻⁶⁴ The joint treatment of TB and HIV involves the use of drugs with related adherence difficulties and overlying toxicity profiles.^{65,66} Obviously, there is a crucial need to improve the existing drugs or introduce new drugs. Possible new drugs should decrease treatment time and have satisfactory tolerability profile.

1.5.1.1 Nanoparticles in Anti-TB Delivery:

A literature review outlining the problems in assessing the treatment and adherence towards anti-TB therapy reports that the patient compliance to the current multi-drug regimen is poor and this leads to the further progression of the disease condition.⁶⁷ The lack of compliance is a result of the prolonged treatment period and high daily dose count which also increase the drug-related toxicity. One of the major ways to achieve good compliance rate is either to reduce the overall period of drug usage or to simplify the daily pill count. Compliance can be accomplished by incorporating sophisticated formulation techniques. Encapsulating the anti-TB drugs within microparticles or nanoparticles can significantly enhance the bioavailability of the drugs and thereby reduce the frequency of the administration. This type of drug encapsulation acts as a drug reservoir and slowly releases the drug over a prolonged period.⁶⁷

1.5.1.2 Immune-Modulator in TB Therapy:

In several other bacterial infections, the period necessary to treat the disease is comparably less because once the drug initiates the killing of the bulk of the bacilli, the host immune system can take care of the remaining bacilli. The reverse is the case in TB bacteria. The TB bacteria weaken the host immune system.⁶⁸ There are some well-known TB antigens which can influence the host immune system^{69,70} and thereby make it incapable of fighting off residual bacteria on its own. To avoid this situation, the incorporation of immune-modulators in the treatment regime for TB seems to be a logical option.

1.6 Transition metal complexes in medicine

Metal ion plays an important role in biology and has led to the development of a huge number of metal complexes with various therapeutic activities. The developments in the field of chemistry provide better opportunities to use metal complexes as therapeutic agents. Metal complexes have shown promising outcomes in the treatment of diseases like diabetes, ulceration, rheumatoid arthritis and inflammatory and cardiovascular diseases.⁷¹

1.7 Aim of the Present Research

This aim of this project was to develop metal complexes of anti-tubercular drugs that have enhanced membrane permeability relative to the parent drugs and hence possibly higher bioavailability and thus be more effectual against resistant TB strains.

1.8 Objectives

The objectives were as follows:

- To study metal complex equilibria using glass electrode potentiometry.
- To determine the structures of the complexes in solution using UV-Vis spectroscopy.
- To measure the lipophilicity and hydrophilicity of the complexes using octanol/water partition coefficients.
- To assess the permeability of metal complexes using Franz cell diffusion measurements.

- To establish the structures of the metal complexes in the solid state using a variety of techniques (elemental analysis, FTIR spectroscopy, single crystal and powder X-ray diffraction).

References:

1. World Health Organization, Global Tuberculosis Report, 2012, Geneva Switzerland.
2. World Health Organization, Global Tuberculosis Report 2015, Geneva Switzerland.
3. L. Nieuwenhoven and I. Klinge, *Res. J. Women's Health*, 2010, **19**, 313-321.
4. Taking sex into account in medicine, *Lancet*, 2011, **378**, 1826.
5. S. Heidari, Q. A. Karim, J. D. Auerbach, S. E. Buitendijk, P. Cahn, M. J. Curno, C. Hankins, E. Katabira, S. Kippax, R. Marlink, J. Marsh, A. Marusic, H. M. Nass, J. Montaner, E. Pollitzer, M. T. Ruiz-Cantero, L. Sherr, P. S. Sow, K. Squires and M. A. Wainberg, *J. Int. AIDS Soc.*, 2012, **15**, 11-13.
6. World Health Organization, Gender and tuberculosis, Gender and Health Research series, 2004. Geneva Switzerland.
7. World Health Organization, Strategy for Integrating Gender Analysis and Action into the Work of WHO, 2009, Geneva Switzerland. Accessed at www.who.int/gender/en. (accessed May 2017).
8. A. Thorson and V. K. Diwan, *Curr. Opin. Pulm. Med.*, 2001, **7**, 165-169.
9. C. B. Holmes, H. Hausler and P. Nunn, *Int. J. Tuberc. Lung Dis.*, 1998, **2**, 96-104.
10. B. Vissandjee and M. Pai, *Int. J. Public Health Res.*, 2007, **52**, 199-201.
11. J. O. Ogden, S. Rangan and M. Uplekar, *Int. J. Tuberc. Lung Dis.*, 1999, **3**, 855-861.
12. M. W. Uplekar, S. Rangan, M. G. Weiss, J. Ogden, M. W. Boorgdorff and P. Hudelson, *Int. J. Tuberc. Lung Dis.*, 2001, **5**, 220-224.
13. D. G. Storla, S. Yimer and G. A. Bjune, *BMC Public Health*, 2008, **8**, 15.
14. V. Kumar, A. K. Abbas, N. Fausto and R. N. Mitchell, *Robins Basic Pathology*, Saunders Elsevier, Philadelphia Pa, USA, 8th edition, 2007.
15. J. R. Starke, *Tuberculosis*, 2003, **83**, 208-12.
16. K. Zaman, *J. Health Popul. Nutr.*, 2010, **28**, 111-113.

17. A. Koul, E. Amoult, N. Lounis, J. Guillemont and K. Andries, *Nature*, 2011, **465**, 483-490.
18. Y. D. Mukadi, D. Maher and A. Harries, *AIDS*, 2001, **15**, 143-152.
19. C. R. Stevenson, N. G. Fourouhi, G. Roglic, B. G. Williams, J. A. Lauer, C. Dye and N. Unwin, *BMC Public Health*, 2007, **7**, 234-241.
20. B. Alisjahbana, E. Sahiratmadja, E. J. Telwan, A. M. Purwa, Y. Ahmad, T. H. M. Ottenhoff, R. H. H. Nelwan, I. Parwati, J. W. M. Van der Meer and R. V. Crevel, *Clin. Infect. Dis.*, 2007, **45**, 428-435.
21. C. Y. Jeon and M. B. Murray, *PLoS Med.*, 2008, **5**, e152.
22. M. C. S. Lourenco, M. L. Ferreira, M. V. Souza, M. A. Peralta, T. R. Vasconcelos and M. G. O. Henriques, *Eur. J. Med. Chem.*, 2008, **43**, 1344-1347.
23. D. Bhowmik, Chiranjib, R. M. Chandira, B. Jayakar and K. P. S. Kumar, *J. Chem. Pharm. Res.*, 2009, **1**, 113-133.
24. F. Biet, M. L. Boschiroli, M. F. Thorel and L. A. Guilloteau, *Vet. Res.*, 2005, **36**, 411-436.
25. L. Richeldi, *Am. J. Respir. Crit. Care Med.*, 2006, **174**, 736-742.
26. M. E. Wolff. *Burger's Medicinal Chemistry and Drug Discovery*, Vol. **2**. John Wiley & Sons. Laguna Beach, 1996.
27. R. Maccari, R. Ottana, F. Monforte and M. G. Vigorita, *Antimicrob. Agents Chemother.*, 2002, **46**, 294-299.
28. A. A. Marcos, C. L. Marília, H. R. Siqueira and F. A. Mello, *J. Bras. Pneumol.*, 2010, **36**, 626-640.
29. M. Niederweis, O. Danilchnka, J. Huff, C. Hoffmann and H. Engelhardt, *Trends Microbiol.*, 2010, **18**, 109-16.

30. V. P. Myneedu, R. Singhal, K. U. Khayyam, P. P. Sharma, M. Bhalla, D. Behera and R. Sarin, *J. Epidemiol. Glob. Health*, 2015, **5**, 365-73.
31. A. M. Abdallah, N. C. Grey van Pittius, P. A. Digiuseppe Champion, J. Cox, J. Luirink, M. J. E. Vandenbroucke-Grauls, B. J. Appelmelk and W. Bitter, *Nat. Rev. Microbiol.*, **5**, 883-891.
32. V. Jarliera and H. Nikaido, *Fems Microbiol. Lett.*, 1994, **123**, 11-18.
33. N. Rastogi, E. Lagrand and C. Sola, *Rev. Sci. Tech. Off. Int. Epiz.*, 2001, **20**, 21-54.
34. C. Dye, *Lancet*, 2006, **367**, 938-940.
35. M. A. Aziz, A. Wright, A. Laszlo, A. De Muynak, F. Portaels, A. Van Deun, C. Wells, P. Null, L. Blanc and M. Raviglione, *Lancet*, 2006, **368**, 2142-2154.
36. D. A. Mitchison, *Am. J. Respir. Crit. Care Med.*, 2005, **171**, 699-706.
37. U. A. Boelsterli and K. K. Lee, *J. Gastroenterol. Hepatol.*, 2014, **29**, 678-687.
38. Q. A. Acton, Latent Tuberculosis: New Insights for the Healthcare Professional, (2011 ed., Scholarly Paper), Scholarly Editions (2012).
39. E. H. Robizek, and I. J. Selikoff, *Am. Rev. Tuberc.*, 1952, **65**, 402-428.
40. G. B. Mackaness and N. Smith, *Am. Rev. Tuberc.*, 1952, **66**, 125-133.
41. E. Suter, *Am. Rev. Tuberc.*, 1952, **65**, 775-776.
42. T. Scior, I. M. Morales, S. J. G. Eisele, D. Domeyer and S. Laufer, *Arch. Pharm. Pharm. Med. Chem.*, 2002, **11**, 511-525.
43. R. Lai, M. Khanna, H. Kaur, N. Srivastava, K. K. Tripathi and S. Lai, *Crit. Rev. Microbiol.*, 1995, **21**, 19-30.
44. J. Suarez, K. Ranguelova, A. A. Jarzecki, J. Manzerova, V. Krymov and Z. B. Zhao, *J. Biol. Chem.*, 2009, **284**, 7017-29.
45. P. Sensi, P. Margalith and M. T. Timbal, *Farmaco Sci.*, 1959, **14**, 146-147.
46. A. Zumla, N. Payam and T. S. Cole, *Nat. Rev. Drug Discov.*, 2013, **12**, 388-404.

47. Hong Kong Chest Service, Medical Research Council, *Lancet*, 1981, **I**, 171–4.
48. Y. Zhang and D. Mitchison, *Int. J. Tuberc. Lung Dis.*, 2003, **7**, 6-21.
49. WHO Model List of Essential Medicines. 18th edition. April 2013.
50. Y. Zhang, M. M. Wade, A. Scorpio, H. Zhang and Z. Sun, *J. Antimicrob. Chemother.*, 2003, **52**, 790-795.
51. A. S. Kolyva and P. C. Karakousis, Chapter from the book understanding tuberculosis- new approaches to fighting against drug resistance. Downloaded from <http://www.intechopen.com/books/understanding-tuberculosis-new-approaches-to-fighting-against-drug-resistance>. (accessed April 2016).
52. L. Ralph, A. Basil and S. Alexander, *Pharmaceutical Innovation: Revolutionising Human Health*. Chemical Heritage Foundation, 1999.
53. K. Mikusová, R. A. Slayden, G. S. Besra and P. J. Brennan, *Antimicrob. Agents Chemother.*, 1995, **39**, 2484-2489.
54. Y. Zhang, *Ammu. Rev. Pharmacol. Toxicol.*, 2005, **45**, 529-564.
55. D. A. Mitchison, *Int. J. Tuberc. Lung Dis.*, 2000, **4**, 796-806.
56. M. M. Wade and Y. Zhang, 2004, *Front. Biosci.*, **9**, 975-994.
57. F. G. Winder. The mode of action of the antimycobacterial agents and associated aspects of the molecular biology of the Mycobacteria, *Academic Press Inc*, New York 1982.
58. Aminosalicylate sodium. In *Drug Facts and Comparisons*, 4th ed., St. Louis 2000. p.750.
59. J. Volmink and P. Garner. Directly observed therapy for treating tuberculosis. *Cochrane Database Syst. Rev.*, 2015, **5**, 1-56.
60. E. D. Chan and M. D. Iseman, *BMJ*, 2002, **325**, 1282–1286.

61. World Health Organization. Multidrug and extensively drug-resistant TB (M/XDR-TB): 2010 global report on surveillance and response. WHO/HTM/TB/2010.3. Geneva, WHO, 2010.
62. American Thoracic Society CDC infectious disease society of America 'Treatment of Tuberculosis' MMWR. Morbidity and Mortality Weekly Report, 2003, **52**, 1-77.
63. C. E. Barry, *Biochem. Pharmacol.*, 1997, **54**, 1165-1172.
64. K. Duncan, *Expert, Opin. Ther.*, 1998, **8**, 137-142.
65. D. Goletti, D. Weissman, R. W. Jackson, N. M. Graham, D. Vlahov, R. S. Klein, S. S. Munsiff, L. Ortona, R. Cauda and A. S. Fauci, *J. Immunol.*, 1996, **157**, 1271-1278.
66. F. Mariani, D. Goletti, A. Ciramella, A. Martino, V. Colizzi and M. Fraziano, *Curr. Mol. Med.*, 2001, **1**, 209-216.
67. S. A. Munro, S. A. Lewin, H. J. Smith, M. E. Engel, A. Fretheim and J. Volmink, *PLoS Med.*, 2007, **4**, e238.
68. G. Canetti, *The Tubercle Bacillus in the Pulmonary Lesion of Man*. Springer Publishing Company, New York, 1955.
69. V. Briken, S. A. Porcelli, G. S. Besra and L. Kremer, *Mol. Microbiol.*, 2004, **53**, 391-403.
70. J. Szczepan, S. Andrzej and K. Katarzyna, *BioEssays*, 2008, **30**, 943-954.
71. P. M. Sabale, J. Patel and Y. Patel, *Int. J. Pharm. Biol. Sci.*, 2012, **3**, 251-265.

Chapter 2

Literature Review

2.0 Transition metal complexes as potential therapeutic agents:

Transition metals have a crucial place within medicinal biochemistry. Research has revealed outstanding progress in the application of transition metal complexes as drugs to treat several human diseases like carcinomas, lymphomas, diabetes and neurological disorders. Transition metals exhibit variable oxidation states and can interact with several negatively charged molecules. This activity of transition metals started the progress of metal-based drugs with promising pharmacological application and may offer exceptional opportunities. Coordination of metal cations with organic drugs is a promising approach that has been successful in many cases with different pharmacological activities.¹⁻⁶ Specifically, several metallic complexes of anti-tubercular drugs have been reported, but accounts of studies of the solution state as well as the solid state of such complexes, to improve the permeability and bioavailability of the parent drug, are lacking.

2.1 Metal ion complexes of anti-TB agents

Complexation between anti-tubercular drugs and metal ions and the methods for complex synthesis have been reported by different authors. Allan *et al.*⁷ reported some first-row transition metal complexes of ISO. Complexes of the chlorides and bromides of manganese(II), cobalt(II) and nickel(II), copper(II) and zinc(II) with ISO have been prepared and studied using magnetic susceptibilities, infrared and electronic spectra.

Cole and co-workers⁸ have investigated copper (II) and zinc (II) interaction with ISO. The formation constants for copper (II) and zinc (II) complexes of ISO and guanosine-5-monophosphate have been measured potentiometrically at 37 °C, I =150 mmol dm⁻³ [NaCl]. These constants have been used in computer models to assess the extent of complex formation by the drug *in vivo*.

Sousa *et al.*⁹ have described ISO metal complex reactivity and insight for the development of a novel anti-tuberculosis drug design. Reactivity studies were conducted with hydrogen peroxide, hexacyanoferrate(III), and aqua penta cyanoferrate(III). The latter species showed a preference for the inner-sphere electron transfer reaction pathway. Additionally, the electron transfer reaction performed with either free ISO or (ISO) penta cyanoferrate(II) complex resulted in similar oxidised ISO derivatives as seen when KatG enzyme was used. However, upon metal coordination, a significant enhancement in the formation of isonicotinic acid was observed as compared with that of isonicotinamide.

Buss *et al.*¹⁰ reported the oxidation of antibiotic RFN catalysed by a metal ion. The metal ions Cu(II), Mn(II) and Co(II), catalysed the oxidation of RFN from naphthol hydroquinone to the naphthoquinone form. Several transition complexes possess anti-tubercular properties and because these complexes often pose stronger activity than the parent compound, it was hypothesised that the active form of most anti-tubercular drugs is in fact the metal complex itself.

Thakar *et al.*¹¹ studied the interaction of transition metal ions and rare earth metal ions with drug ISO in 20% (v/v) ethanol-water mixture at 0.1 (NaClO₄) ionic strength and a temperature of 298 K by potentiometric titration. The data obtained were used to calculate the values of proton-ligand stability constant (p*K*) and metal-ligand stability constant (log *K*). The transition metal ions and rare earth metal ions form 1:1 and 1:2 metal-ligand complexes.

Magare and co-workers¹² reported the interaction of some anti-tubercular drugs with transition metal ions. The stability constants of Mn(II), Co(II), Ni(II), Cu(II), and Zn(II) complexes with PZA, ISO and EMB-HCl were evaluated. The study was carried out at 30 °C and fixed 0.1 M (NaClO₄) ionic strength in an aqueous medium potentiometrically. The proton-ligand stability constants and metal-ligand stability constants were determined and discussed with respect to

the order of stability and the basicity of ligands, and correlated with atomic number, ionisation potential, electronegativity and reciprocal of ionic radii.

Shailendrasingh *et al.*¹³ examined the stability constants for complexation of ISO and imipramine hydrochloride with transition metal ions Fe, Co, Ni, Zn and Cd by potentiometric titration in 20% (v/v) ethanol-water mixture at three different temperatures (25 °C, 35 °C and 45 °C) and an ionic strength of 0.1 M NaClO₄. The method of Calvin and Bjerrum as adopted by Irving and Rossetti has been employed to determine metal-ligand stability constant log *K* values. The transition metal ion forms 1:1 and 1:2 complexes. The thermodynamic parameters such as Gibbs free energy change (ΔG), entropy change (ΔS) and enthalpy change (ΔH) associated with the free complexation reactions were calculated. The formation of metal complexes was found to be spontaneous, exothermic in nature and favourable at a lower temperature.

Nageswara *et al.*¹⁴ studied the protonation and complexation equilibria of EMB-HCl potentiometrically in an aqueous medium at an ionic strength of 0.1 mol dm⁻³ and 303 K. The protonation constants, as well as binary stability constants of Cu(II), Ni(II) and Co(II) complexes, were evaluated, and the best fit was chosen based on the statistical parameters using the MINIQUAD75 computer program.

Shehata *et al.*¹⁵ investigated the thermodynamics of metal complexation of the macrocyclic antibiotic RFN. The stoichiometric equilibrium constants were determined in 50% (v/v) methanol-water medium at different temperatures and constant ionic strength (0.05 M KCl) by means of potentiometry.

Yamabe *et al.*¹⁶ have shown that metal complexation of drugs changes their bioavailability and toxicity. Oliveira *et al.*¹⁷ studied the Co(III) complexes of thiosemicarbazones as potential anti-*M. tuberculosis* agents. Co(II) complexes from 2-acetyl pyridine N (4)-R-

thiosemicarbazone (Hatec-R, R=alkyl, aryl) have been characterised by elemental analysis, FTIR, UV-Visible and ^1H NMR spectroscopies, cyclic voltammetry, conductimetry measurement and single crystal X-ray diffraction. The Co(III) complex showed satisfactory activity with minimal inhibitory concentration value under $10\ \mu\text{mol dm}^{-3}$ and presented quite low toxicity.

Sonar and Pawar¹⁸ investigated the spectroscopic and pH-metric studies of Ce(III), Dy(III), Gd(III), Yb(III), and Pr(III) metal complexes of RFN. The metal-ligand and proton-ligand stability constants were determined at various ionic strengths. The calculated values of the stability constants are high, indicating stable complexes over a wide range of ionic strength.

Sonar and Pawar¹⁹ determined the stability constants of rifampicin complexes with rare earth metal ions in the temperature range 303-318 K at constant ionic strength 0.1 M in 50% dioxane-water mixture using the pH-metric technique. The thermodynamic parameters (ΔG , ΔH and ΔS) were calculated. The formations of the metal complexes were found to be spontaneous and exothermic in nature.

Bilgic Alkaya *et al.*²⁰ studied the ternary complex formation of ISO with some transition metals and amino acids using spectroscopy and potentiometric techniques. Their stability constants were determined and the results showed that forming ternary complexes of ISO –metal with amino acids can increase anti-tumor activity. The presence of Zn(II) and Cu(II) balances and prevents hepatic toxicity as well as side effects. Copper and zinc bonding geometry are square-planar with ISO carbonyl oxygen and hydrazide amino nitrogen atom donors. Complexing with Cu(II) and Zn(II) does not significantly alter ISO molecular conformation.

Patel *et al.*²¹ synthesised Cu(II), Ni(II) and Co(II) complexes of ciprofloxacin and evaluated their antimicrobial, antioxidant and anti-tubercular activity. It was observed that the anti-TB activity of the ligand was enhanced on complexation with Ni(II) and Co(II) ions.

Tiwani²² reported the antibacterial activity of mixed ligand chelate and its application to tuberculosis. The study revealed that metal chelates (complexes) are more potent compared to the parent drug.

Sandbhor *et al.*²³ worked on metal complexes of carboxamidrazone analogues as anti-tubercular agents; the analogues were synthesised, and the structures of their metal complexes were determined using X-ray crystallography. All complexes were assessed for their *in vitro* activity upon copper complexation, resulting in enhancement factors of 32-64 in their anti-tubercular activity.

Phase *et al.*²⁴ determined the stability constant of the ternary chelate of Zn(II) metal ion with aspartame and EMB-HCl as first ligand and amino acid as a secondary ligand. The reaction was carried out in 20% (v/v) ethanol-water medium pH-metrically at 30 °C and 0.1 M NaClO₄ ionic strength. The formation of complex species as a function of pH was also discussed using the method of Irving and Rossotti and evaluated using the computer SCOGS program.

Anti-tubercular drugs can coordinate with metal cations through different chemical groups: in the case of ISO, these are the heterocyclic nitrogen from the pyridine ring, the carboxylic O atom and N atoms of the hydrazide group. For this versatility, ISO is also an interesting ligand from the chemical point of view. The d-block elements form small, highly-charged, ions with vacant, low energy orbitals which are able to accept lone pairs of electrons donated by ligands and this favours metal complex formation.²⁵ The drugs ISO, EMB, PZA and PAS are all able to act as ligands and form metal complexes. Hence, these are good targets for investigation. The stability of metal complexes of therapeutic drugs plays a major role in biological processes in the context of metalloproteins, metalloenzymes, storage, transport, detoxification and chemical activity.^{26,27}

References:

1. L. R. Azuara and M. E. Bravo-Gomez, *Curr. Med. Chem.*, 2010, **17**, 3606-3615.
2. World Health Organization, TB. Global Emergency, WHO Report No.14977, Geneva, Switzerland, 1994, 97-98.
3. B. Bottari, R. Maccari, F. Monforte, R. Ottana, E. Rotondo and M. G. Vigorita, *Bioorg. Med. Chem. Lett.*, 2000, **10**, 657-660.
4. G. Lowe, A. S. Droz, T. Vilaivan, G. W. Weaver, J. J. Park, J. M. Pratt, L. Tweedale and L. R. Kelland, *J. Med. Chem.*, 1999, **42**, 3167-3174.
5. R. A. Sanchez-Delgado, M. Navarro, H. Perez and J. A. Urbina, *J. Med. Chem.*, 1996, **39**, 1095-1099.
6. R. Malhotra, J. P. Singh, M. Dudeja and K. Sdhindsa, *J. Inorg. Biochem.*, 1992, **46**, 119-127.
7. J. R. Allan, G. M. Baillie and N. D. Baird, *J. Coord. Chem.*, 1984, **13**, 83-88.
8. A. Cole, P. P. May and D. R. Williams, *Agent Actions*, 1993, **13**, 91-97.
9. E. H. Sousa, L. A. Basso, D. S. Santo, I. C. Diogenes, E. Longinotti, L. G. Lopes and I. S. Moreira, *J. BioInorg. Chem.*, 2012, **17**, 275-83.
10. W. C. Buss, E. Reyes and T. D. Barela, *Res. Commun. Chem. Pathol. Pharmacol.*, 1977, **17**, 547-50
11. S. V. Thakar, M. Farooqui and S. D. Naikwade, *Int. J. Inorg. Chem.*, 2012, **4**, 5-7.
12. B. K. Magare, M. N. Farooqui, R. S. Shelke, and M. B. Ubale, *Orient. J. Chem.*, 2009, **25**, 387-390.
13. V. T. Shailendraingh, F. Mazahar and D. N. Sahebra, *J. Chem., Biol. Phys. Sci.*, 2013, **4**, 1-7.
14. G. R. Nageswara and M. M. Annapurna, *J. Pharm. Educ. Res.*, 2010, **1**, 44-50.

15. I. Shehata, I. Kenawy, A. H. Askalany and A. A. Hassan, *Can. J. Chem.*, 2001, **79**, 42-49.
16. S. Yamabe and K. T. Tokyo, *Chem. Abs.*, 1989, **111**, 219307z.
17. C. G. Oliveira, P. I. Maia, M. Miyata, F. R. Pavan, C. Q. F. Leite, E. T. Almeida and V. M. Teflon, *J. Braz. Chem. Soc.*, 2014, **25**, 1848-1856.
18. A. N. Sonar and N. S. Pawar, *E-J Chem.*, 2011, **8**, 517-522.
19. A. N. Sonar and N. S. Pawar, *J. Chem. Pharm. Res.*, 2010, **2**, 446-449.
20. D. B. Alkaya, S. Karaderi and G. Erdogan, *Trakya Univ. J. Nat. Sci.*, 2013, **14**, 1-14.
21. K. S. Patel, J. C. Patel, H. R. Dholariya, V. K. Patel and K. D. Patel, *Open J. Met.*, 2012, **2**, 49-59.
22. C. R. Tiwari, *Pharma. Chem.*, 2012, **4**, 39-42.
23. U. Sandbhor, S. Padhye, D. Billington, D. Rathbone, S. Franzblau, C. E. Anson and A. K. Powell, *J. Inorg. Biochem.*, 2002, **90**, 127-136.
24. R. P. Phase, A. G. Shankarwar, S. G. Shankarwar and T. K. Chondhekar, *Adv. App. Sci Res.*, 2013, **4**, 46-49.
25. J. Chen, K. Fukuzumi, B. Lp, Florence and A. P. Cid, *Int. J. Pharma. Biol. Chem. Sci.*, 2014, **3**, 36-45.
26. L. Oehninger, R. Rubbiani and I. Ott, *Dalton Trans.*, 2013, **42**, 3269-84.
27. S. Thakar, S. Naikwade and M. Farooqui, *Int. J. Chem. Sci.*, 2013, **1**, 88-92.

Chapter 3

Glass Electrode Potentiometry

3.1 Glass Electrode Potentiometry

Glass electrode potentiometry (GEP) is a volumetric method in which the potential difference between two electrodes (reference and indicator electrode) is measured as a function of the added reagent. It is the most versatile and frequently used analytical technique for studying chemical interaction in aqueous solution.¹ The difference in potential (emf) is used to measure the concentration of the analyte.

The main advantage of this technique, compared to other methods, is the possibility of monitoring the resulting complexation as a function of pH and to observe the exact point at which complexation takes place. Also, the dissociation constants and the stability constants of complexes can be calculated.² This method requires the use of a glass hydronium ion selective electrode (indicator electrode), an appropriate reference electrode and a sensitive potentiometer.^{3,4}

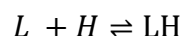
There are factors which assist the formation of a complex. The capacity of a metal ion to form a complex with a ligand is decided by its environment which in turn decides the stability of the compound. Some of the factors which affect the stability of the complexes are solvents, temperature, nature of metal ion and nature of ligands.

In this study, glass electrode potentiometry was used to investigate the interaction between the ligand, the protons and the metal ions. Potentiometric data were analysed using the Equilibrium Simulations for Titration Analysis (ESTA) suites of the program. These data were also used to envisage the possible metal/ligand models and to predict the distribution of species in solution.

3.2 Theory

The theory of formation constant and methods of determination has been covered extensively in the literature.⁵⁻⁷

For the reaction



where L is the ligand, H is a proton and LH is a protonated ligand, the thermodynamic protonation constant, ${}^T K_{LH}$, of the ligand can be expressed as

$${}^T K_{LH} = \frac{\{LH\}}{\{L\}\{H\}} \quad (3.1)$$

where $\{LH\}$ is the activity of the singly protonated ligand, $\{L\}$ is the activity of the ligand and $\{H\}$ is the activity of the proton.

Likewise,

$$\{X\} = \gamma_X [X] \quad (3.2)$$

where $\{X\}$ is the activity of species X (which can be a ligand, a proton or a metal ion), γ_X is the activity coefficient of the species X and $[X]$ is the molar concentration of X.

Therefore,

$${}^T K_{LH} = \frac{(\gamma_{LH}[LH])}{(\gamma_L[L])(\gamma_H[H])} \quad (3.3)$$

Equation (3.3) can be rearranged as

$${}^T K_{LH} = \left(\frac{\gamma_{LH}}{\gamma_L \gamma_H} \right) \left(\frac{[LH]}{([L][H])} \right) \quad (3.4)$$

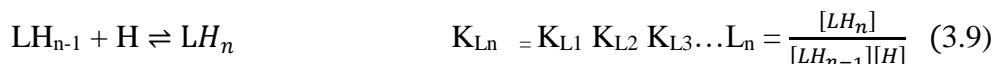
At constant ionic strength $\left(\frac{\gamma_{LH}}{\gamma_L\gamma_H}\right)$ is constant and the equilibrium constant can be expressed as

$$K_{L1} = \frac{[LH]}{[L][H]} \quad (3.5)$$

For a ligand that has three protonation constants, ${}^T K_{L1}$, ${}^T K_{L2}$ and ${}^T K_{L3}$, these can be described in a stepwise manner as



Also, for the ligand with n protonation constants



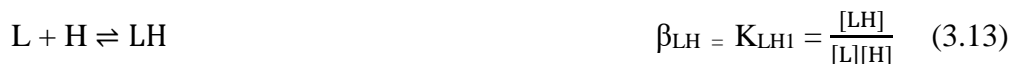
Similarly, for the metal M and the ligand L that react to give a complex ML, the stability constant (K_{ML}) can be described as



Therefore, for the general case,



The overall formation constant, β can be expressed as





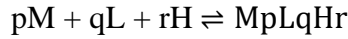
Similarly,



and



For the reaction



p , q and r represent the stoichiometric coefficients of M , L and H respectively, r the stoichiometric coefficient of H or hydroxyl ion added to the complex. The formation constant (β) of the reaction can be expressed as

$$\beta_{pqr} = \frac{[\text{M}_p\text{L}_q\text{H}_r]}{[\text{M}]^p [\text{L}]^q [\text{H}]^r} \quad (3.20)$$

The concentration of $\text{M}_p\text{L}_q\text{H}_r$ at point k is expressed as

$$[\text{M}_p\text{L}_q\text{H}_r]_k = \beta_{pqr} [\text{M}]_k^p [\text{L}]_k^q [\text{H}]_k^r \quad (3.21)$$

The total concentration of the metal ion at point k ($T_{\text{M}, k}$) can be expressed as

$$T_{\text{M}, k} = [\text{M}]_k + \sum_{i=1}^N P_i \beta_{pqr} [\text{M}]_k^p [\text{L}]_k^q [\text{H}]_k^r \quad (3.22)$$

The total concentration of the ligand at point k ($T_{L, k}$) can be expressed as

$$T_{K,L} = [L]_K + \sum_{i=1}^N P \beta_{pqr} [M]_p^k [L]_q^k [H]_r^k \quad (3.23)$$

The total concentration of the hydronium ion at point k ($T_{H, k}$) can be expressed as

$$T_{K,H} = [H]_K + \sum_{i=1}^N P \beta_{pqr} [M]_p^k [L]_q^k [H]_r^k \quad (3.24)$$

The coefficient of the proton (r) can be greater than or equal to 1 if the complex is protonated. However, if the ligand loses all its protons upon complexation with the ligand, or if the hydroxide ion (OH^-) is added to the complex, then r can have a negative value.^{8,9} When the complex is not protonated, and there is no hydroxide ion attached to the complex then $r = 0$. ML , MLH , MLH_2 and MLH_n indicate a complex with one central metal ion that is not protonated, singly protonated, doubly protonated, and having one ligand and n protons attached respectively.

3.3 Data Analysis

The stability constants of the protonation/deprotonation of the ligands and complexes were calculated from the potentiometric data using the ESTA suite of programs. This package has two basic program modules, namely the simulation unit (ESTA1) and the optimisation units (ESTA2B). The simulation unit characterises the system on a point-by-point basis, and the optimisation unit is used to characterise the titration as giving the average values for the titration system. Simulation is done by using the mass balance equations, which help to calculate complexation function and speciation of the solution, thereby aiding the interpretation

of the data. ESTA5 is a plotting unit, used to place the results calculated by ESTA1 in a graphical form.

Three tasks from the ESTA program were used in this study, namely the formation function (Z-bar), the deprotonation function (Q-bar) and the objective function (OBJE).

The ZBAR task is used to calculate the formation functions at each titration point; the calculated and observed functions were obtained from the ZBAR, and the residuals have been computed from equations 3.29 and 3.30 for the proton formation functions and the metal formation functions respectively.

$$\text{Residual pH} = \text{pH}^o - \text{pH}^c \quad (3.25)$$

Similarly

$$Z - \text{bar}_H = \frac{T_H - H + OH}{T_L} \quad (3.26)$$

and

$$Z - \text{bar}_M = \frac{A + (n \sum \beta_{LHn} H^n)}{T_M} \quad (3.27)$$

where
$$A = \frac{T_H H + OH}{(n \sum \beta_{LHn} H^n)} \quad (3.28)$$

For proton formation function,

$$\text{Residual formation function} = Z\text{-bar}^o_H - Z\text{-bar}^c_H \quad (3.29)$$

For metal formation function,

$$\text{Residual} = Z\text{-bar}^o_M - Z\text{-bar}^c_M \quad (3.30)$$

where

$$Z_{H\text{-bar}} \text{ point residual} = [(pH^O - pH^C)^2 + (Z\text{-bar}^O_H - Z\text{-bar}^C_H)^2]^{1/2} \quad (3.31)$$

and

$$Z_{M\text{-bar}} = [(pA^O - pA^C)^2 + (Z\text{-bar}^O_M - Z\text{-bar}^C_M)^2]^{1/2} \quad (3.32)$$

where pH^O is the observed pH, pH^C is the calculated pH, $Z\text{-bar}^O_H$ is the observed proton formation constant, $Z\text{-bar}^C_H$ the calculated proton formation function, $Z\text{-bar}^O_M$ is the observed metal formation function, $Z\text{-bar}^C_M$ is the calculated metal formation, pA^O is the negative logarithm of the observed ligand concentration, pA^C is the calculated ligand concentration, E_H is the potential of the hydronium ion, and ${}^1E^O_H$ is the standard potential. S_H is the slope of the electrode, and $\log H$ is the logarithm of the proton concentration. T_H is the total concentration of the hydronium ion, H is the concentration of the hydronium ion, OH is the concentration of the hydroxide ion, T_L is the total ligand concentration, A is the ligand concentration, n is the number of protons bound to the ligand, β_{LH_n} is the formation constant of the protonated ligand with n protons, and T_M is the total concentration of the metal ion.¹⁰⁻¹²

The ESTA task $Q\text{-bar}$ is used to calculate the observed and calculated deprotonation functions. The deprotonation function is defined as the average number of protons released by the ligand upon complexation with the metal ion; $Q\text{-bar}$ is expressed as

$$Q_{M\text{-bar}} = \frac{(T^*_H - T_H)}{T_M} \quad (3.33)$$

where T^*_H is the calculated total concentration of protons in the system at the observed pH ignoring the presence of all the metal complexes.

When $p = \text{zero}$ and $OH = \frac{K_w}{H}$

the mass balance equations for T^*_H and T_L can be written as

$$T^*_H = H - OH + \sum_{J=1}^{NJ} r[M_p L_q H_r] \quad (3.34)$$

And

$$T_L = L + OH + \sum_{J=1}^{NJ} q[M_p L_q H_r] \quad (3.35)$$

where N_J is the total number of titration points.

For a binary system, a formation function is defined for the ligand subsystem as

$$\bar{n} = \frac{T^*_H - H + OH}{T^r_L} \quad (3.36)$$

In general, \bar{Z}_H was used to estimate protonation constants of the ligand and the stability constants of the complexes. From \bar{Z}_H , the number of protons bound per ligand was estimated, and from \bar{Z}_M the number of protons released by the ligand upon complexation with the metal ion was estimated. \bar{Q} indicates the number of protons released by the ligand on complexation with the metal ion. \bar{Q} was compared to \bar{n} which measures the number of protons that could have bound to the ligand in the absence of the metal ion. The distribution template of the ESTA programs was used to calculate the distribution of the ligand in the metal complexes in solution.

The formation (\bar{Z}_M) and the deprotonation (\bar{Q}_M) functions were used to investigate the reproducibility of the experimental data and the reliability of evaluated $\log \beta_{pqr}$ values.^{13,14} These two functions serve two purposes. Firstly, they give a visual check on the experimental data and secondly, their shape provides an idea of the speciation model applicable to the system.

If the \bar{Z}_M curves at the different metal to ligand ratios are superimposable, then simple stepwise complexation is indicated. Non-superposability indicates that polynuclear species are

present. Fanning back of Z_M -bar curves shows the presence of hydroxo or mixed hydroxo species.¹⁵ When Q -bar coincides with n -bar, it indicates that no further complexation takes place in this range. When Q -bar rises above the n -bar curve, it indicates hydrolysis of the metal ion forming species MLH_{-1} .

The task (OBJE) was used for weighting the objective function (U_{obj}) contribution based on the observed emf and the relative contributions of the most significant errors to the weight at each titration point. This function is expressed as;

$$U_{obj} = (N - n_p)^{-1} \sum_{n=1}^N n_e^{-1} \sum_{q=1}^{ne} w_{nq} (y_{nq}^{obs} - y_{nq}^{calc})^2 \quad (3.37)$$

where

N is the total number of experimental points, n_p is the total number of points being optimised, n_e is the total number of electrodes, w_{nq} is the weight of the q^{th} residual at the n^{th} point and y_n^{th} the calculated variable at the q^{th} residual at the n^{th} point.

Data are optimised by minimising the objective function. This can be achieved if the objective function is quadratic with all the parameters (Gauss-Newton method)

U_{obj} can, therefore, be expressed as

$$U_{obj} = a + ptb + \frac{(p^t H_p)}{2} \quad (3.38)$$

The program also calculates the standard deviations, estimated errors for the parameters being optimised using the method of least-squares. The standard deviation σ can be expressed as

$$\sigma = \left[\frac{U_{obj} G_{rr}}{(N - n_p)} \right]^{1/2} \quad (3.39)$$

The Hamilton R-factor (R^H) can be used to test the agreement between the observed and the calculated values of the refined data. This factor can be expressed as

$$R_f^H = \left[\frac{U_{obj}}{\sum n_e^{-1} \sum W_{nq} (Y_{nq}^{obs})^2} \right]^{1/2} \quad (3.40)$$

The best possible R_f^H value based on the number of variables and the random errors in the analytical data, R_{lim}^H can be expressed as

$$R_{lim}^H = \left[\frac{N_{obj}}{\sum n_e^{-1} \sum W_{nq} (Y_{nq}^{obs})^2} \right]^{1/2} \quad (3.41)$$

If R_f^H is less than R_{lim}^H the model is within the maximum allowed experimental error.²⁰

3.3.1 The Electrode Cell

The electrode cell is the essential tool of potentiometric analysis. An electrochemical cell consists of two half-cells, each containing an electrode in contact with an electrolyte. The electrode is an electronic conductor, and an electrolyte is a phase in which ions carry charges. The half-cells are connected by a salt bridge which allows ions to move between half-cells but prevents mixing of the electrolytes.

The setup of the cell can be represented as below:

reference electrode | salt bridge | analyte solution | glass electrode

E_{ref}

E_j

E_g

Each electrode possesses a half-cell reaction. The reference electrode potential, E_{ref} , has a known constant value and it is not affected by the concentration of the analyte solution,¹⁶ whereas the potential of the glass electrode, E_g , varies with the concentration of the analyte solution.¹⁷ The liquid junction potential, E_j , results from a difference in the concentrations of

the analyte solution and the internal reference solution. The observed potential, E_{cell} , can therefore be expressed as

$$E_{cell} = E_{ref} + E_j + E_g \quad (3.42)$$

As E_g varies with the concentration of the analyte solution, the Nernst equation can be written as

$$E_{cell} = E_{ref} + E_j + \left(E_g + \frac{RT \ln \{H\}}{F} \right) \quad (3.43)$$

where E_g is the standard electrode potential and $\{H\}$ is the activity of the hydrogen ion.

If the ionic strength and hence the activity coefficient of the H ions are constant, then

Equation 3.43 can be written as;

$$E_{cell} = E_{const} + \frac{RT \ln [H^+]}{F} \quad (3.44)$$

The potential depends on the temperature, and the relationship between the two varies with the activity of the hydrogen ion. This can be expressed in terms of the slope factor, s

$$s = \frac{2.303RT}{F} \quad (3.45)$$

Substituting Equation 3.45 into 3.44 yields

$$E_{cell} = E_{const} + s \log [H^+] \quad (3.46)$$

Both slope, s , and E_{const} are determined to calibrate the electrode.

3.4 Experimental

3.4.1 Preparation of Solutions

The potentiometric titrations were performed at a stable temperature and ionic strength^{18,19} under an inert atmosphere. The end-point of the potentiometric data and the carbonate

contamination of the sodium hydroxide titrant solution were checked by acid-base titration using the Gran method.²⁰ The electrode system was calibrated according to the method of Irving et al.²¹ All the solutions used for titration were standardised; the primary chemical of known mass was used to standardise the acids/bases which were used to standardise the ligand solutions. Methods for standardisation of solutions of the metal ions are described.²²⁻²⁴

The chemicals and reagents were of analytical grade and were used without any additional purification. Solutions of sodium hydroxide (0.1 M) were prepared from Merck ampoules (1.09959-Trisol) in distilled deionised water and were prepared under an inert atmosphere of nitrogen gas to eliminate any contamination by CO₂. These solutions were standardised against potassium hydrogen phthalate (KHP). The solutions of hydrochloric acid (HCl) (0.01 M) were prepared from Merck ampoules (1.09970) and standardised with the standard solution of sodium hydroxide using Gran methods. All stock solutions were prepared using NaCl as a background electrolyte to maintain a constant ionic strength of 0.15 mol dm⁻³.

The ligands were purchased from Sigma-Aldrich (South Africa). They were in powder form and were 99.0% pure. 0.01 M Ligand solution was prepared in 0.01 M HCl. The metal solutions were prepared by dissolving NiCl₂·6H₂O, CuCl₂·2H₂O and ZnCl₂ in boiled out glass distilled water to yield 0.01 M solutions. The toxic level of the metals was considered by using a low concentration of metal.

The choice of the metal ions rests on their availability and on their importance in a physiological system. They were standardised by using a meter ohm 765 Dosimat automatic burette dispensing 0.01 mol dm⁻³ EDTA solution. Titration was done in duplicate to check the reproducibility.

3.4.2 Potentiometric Measurement

All pH measurements were carried out at 25 °C and a stable ionic strength of 0.15 mol dm⁻³ (NaCl). The Ω Metrohm glass electrode was calibrated with a set of Ω Metrohm ion analysis pH buffers, and the Nernstian slope was determined.^{25,26} The slope varied from 57.13 to 58.27 and the pH range from 2.00-11.00 using a Ω Metrohm 848 Titrino plus. The data of acid/base titrations were used to calculate the electrode response intercept, E^0 , from the slope and the negative logarithm of the water ion product, pK_w .

For the protonation of the ligand, an exact volume was taken from the prepared ligand solution. The solution was stirred continuously and gently with a Ω Metrohm 801 magnetic stirrer. When a stable temperature of 25 ± 0.1 °C was attained, the solutions of the ligands were titrated with standard solutions of sodium hydroxide. For the complexation titration, the metal to ligand molar ratios varied between 1:1 and 1:2. These solutions were titrated with standard solutions of NaOH.

3.5 Results

3.5.1 Isoniazid (ISO)

3.5.1.1 Protonation

$Z_{H\text{-bar}}$ for protonation of ISO is presented in Figure 3.1. The function levels to zero at a high pH of 11.82; thereafter, it rises and then levels off at the $Z_{H\text{-bar}}$ value of 1 between pH 9.38 and 5.57. Below pH 4.78 the function rises to a $Z_{H\text{-bar}}$ of 1.8. This indicates that two protons have been added to the ligand making it di-protonated at low pH.

Protonation constants of ISO were estimated from the half $Z_{H\text{-bar}}$ values, $\log K_{LH1}$ of 10.95, $\log K_{LH2}$ of 3.67, and these values were used as the starting values in ESTA.

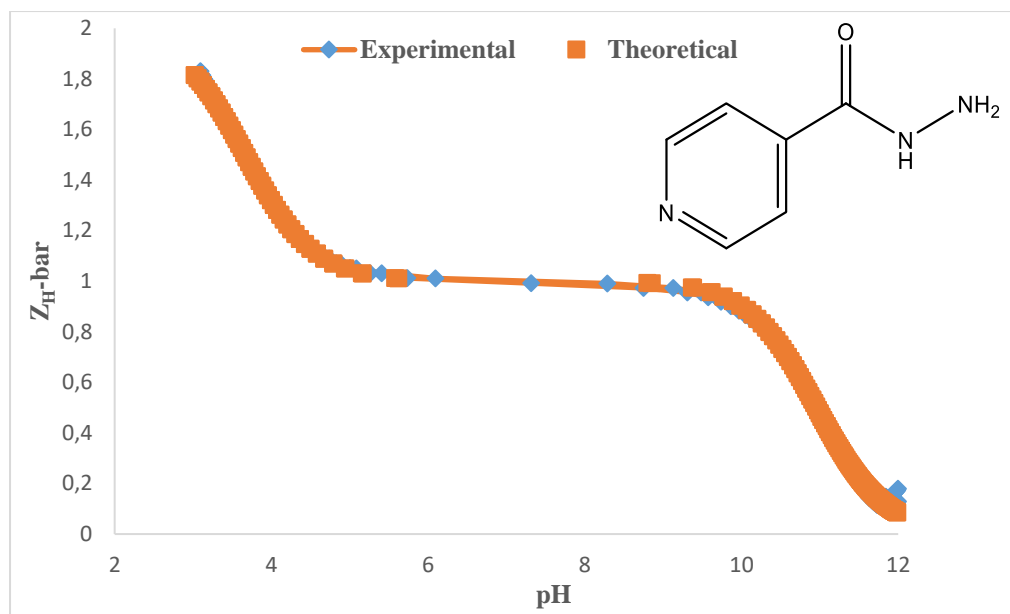


Figure 3.1: $Z_{H\text{-bar}}$ as a function of pH for the protonation of ISO.

Optimised $\log \beta_{pqr}$ are given in Table 3.1. The results are in good agreement with literature values of $\log K_{LH1}$ of 10.6 and $\log K_{LH2}$ of 3.8 for ISO at 25 °C and $I = 0.10 \text{ mol dm}^{-3}$.²⁷ The theoretical and experimental plots are shown in Figure 3.1. They are well superimposed, and this gives confidence to the result.

Table 3.1 : Stability constants ($\log \beta_{pqr}$) for ISO $\beta_{pqr} = [M_p L_q H_r] / [M]^p [L]^q [H]^r$, $I = 0.15 \text{ mol dm}^{-3}$ (NaCl), $T = 25 \text{ }^\circ\text{C}$. S. dev. denotes standard deviation in $\log \beta_{pqr}$; R_f^H is the Hamilton R-factor and R_{lim}^H its limit, n_T is the number of titrations, (n_p) is the number of titration points.

Ligand	P	q	R	$\log \beta_{pqr}$	S. dev.	R_f^H	R_{lim}^H	$n_T(n_p)$
ISO-H	0	1	1	10.95	0.003			
ISO-H ₂	0	1	2	14.62	0.003	0.003	0.001	2(323)

The three species of this ligand are shown in the speciation graph in Figure 3.2. The predominant species in solution from pH 3.77-9.36 is LH.

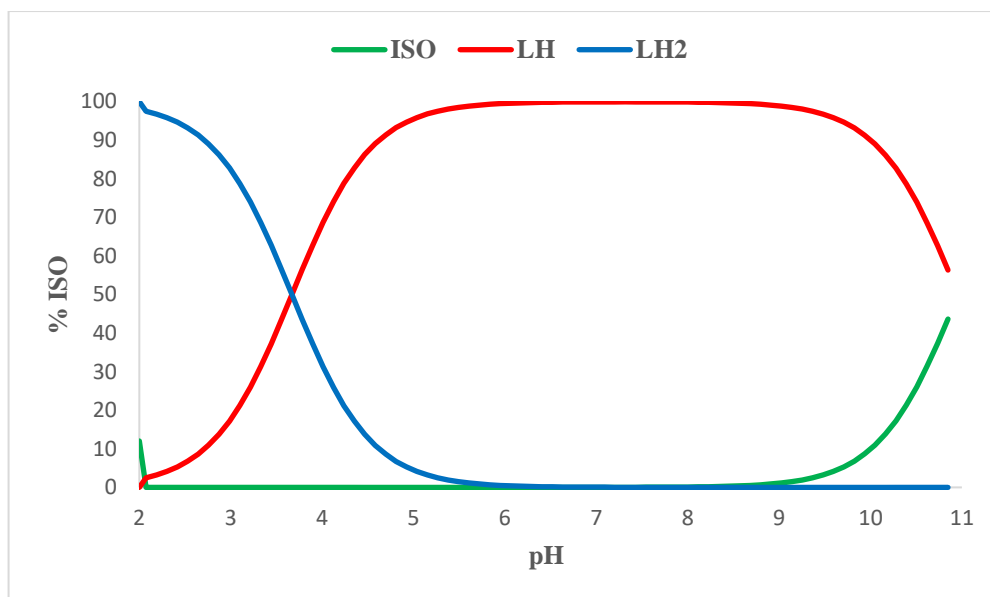


Figure 3.2: Distribution curve for the protonation of ISO.

The protonation of ISO is through both the pyridyl nitrogen and the hydrazide group. The measured dissociation constants for ISO of 3.67 and 10.95 correspond to the protonation of the pyridine nitrogen and the hydrazide group respectively. The values obtained are close to the literature values of 10.6 and 3.8,²⁷ and 10.8 and 3.5.²⁹

3.5.1.2 Copper complexation

Figure 3.3 shows the complex formation (Z_M -bar) for the Cu(II) ISO titrations. The Z_M -bar function levels off at ~ 0.4 , indicating that ML is not the predominant species in the solution.

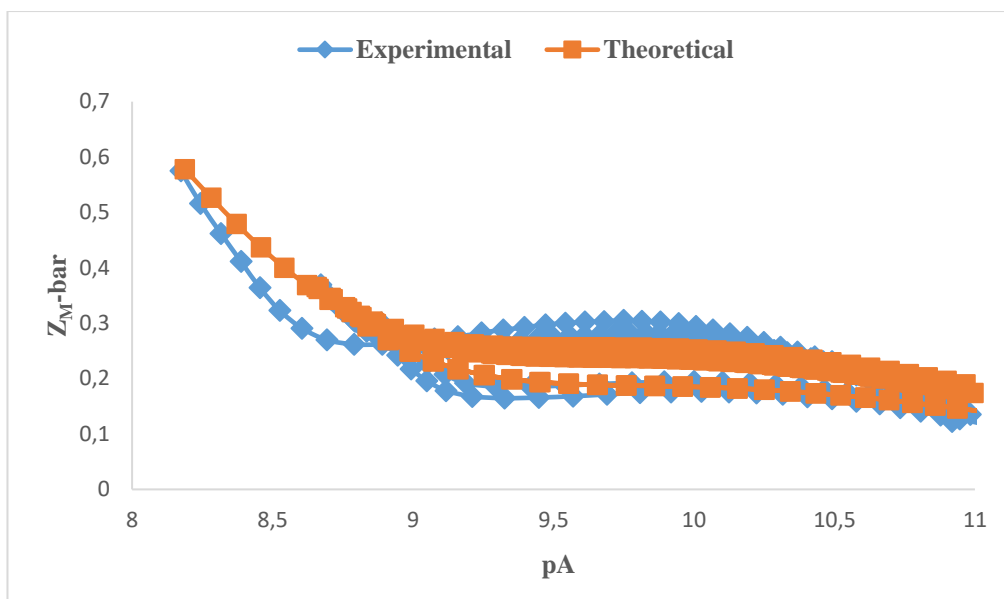


Figure 3.3: $Z_M\text{-bar}$ as a function of pA for Cu(II) ISO complex.

The deprotonation function ($Q_M\text{-bar}$) in Figure 3.4 shows that at a pH of approximately 2.91, the $Q\text{-bar}$ is greater than zero indicating that complexation has commenced. ISO has two dissociable protons, and it loses one upon complexation with Cu(II).

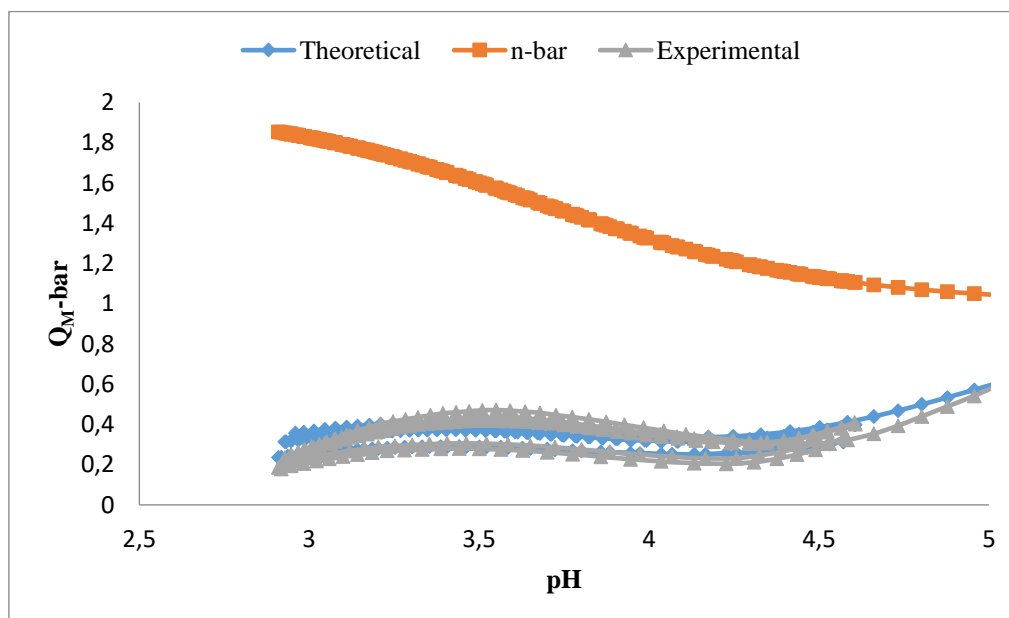


Figure 3.4: $Q_M\text{-bar}$ as a function of pH for the Cu(II) ISO complex.

The reproducibility of repeat titrations and excellent agreement, at different metal to ligand ratios, between the theoretical and experimental formation and deprotonation function curves

gives confidence to the result. The stability constants are given in Table 3.2. The stability constant $\log K$ of 6.52 has been reported in literature for the CuISO complex at 30 °C and $I=0.10 \text{ M NaClO}_4$.³⁰ The standard deviation is reasonably low. The Hamilton R_f^H factor indicates that the model is a good description of the equilibria occurring in solution.

Table 3.2: Stability constants ($\log \beta_{pqr}$) for Cu(II) ISO $\beta_{pqr} = [M_p L_q H_r] / [M]^p [L]^q [H]^r$, $I=0.15 \text{ mol dm}^{-3}$ (NaCl), $T = 25 \text{ }^\circ\text{C}$. S. dev. denotes standard deviation in $\log \beta_{pqr}$; R_f^H is the Hamilton R-factor and R_{lim}^H its limit, n_T is the number of titrations, (n_p) is the number of titration points.

Complexes	P	q	r	$\log \beta_{pqr}$	S. dev.	R_f^H	R_{lim}^H	$n_T(n_p)$
CuISOH	1	1	1	13.77	0.007			
CuISO	1	1	0	8.98	0.009	0.009	0.003	5(200)

The speciation graph for Cu(II) ISO is given in Figure 3.5. Only MLH and ML species are formed, MLH being the more stable species. Formation of precipitate was observed at pH above 4.8.

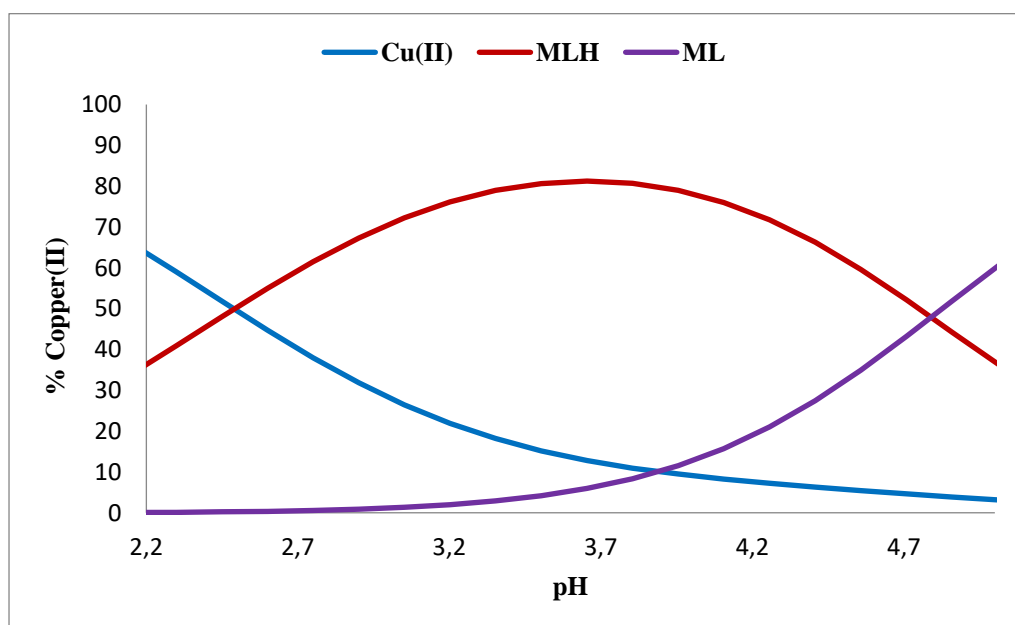


Figure 3.5: The distribution curve for the Cu(II) ISO complex (metal to ligand ratio 1:1).

3.5.1.3 Nickel complexation

Z_M -bar for Ni(II) ISO as a function of pA is given in Figure 3.6. Note that this curve is very different from the one obtained with Cu(II). The main reason for this is the pH. In the case of Ni(II), the titration could be continued to pH 11, whereas with Cu(II) precipitation occurred above pH 5. The hump at pA 10 indicates the presence of a protonated species, while the fanning back at pH 4.9 is indicating the formation of hydroxy species. ISO has two dissociable protons, but one was lost upon complexation with Ni(II) (Figure 3.6).

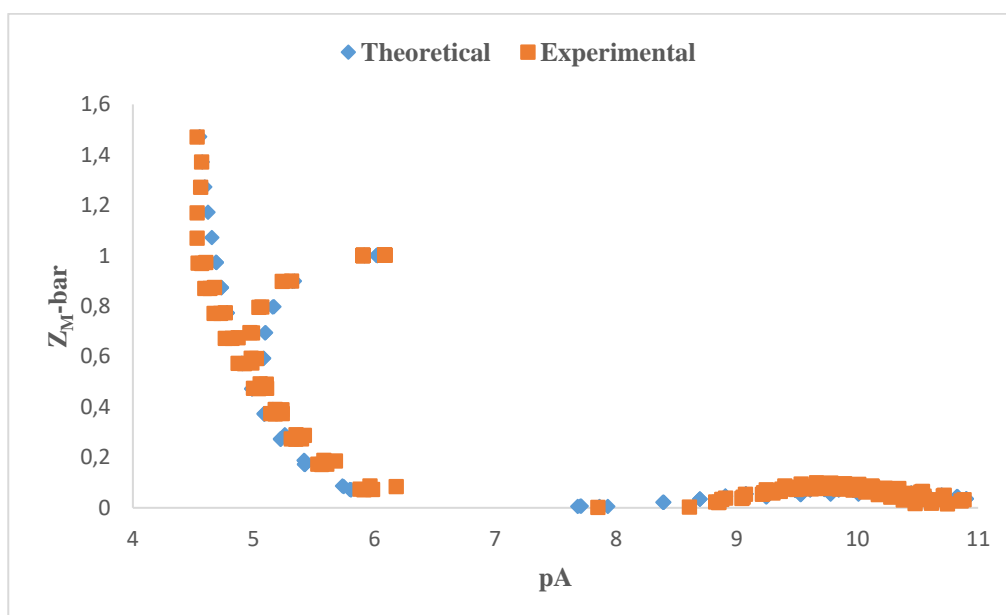


Figure 3.6: Z_M -bar as a function of pA for Ni(II) ISO complex.

The deprotonation function Q_M -bar for Ni(II) ISO complex is shown in Figure 3.7. At pH 5-7 the Q -bar levels off at zero indicating that no further complexation takes place in this pH range. The bar rises above n -bar in the pH range of 8.9 and 9.9 indicating the formation of the hydroxo species.

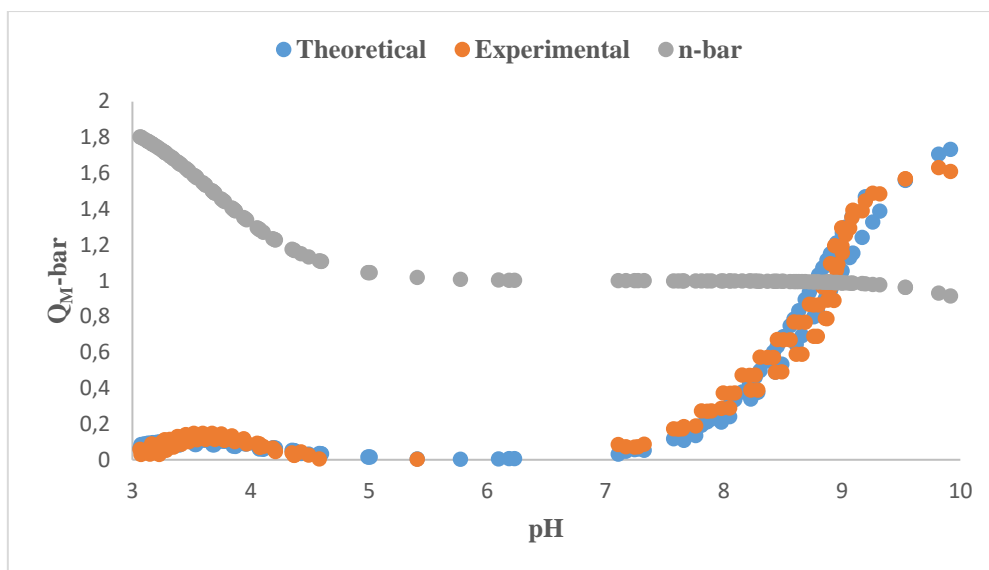


Figure 3.7: Q_M -bar as a function of pH for Ni(II) ISO complex.

Species formed between Ni(II) and ISO and their stability constants are given in Table 3.3. The reproducibility of the titration results and agreement between the theoretical and experimental formation and deprotonation functions at the different metal to ligand ratios gives confidence to the model. A stability constant $\log K$ of 5.11 has been reported in literature for the NiISO complex at 30 °C and $I = 0.10 \text{ M NaClO}_4$.³⁰

Table 3.3: Stability constants ($\log \beta_{pqr}$) for Ni(II) ISO complex $\beta_{pqr} = [M_p L_q H_r] / [M]^p [L]^q [H]^r$, $I = 0.15 \text{ mol dm}^{-3}$ (NaCl), $T = 25 \text{ }^\circ\text{C}$. S. dev. denotes standard deviation in $\log \beta_{pqr}$; R_f^H is the Hamilton R-factor and R_{lim}^H its limit, n_T is the number of titrations, (n_p) is the number of titration points.

Complexes	P	q	r	$\log \beta_{pqr}$	S. dev.	R_f^H	R_{lim}^H	$n_T(n_p)$
NiISOH	1	1	1	12.92	0.02			
NiISO	1	1	0	4.92	0.01	0.015	0.003	5(146)
NiISOH ₋₁	1	1	-1	-4.04	0.01			

Figure 3.8 shows the speciation graph for 1:1 Ni(II) ISO in the pH range of 2.0 to 11. The MLH species forms in the pH range 2.1 to 9.8 and a maximum of 61% was observed, while ML forms

between pH 6.6 and pH 9.2 and reached a maximum of 63%. About 96% of MLH_1 was established between pH 7.8 and 10.5.

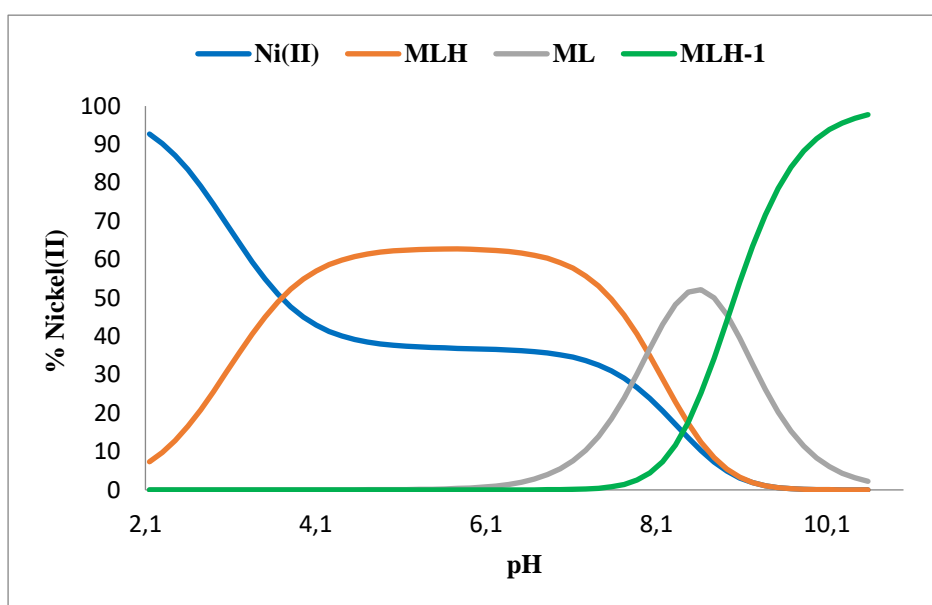


Figure 3.8: The distribution curve for the Ni(II) ISO complex (metal to ligand ratio 1:1).

3.5.1.4 Zinc complexation

Z_M -bar as a function of pA is shown in Figure 3.9. The complexation curves for various metal to ligand ratios start at pA= 6.7. The formation function rises and fans back, thus indicating the formation of hydroxyl complex species in solution. The agreement between the theoretical and experimental complex formation curves at the different metal to ligand ratios support the potentiometric model chosen in data analysis.

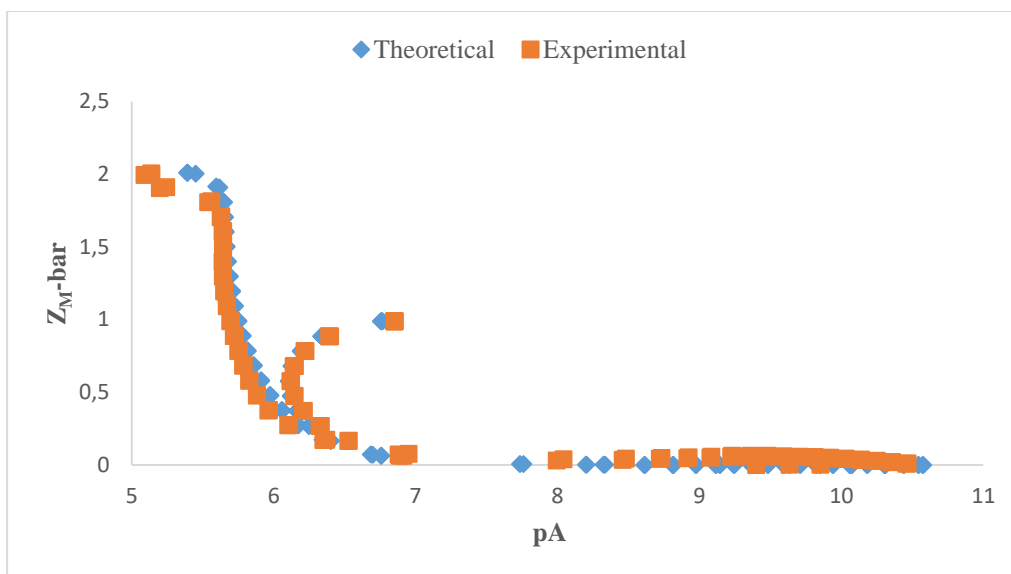


Figure 3.9: $Z_{M\text{-bar}}$ as a function of pA for Zn(II) ISO complex.

$Q_{M\text{-bar}}$ for Zn(II) ISO titration is depicted in Figure 3.10. At pH 3.31 the deprotonation function value of zero indicates that no protons have been displaced due to complexation. For pH values above 6.36, the deprotonation function $Q_{M\text{-bar}}$ rises to intersect the protonation curve, $n\text{-bar}$, at a pH of 7.75, reaching a maximum of about 1.09. ISO has two dissociable protons, and it loses one proton upon complexation with Zn(II). The system consists mostly of hydroxo species from pH 7.7 to pH 10.1.

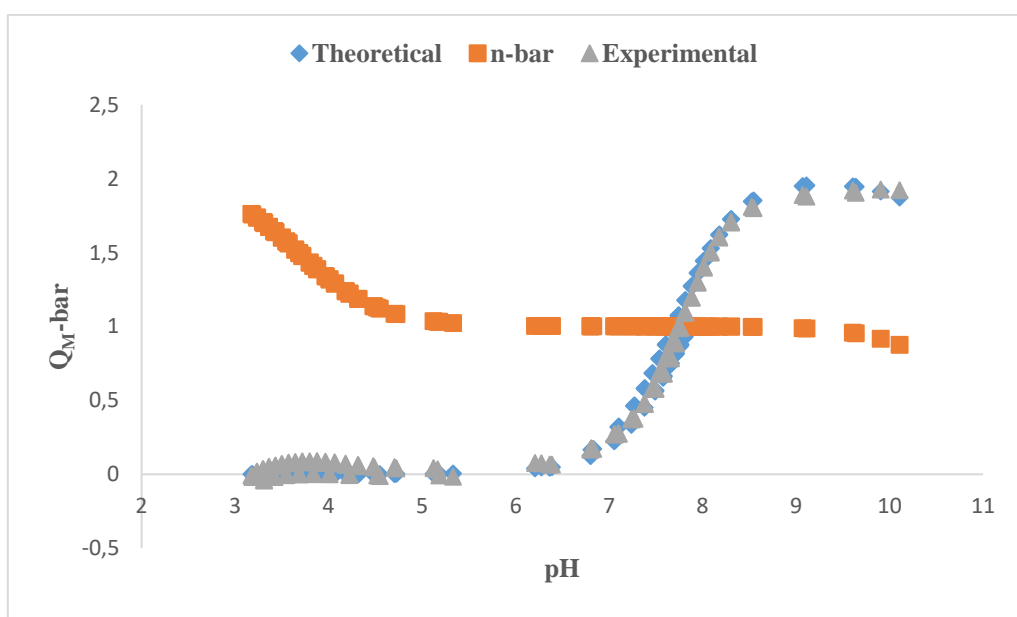


Figure 3.10: $Q_{M\text{-bar}}$ as a function of pH for Zn(II) ISO complex.

Table 3.4 shows that two species were obtained in the complexation of Zn(II) with ISO and their stability constants are shown. The standard deviations of the $\log \beta_{pqr}$ values obtained from the potentiometry are reasonably low. A stability constant $\log K$ of 5.71 has been reported in literature for the CuISO complex at 30 °C and $I = 0.10 \text{ M NaClO}_4$.³⁰

Table 3.4: Stability constants ($\log \beta_{pqr}$) for Zn(II) ISO complex $\beta_{pqr} = [M_p L_q H_r] / [M]^p [L]^q [H]^r$, $I = 0.15 \text{ mol dm}^{-3}$ (NaCl), $T = 25 \text{ °C}$. S. dev. denotes standard deviation in $\log \beta_{pqr}$; R_f^H is the Hamilton R-factor and R_{lim}^H its limit, n_T is the number of titrations, (n_P) is the number of titration points.

Complexes	P	q	r	$\log \beta_{pqr}$	S. dev.	R_f^H	R_{lim}^H	$n_T(n_P)$
ZnISO	1	1	0	5.50	0.03			
ZnISOH ₋₁	1	1	1	-2.10	0.01	0.02	0.005	4(118)

Figure 3.11 shows the distribution of the three species of the ligand from pH 2.2 to 10.2. 40% of Zn(II) existed in ML form at pH 7.4, and a maximum of 99% of MLH₋₁ is observed at pH 9.8. The CuISO species is more stable than the NiISO and ZnISO species. The good agreement between the theoretical and experimental formation and deprotonation functions, as well as low standard deviations and Hamilton R-factors, confirm the validity of this model.

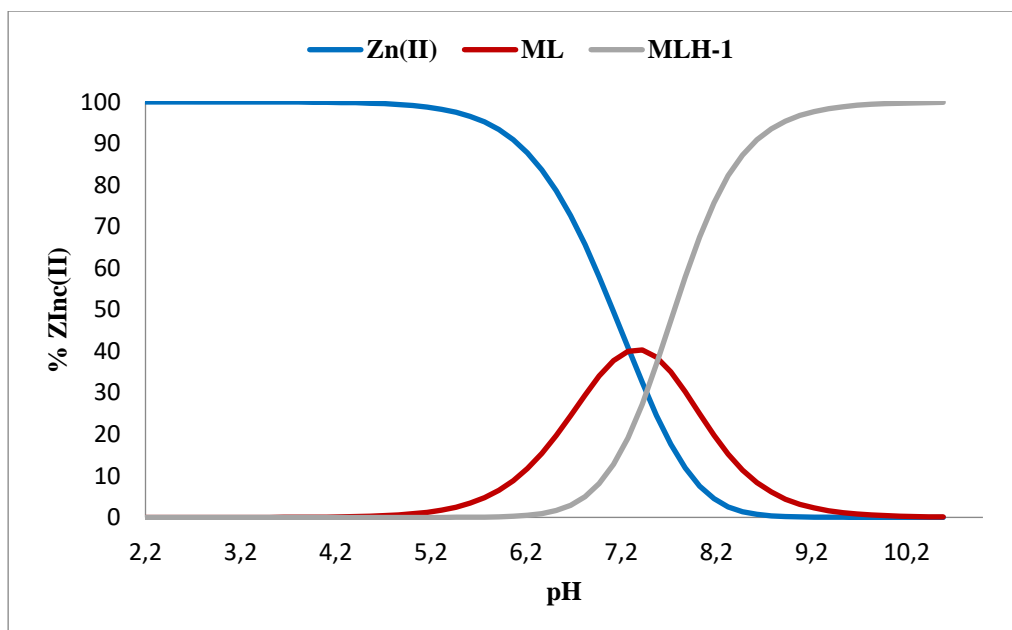


Figure 3.11: The distribution curve for the Zn(II) ISO complex (metal to ligand ratio 1:1).

3.5.1.5 Discussion

The equilibrium constants for the complexation of Cu(II), Ni(II) and Zn(II) with ISO are given in Tables 3.2-3.4. Log K values of 6.52, 5.11 and 5.71 have been reported in the literature for ML species of the Cu(II), Ni(II) and Zn(II) complexes of ISO.³⁰ These values are about 0.19-1.73 log units larger than the values obtained in our work. The difference in these values may be attributed to the fact that Magare and co-workers³⁰ used a model different from what we proposed in our study. A good agreement between the theoretical and experimental formation and deprotonation constant as well as a low standard deviation and Hamilton R-factors confirms the validity of the model used in the present study.

The equilibrium constant for the deprotonation of CuISOH is ($\log \beta_{MLH} - \log \beta_{ML} = (13.77 - 8.98)$) i.e. 4.79, Table 3.5, which is similar to the pK_a of pyridine (5.21).³¹ This suggests that it is the pyridine that is deprotonated to form ML from MLH. At pH 3.5 CuISOH is the predominant species.

Table 3.5: Equilibrium constants of the reaction of Cu(II), Ni(II) and Zn(II) with ISO.

The reaction progress	Cu(II)	Ni(II)	Zn(II)
$MLH \rightleftharpoons ML + H^+$	4.79	8.00	-
$ML \rightleftharpoons MLH_{-1} + H^+$	-	8.96	7.60

The $\log \beta$ value for CuISO is 8.98; this is much higher than the stability constants of $[Cu(II)(NH_3)]^{2+}$ (4.8), $[Cu(II)(pyridine)]$ (2.49), and $[Cu(II)(benzylhydrazide)]$ (1.73), suggesting that the ligand is not monodentate.²⁷ The $\log K$ values for pyridine complexation with Cu(II) and Ni(II) are 2.49 and 1.87 respectively. These are lower than the values obtained in this study indicating that the coordination for the CuL and NiL is not *via* the pyridine nitrogen.²⁷ The $\log \beta$ value is quite close to the $\log \beta$ of $[Cu(II)(en)]^{2+}$ (10.5) suggesting that the ligand has a similar binding mode. The formation equilibria for Ni(II) show that this metal ion forms relatively stable complexes with ISO, although its stability is lower than that of Cu(II). Trends in the equilibrium constant are in accordance with the Irving-Williams stability series.¹⁴ The ligand forms a quite stable complex with the metals and could be more selective for Cu(II) than Zn(II) and Ni(II).

For example, the stability constants ($\log \beta$ values) of the ML species of ISO with Cu(II), Ni(II) and Zn(II) are 8.98, 4.92 and 5.50 respectively. The difference in stability of some 3.5-4 log units is observed between Cu(II) and the *in vivo* competitors Ni(II) and Zn(II). The explanation for this observation is that the arrangement of the ligand donor atom is such that the metal ion is constrained to adopt a square-planar coordination geometry. As observed in most simple systems³² and metalloenzymes,³³ Zn(II) prefers a tetrahedral coordination geometry.

The proposed structure for this complex is given in Figure 3.12. CuLH is formed by the coordination of the isoniazid carbonyl oxygen and hydrazide amino nitrogen atoms, while the pyridine group is protonated. The donor atom forms a five-membered chelate ring.

In the deprotonation of ML to form MLH₁, for Ni(II) and Zn(II), the calculated pK_a ($\log \beta_{ML} - \log \beta_{MLH-1}$) values were 8.96 and 7.60 respectively. The value of 8.96 is 0.9 log units lower than the first hydrolysis constant of Ni(II) (pK_a-OH) of 9.86.³⁴ Furthermore, the pK_a value of the formation of MLH₁ species for Zn(II) was 1.57 log units lower than the first hydrolysis constant of Zn(II) (pK_a-OH) = 9.17.³⁴ The values of the hydrolysis constant of the metal suggest that the deprotonation comes from a coordinated water molecule in the complex.

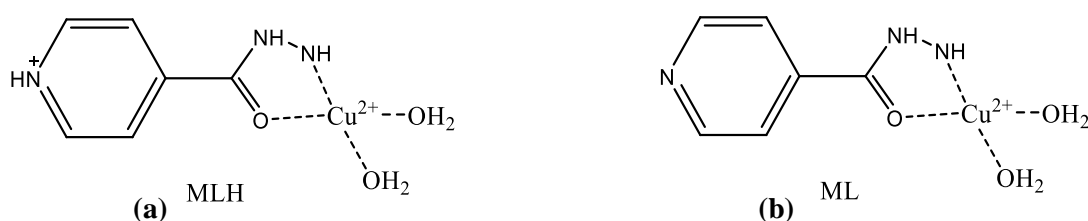


Figure 3.12: Possible structures for MLH and ML of the Cu(II) ISO system.

3.5.2 Ethambutol (EMB)

3.5.2.1 Protonation

The Z_{H-bar} function for protonation of EMB is given in Figure 3.13. The variation of the mean number of protons bound to the ligand as a function of pH is given. At pH between 10.48 and 11.00, Z_{H-bar} is 0, and the ligand is fully deprotonated. From pH 10.14 to 8.79 Z_{H-bar} rises, indicating the protonation of the ligand from L-form to the LH-form in this pH range. From 8.54 to 7.51, Z_{H-bar} was constant at approximately $Z_{H-bar} = 1$. The graph rises again from pH 7.5 to 5.8 and then levels up at pH 2, indicating the addition of another proton. Protonation constants of EMB were estimated from the half Z_{H-bar} values, $\log K_{LH1} = 9.63$, $\log K_{LH2} = 6.52$, and were used as the starting values in ESTA.

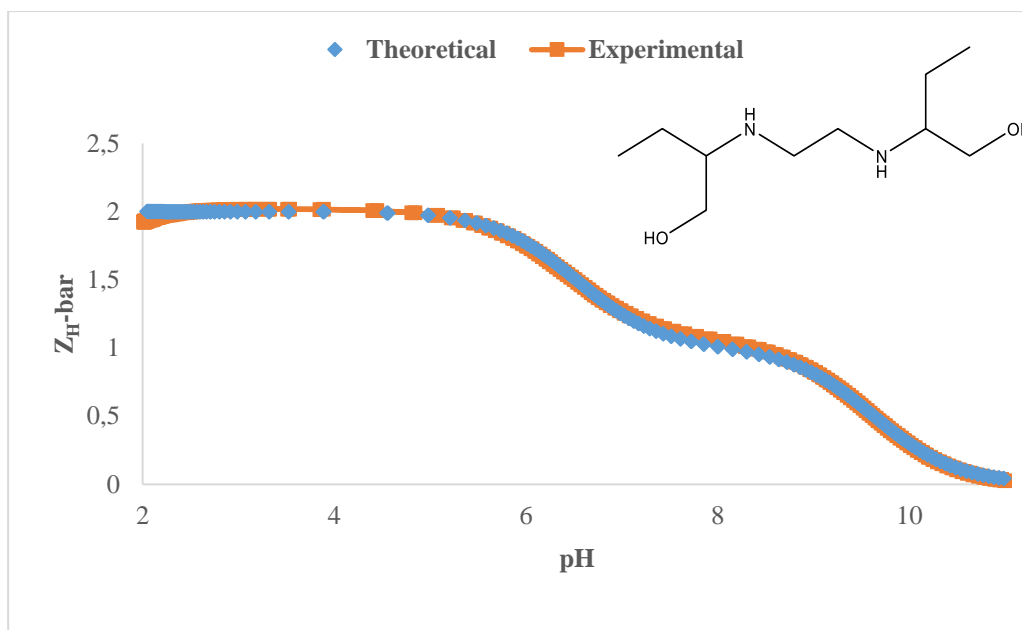


Figure 3.13: $Z_{\text{H}}\text{-bar}$ as a function of pH for the protonation of EMB.

The final $\log \beta$ values are given in Table 3.6. The standard deviations were small, and the model is accurate since Hamilton R-factors are low, giving confidence in the results. The theoretical and experimental curves are well superimposable, supporting the protonation model.

Table 3.6: Stability constants ($\log \beta_{\text{pqr}}$) for EMB $\beta_{\text{pqr}} = [\text{M}_p\text{L}_q\text{H}_r]/[\text{M}]^p[\text{L}]^q[\text{H}]^r$, $I = 0.15 \text{ mol dm}^{-3}$ (NaCl), $T = 25 \text{ }^\circ\text{C}$. S. dev. denotes standard deviation in $\log \beta_{\text{pqr}}$; R_f^H is the Hamilton R-factor and R_{lim}^H its limit, n_{T} is the number of titrations, (n_{p}) is the number of titration points.

Ligand	P	q	r	$\log \beta_{\text{pqr}}$	S. dev.	R_f^H	R_{lim}^H	$n_{\text{T}}(n_{\text{p}})$
EMB-H	0	1	1	9.63	0.005	0.009	0.002	2(319)
EMB-H ₂	0	1	2	16.15	0.007			

The speciation for EMB protonation titration is given in Figure 3.14. The plots indicate that the ligand solution has a mixture of mono- and di-protonated species. The mono-protonated species were dominant at higher pH, and the neutral form of the ligand protonates below pH 6.0. It confirms that LH^+ dominates in the pH range 5.3 -10.7. At pH 10.84 there is already

more free ligand than LH in solution. Below pH 5.2, the predominant species is $[LH_2]^{+2}$ in an aqueous solution of this ligand.

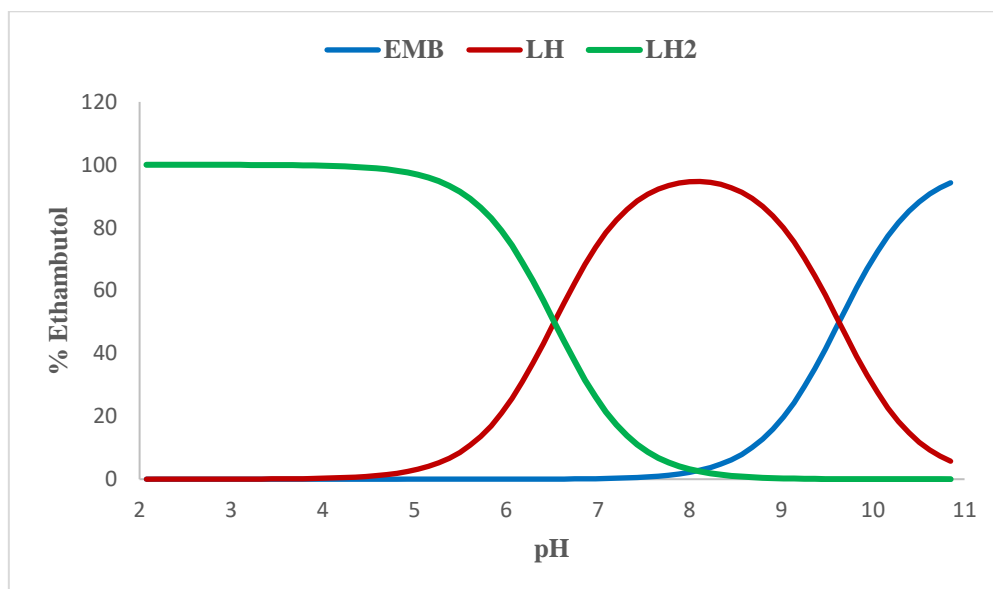


Figure 3.14: Distribution curve for the protonation of EMB.

EMB shows two pK_a values of 9.63 and 6.52 arising from the two amino nitrogen groups. The results obtained are higher than literature values, namely $\log K_{LH1}$ of 9.15 and $\log K_{LH2}$ of 6.10.²⁷ This can probably be attributed to the different experimental conditions for the latter determinations, namely $T = 30\text{ }^\circ\text{C}$ and $I = 0.1\text{ mol dm}^{-3}$.

3.5.2.2 Copper complexation

Figure 3.15 shows that the complex formation function ($Z_{M\text{-bar}}$) levels off at a value of ≈ 1.0 indicating the presence of CuEMB as a major species. At higher pH, Z_{bar} rise above 2, showing the presence of $\text{Cu}(\text{EMB})_2$. It is dependent on component ratios and concentration, suggesting a complex stoichiometry of 1:1 and 1:2. As the titration continues, the curves rise steeply and fan back indicating the formation of hydroxo complex species.¹²

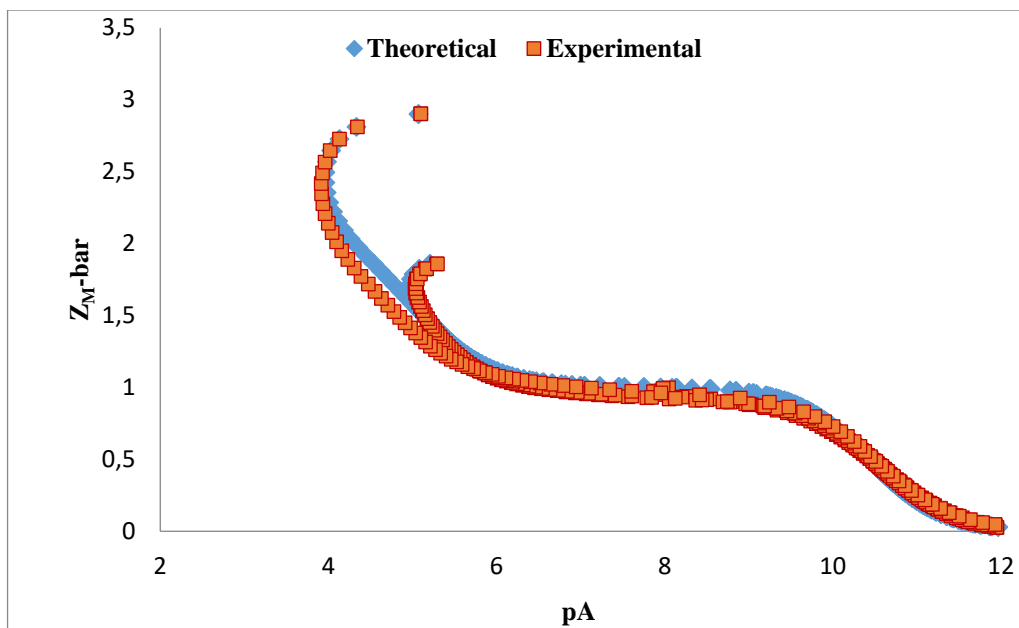


Figure 3.15: $Z_M\text{-bar}$ as a function of pA for the Cu(II) EMB complex.

The total number of dissociable protons on the ligand ($n\text{-bar}$) and the total number of protons lost upon complexation of Cu(II) with EMB ($Q\text{-bar}$) are shown in Figure 3.16. At a pH of 2.32, $Q_M\text{-bar}$ is zero indicating that complexation has not commenced. The function then increases rapidly in the pH range 3.51 to 5.70 to a maximum value of 1.78 indicating that approximately two protons are lost due to complex formation. From pH 6.0 to 8.84 $Q_M\text{-bar}$ rises above the $n\text{-bar}$ indicating hydrolysis of the complex.

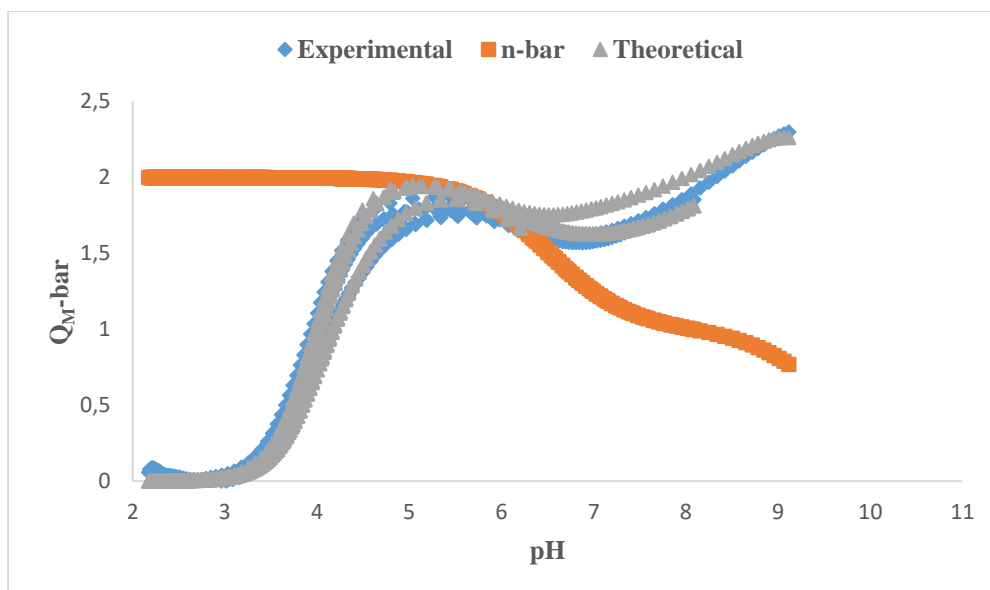


Figure 3.16: $Q_M\text{-bar}$ as a function of pH for the Cu(II) EMB complex.

The stability constants for the species formed between Cu(II) and EMB from pH 2 to pH 11 are given in Table 3.7. The theoretical and experimental data are superimposed. The standard deviations and the Hamilton R-factors are low giving confidence to the model. A $\log \beta$ value of 10.56 has also been reported for the ML species of the copper complex.³⁵

Table 3.7: Stability constants ($\log \beta_{pqr}$) for Cu(II) EMB complex $\beta_{pqr} = [M_p L_q H_r] / [M]^p [L]^q [H]^r$, $I = 0.15 \text{ mol dm}^{-3}$ (NaCl), $T = 25 \text{ }^\circ\text{C}$. S. dev. denotes standard deviation in $\log \beta_{pqr}$; R_f^H is the Hamilton R-factor and R_{lim}^H its limit, n_T is the number of titrations, (n_p) is the number of titration points.

Complexes	p	q	r	$\log \beta_{pqr}$	S. dev.	R_f^H	R_{lim}^H	$n_T(n_p)$
CuEMB ₂	1	2	0	15.42	0.01			
CuEMB	1	1	0	10.43	0.005	0.01	0.002	5(569)
CuEMB ₂ H ₋₁	1	2	-1	6.65	0.01			
CuEMB ₂ H ₋₂	1	2	-2	-3.36	0.12			

The species distribution curve for the complexes of EMB and Cu(II) are shown in Figure 3.17. At pH 2.0, there is 100% of the free metal ion species. ML predominates over a wide pH range of 2.90-9.38. ML reaches a maximum of 99% at pH 5.31. At about pH 6.20, the CuEMB₂ complex starts to form reaching a maximum of 72% at pH 8.17. The proportion of CuEMB₂

began to decrease from pH 8.62. At pH 7.72 the CuEMB_2H_1 species starts to form at the expense of CuEMB_2 reaching a maximum of 64% at pH 9.5. From pH 9.0 formation of CuEMB_2H_2 commenced and it attained a maximum of 84% at pH 10.73.

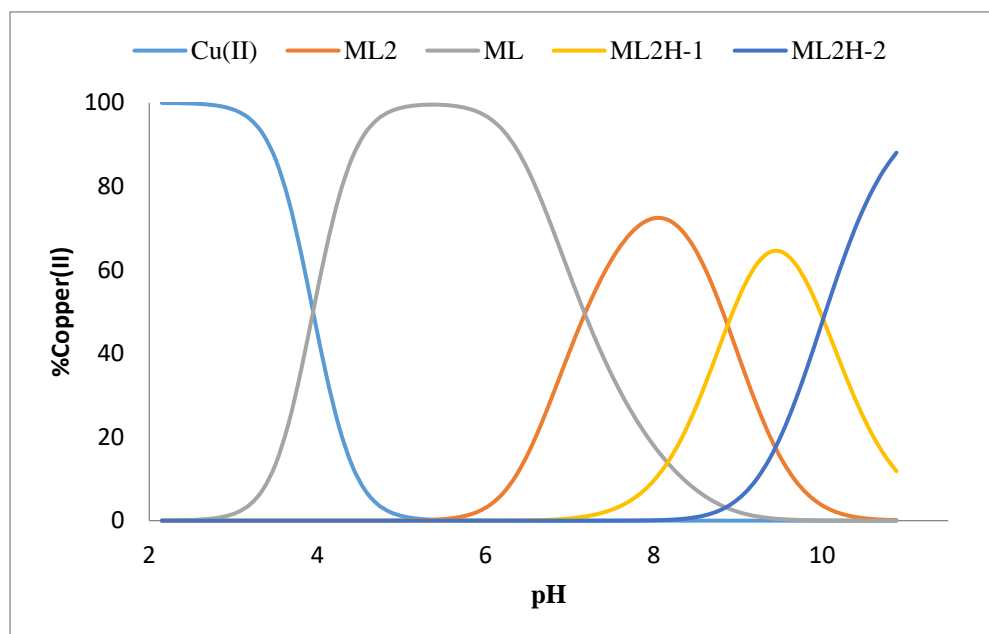


Figure 3.17: The distribution curve for the Cu(II) EMB complex (metal to ligand ratio 1:2).

3.5.2.3 Nickel complexation

Z_M -bar for Ni(II)EMB titrations is shown in Figure 3.18. The complexation curves for various metal to ligand ratios start at $\text{pA} = 8.4$; the formation function rises and fans back indicating the formation of hydroxo or mixed hydroxo complex species in solution. The conformity between the theoretical and practical formation curves at the different metal to ligand ratios supports the potentiometric model chosen in data analysis. EMB has two dissociable protons, and it loses both upon complexation with Ni(II) .

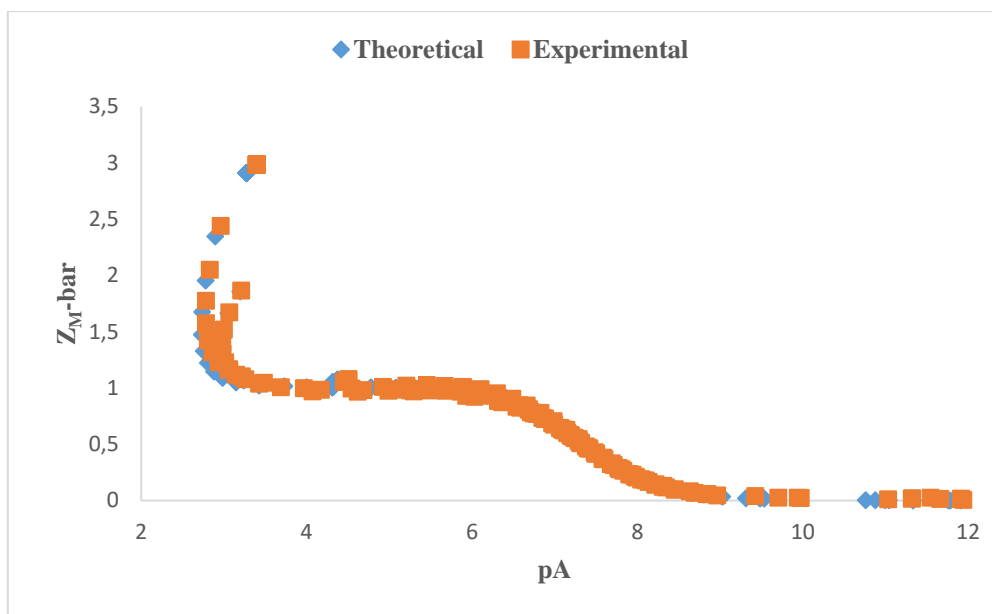


Figure 3.18: $Z_M\text{-bar}$ as a function of pA for the Ni(II) EMB complex.

Figure 3.19 shows that at pH 2.33, the deprotonation function $Q\text{-bar}$ is zero and no proton has been displaced due to complexation. For pH values above 4.89, $Q\text{-bar}$ rapidly rises to intersect the protonation curve, $n\text{-bar}$, at a pH of 6.33, reaching a maximum value of 1.62. The falling of the curves at about 6.82 shows that complexation is complete. Above pH 9, the curve rises indicating the formation of hydroxo species. It is noteworthy that in the case of the Ni(II) with EMB, metal to ligand ratio 1:2 was tried but the ML_2 species was always rejected.

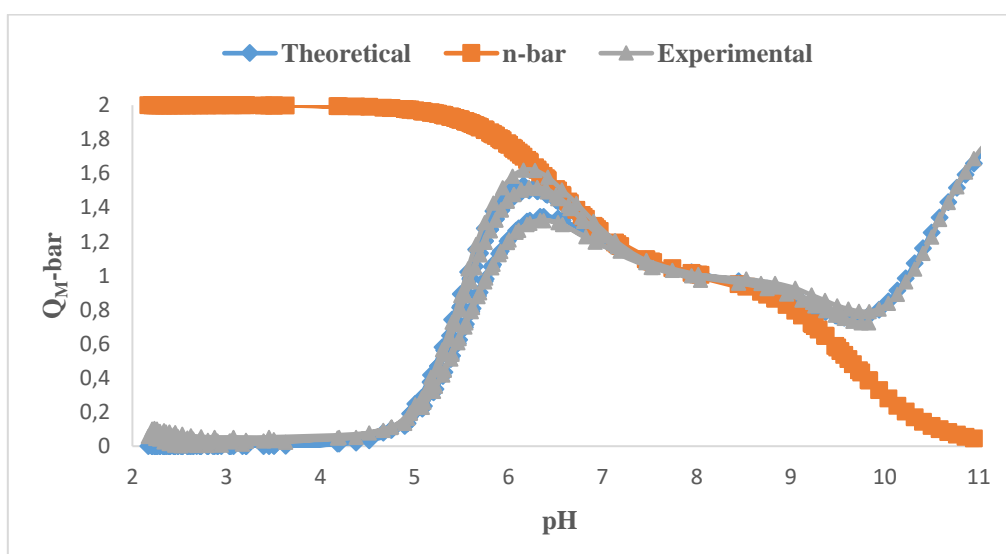


Figure 3.19: $Q_M\text{-bar}$ as a function of pH for the Ni(II) EMB complex.

The agreement between the theoretical and experimental complex formation curves at different metal to ligand ratios supports the potentiometric model chosen in data analysis. The stability constants are given in Table 3.8. The calculated formation constants have low standard deviation and are comparable with those of Cu(II) complexation. The Hamilton R-factors indicate that the model is a good description of the equilibria occurring in solution.

Table 3.8: Stability constants ($\log \beta_{pqr}$) for Ni(II) EMB complex $\beta_{pqr} = [M_p L_q H_r] / [M]^p [L]^q [H]^r$, $I=0.15$ mol dm⁻³ (NaCl), $T = 25$ °C. S. dev. denotes standard deviation in $\log \beta_{pqr}$; R_f^H is the Hamilton R-factor and R_{lim}^H its limit, n_T is the number of titrations, (n_p) is the number of titration points.

Complexes	P	q	r	$\log \beta_{pqr}$	S. dev.	R_f^H	R_{lim}^H	$n_T(n_p)$
NiEMB	1	1	0	7.37	0.003			
NiEMBH ₁	1	1	-1	-2.84	0.01	0.006	0.002	5(233)
NiEMBH ₂	1	1	-2	-13.42	0.01			

The speciation graphs in Figure 3.20 show that ML predominates over a wide pH range of 5.11-10.13. ML reaches a maximum of 99% at pH 7.87. At about pH 9.0-10.58, there was the formation of MLH₁ and MLH₂, and maxima of 41% were observed.

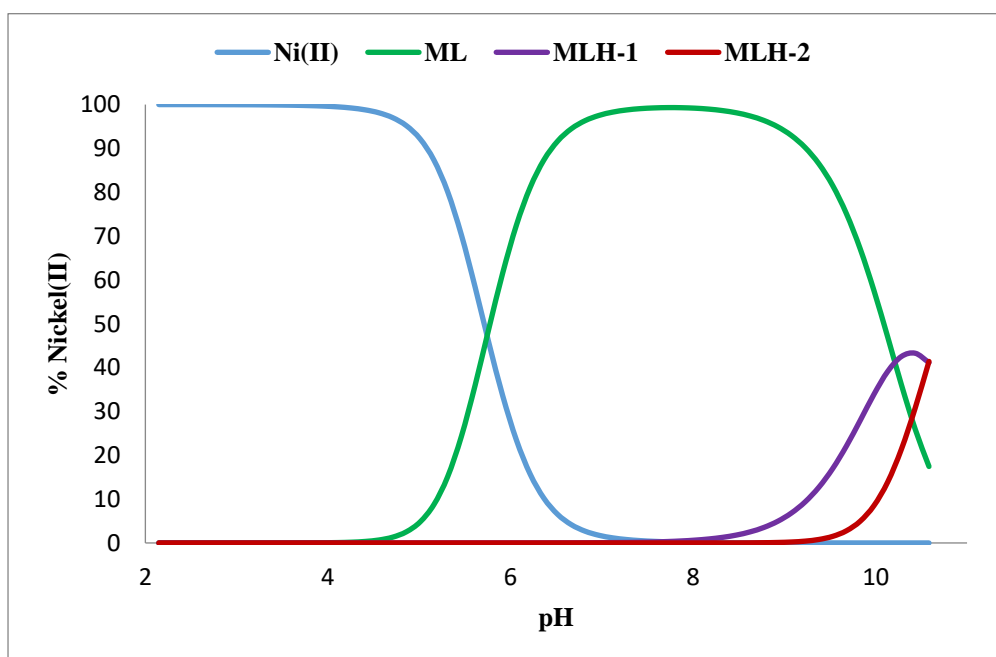


Figure 3.20: The distribution curve for the Ni(II) EMB complex (metal to ligand ratio 1:1).

3.5.2.4 Zinc complexation

Figure 3.21 shows the complex formation function ($Z_M\text{-bar}$) level off at the value of ≈ 1.0 for mononuclear species formation indicating that ZnEMB is the predominant species.

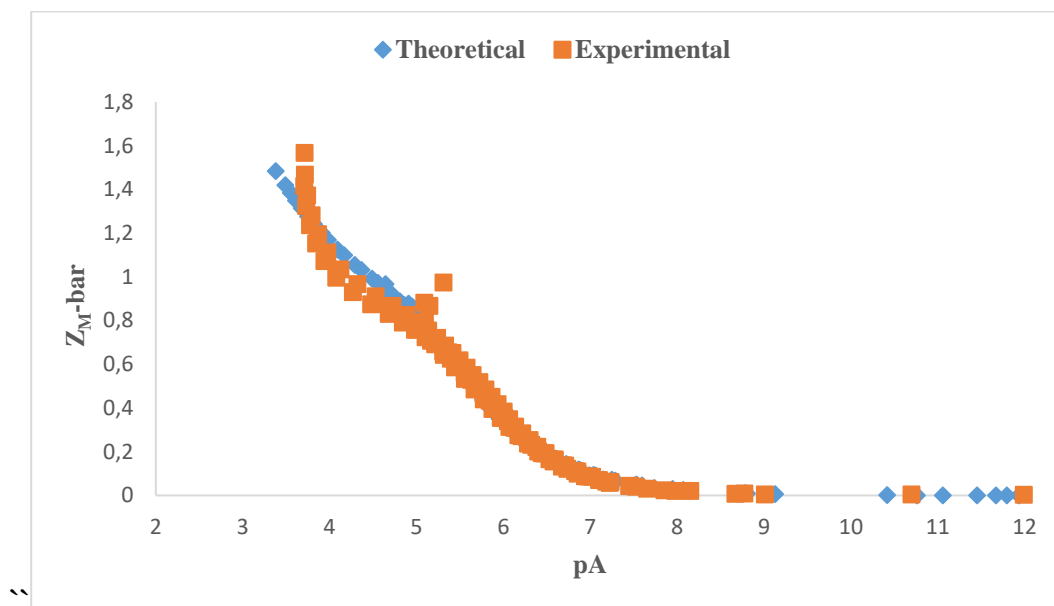


Figure 3.21: $Z_M\text{-bar}$ as a function of pA for the Zn(II) EMB complex.

The total number of dissociable protons on the ligand ($n\text{-bar}$) and the total number of protons lost upon complexation of Zn(II) with EMB are shown in Figure 3.22. In the pH range 2.3-5.65 the $Q\text{-bar}$ value of zero indicates that no protons have been displaced due to complexation. At pH value above 5.8, the deprotonation function $Q\text{-bar}$ rapidly rises to intersect the protonation curve, $n\text{-bar}$, at a pH of 7.69, with a maximum value of about 1.09. The rising of the curves at about pH 8.4 shows that a complex is still forming. The agreement between the theoretical and experimental complex formation curves at the different metal to ligand ratios supports the potentiometric model chosen in data analysis.

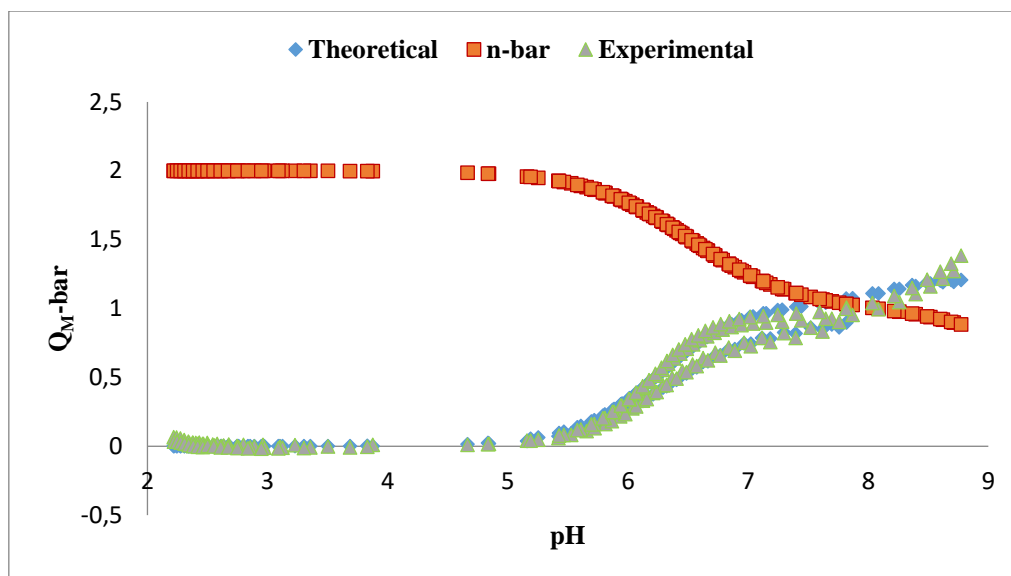


Figure 3.22: Q_M -bar as a function of pH for the Zn(II)EMB complex.

The stability constants ($\log \beta_{pqr}$) are given in Table 3.9. The standard deviations are small, and the Hamilton R-factor limits are low giving confidence to the chosen model. It is worth noting that when Q -bar rises above the n -bar curve, it indicates hydrolysis of the metal ion species, forming the species MLH_{-1} . In this instance, different models were tried, but this species was always rejected.

Table 3.9: Stability constants ($\log \beta_{pqr}$) for Zn(II) EMB complex $\beta_{pqr} = [M_p L_q H_r] / [M]^p [L]^q [H]^r$, $I = 0.15 \text{ mol dm}^{-3}$ (NaCl), $T = 25 \text{ }^\circ\text{C}$. S. dev. denotes standard deviation in $\log \beta_{pqr}$; R_f^H is the Hamilton R-factor and R_{lim}^H its limit, n_T is the number of titrations, (n_p) is the number of titration points.

Complexes	P	q	r	$\log \beta_{pqr}$	S. dev.	R_f^H	R_{lim}^H	$n_T(n_p)$
ZnEMB	1	1	0	5.72	0.008			
ZnEMB ₂	1	2	0	9.044	0.03	0.01	0.002	4(171)
ZnEMBH	1	1	1	11.86	0.02			

The species distribution curve for the complexation of EMB and Zn is shown in Figure 3.23. At pH 2.2, there is 100% of the free metal ion species. Around pH 4.70, the ZnEMBH species began to form, reaching a maximum of 28%. The proportion began to fall at pH 6.0, where the

formation of ZnEMB commenced and reached a maximum of 84% in the solution; ZnEMB₂ was formed at the expense of ML species. The highest amount of ML₂ species present in the solution was 39%.

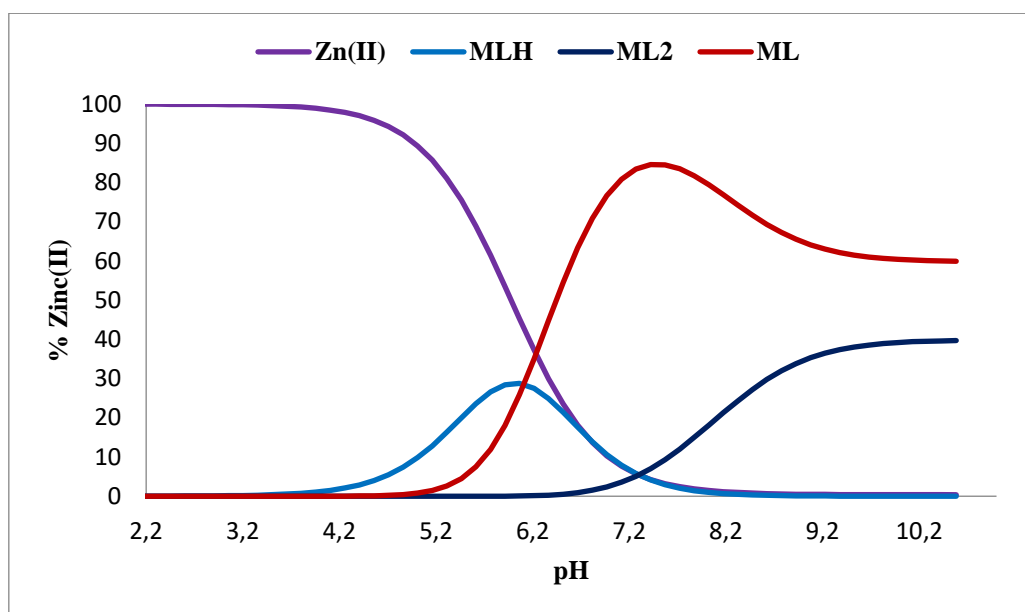


Figure 3.23: The distribution curve for the Zn(II) EMB complex (metal to ligand ratio 1:2).

3.5.2.5 Discussion

The equilibrium constants for the deprotonation of Cu(II), Ni(II) and Zn(II) with EMB are given in Table 3.10. The $\log \beta$ value for ML in Cu(II) EMB is 10.43 suggesting that the ligand has a similar binding mode as $[\text{Cu(II)(en)}]^{2+}$ (10.5).

Table 3.10: Equilibrium constants of the reaction of Cu(II), Ni(II) and Zn(II) with EMB

The reaction progress	Cu(II)	Ni(II)	Zn(II)
$\text{MLH} \rightleftharpoons \text{ML} + \text{H}^+$	-	-	6.14
$\text{ML} \rightleftharpoons \text{MLH}_{-1} + \text{H}^+$	-	10.21	-
$\text{MLH}_{-1} \rightleftharpoons \text{MLH}_{-2} + \text{H}^+$	-	10.58	-

$ML_2 \rightleftharpoons ML_2H_{-1} + H^+$	8.77	-	-
$ML_2H_{-1} \rightleftharpoons ML_2H_{-2} + H^+$	10.01	-	-

For ML, the coordination can take place through the two N atoms and two O atoms of the ligand. Comparing the $\log \beta$ value of Cu(EMB) (10.43) and that of $[Cu(II)(en)]^{2+}$ (10.5), it is observed that they are close, suggesting that the coordination mode is similar, i.e., through the 2N of the two amino groups of the ligand. If the OH is coordinated, it is expected that the $\log \beta$ value for Cu(EMB) would be greater than $\log \beta$ for Cu(en). Two proposed structures are shown in Figure 3.24. Based on the above argument the structure (b) is more favourable than (a). A similar binding mode has been reported for many Cu-N complexes.³⁶⁻⁴⁰

The $\log \beta$ value of ML_2 in solution is 15.42, and it compares well with the $\log \beta$ value for $[Cu(II)(en)_2]^{2+}$ (15.9), indicating similar coordination mode. The ML_2 can coordinate through the two amino nitrogen atoms from the two ligands. The calculated Cu(II)-assisted deprotonation constant associated with the formation of ML_2H_{-1} is the difference between $\log \beta_{ML_2}$ and $\log \beta_{ML_2H_{-1}}$ (8.77, Table 3.10). This could be due to loss of a proton from the coordinating water molecule since the pK_a is close to the hydrolysis constant of $[Cu(OH_2)_6]^{2+}$. In the formation of ML_2H_{-2} , there is also a loss of another proton from the coordinating water molecule ($ML_2H_{-1} \rightleftharpoons ML_2H_{-2} + H^+$) with $pK_a = 10.01$ (Table 3.10). The proposed structures for ML_2 , ML_2H_{-1} and ML_2H_{-2} are shown in Figure 3.25. The complexes contain five-membered rings and are quite stable. A noticeable feature about the complexation of EMB with Cu(II), Ni(II) and Zn(II) is the prevalence of the ML species. The difference in the stability observed between the metal ions with EMB was 3-4 log units, and the trend agrees with the Irving-Williams stability order for transition-metal complexes.¹⁴ The potentiometric data presented could be further supported by ESI-MS measurements in the future.

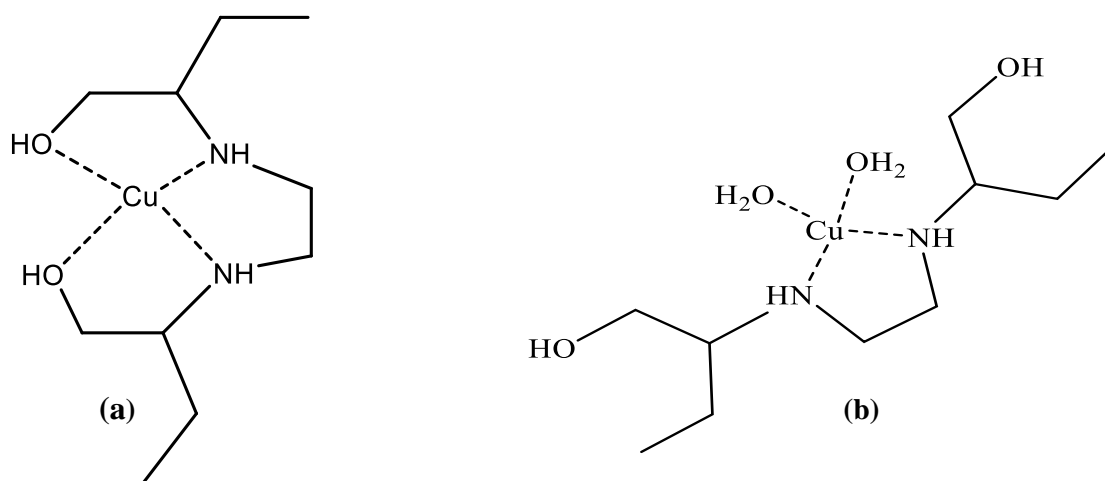


Figure 3.24: Possible structures for ML of the Cu(II) EMB system.

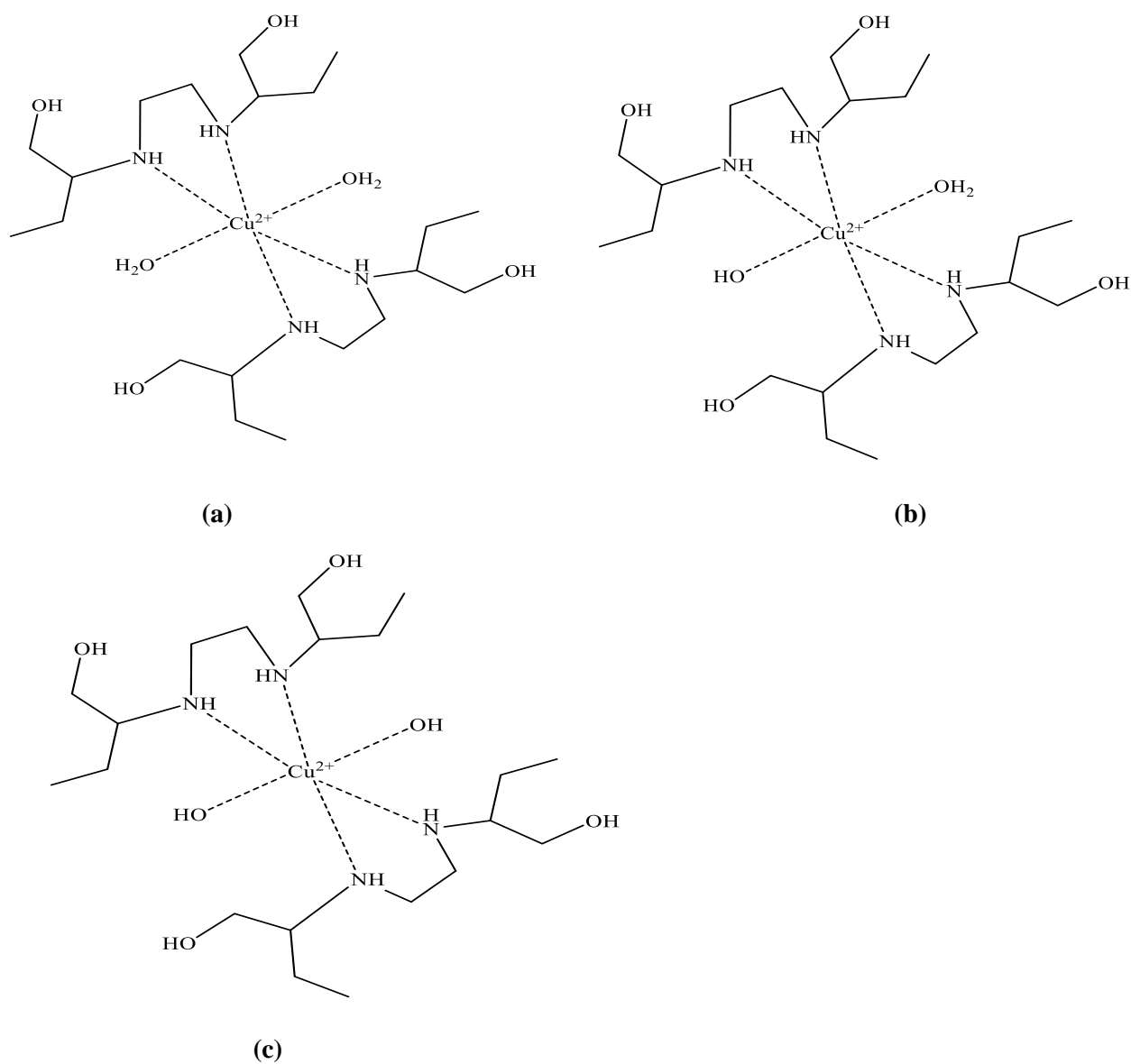


Figure 3.25: Possible structures for ML₂, ML₂H₁ and ML₂H₂ of the Cu(II) EMB system.

3.5.3 P-aminosalicylic acid (PAS)

3.5.3.1 Protonation

$Z_{\text{H}}\text{-bar}$ for protonation of PAS is given in Figure 3.26. The graph rises until it reaches $Z_{\text{H}}\text{-bar} = 1.28$ between pH 5.5 and 2.20, indicating that more than one proton has been added. Protonation constants of PAS were estimated from the half $Z_{\text{H}}\text{-bar}$ values, namely $\log K_{\text{LH1}} = 3.78$ and $\log K_{\text{LH2}} = 1.86$, which were used as the starting values in ESTA. The experimental and theoretical plots are well superimposed. This leads to confidence in the model.

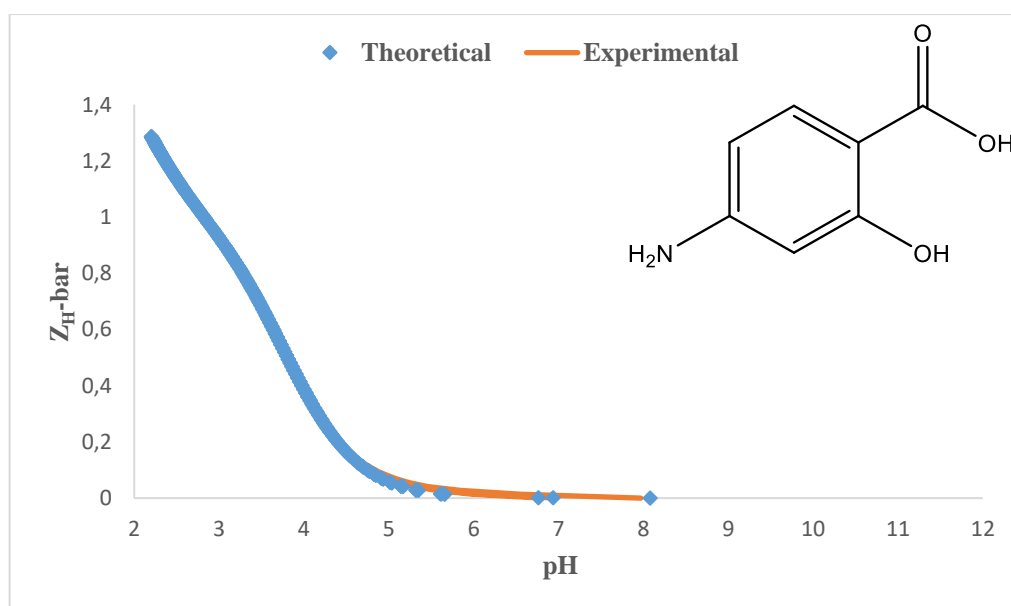


Figure 3.26: $Z_{\text{H}}\text{-bar}$ as a function of pH for the protonation of PAS.

Optimised $\log \beta$ values are given in Table 3.11. These values are lower than those reported in the literature (namely $\log \beta_{\text{LH1}} = 4.08$ and $\log \beta_{\text{LH2}} = 6.08$) at a temperature of 25 °C and ionic strength 0.10 M NaClO_4 .²⁷ The standard deviations were small, giving confidence in the results. The speciation for PAS protonation titration is given in Figure 3.27.

Table 3.11: Stability constants ($\log \beta_{pqr}$) for PAS $\beta_{pqr} = [M_p L_q H_r] / [M]^p [L]^q [H]^r$, $I = 0.15 \text{ mol dm}^{-3}$ (NaCl), $T = 25 \text{ }^\circ\text{C}$. S. dev denotes standard deviation in $\log \beta_{pqr}$; R_f^H is the Hamilton R-factor and R_{lim}^H its limit, n_T is the number of titrations, (n_p) is the number of titration points.

Ligand	p	q	r	$\log \beta_{pqr}$	S. dev.	R_f^H	R_{lim}^H	$n_T(n_p)$
PAS-H	0	1	1	3.78	0.002	0.007	0.001	3(419)
PAS-H ₂	0	1	2	5.64	0.005			

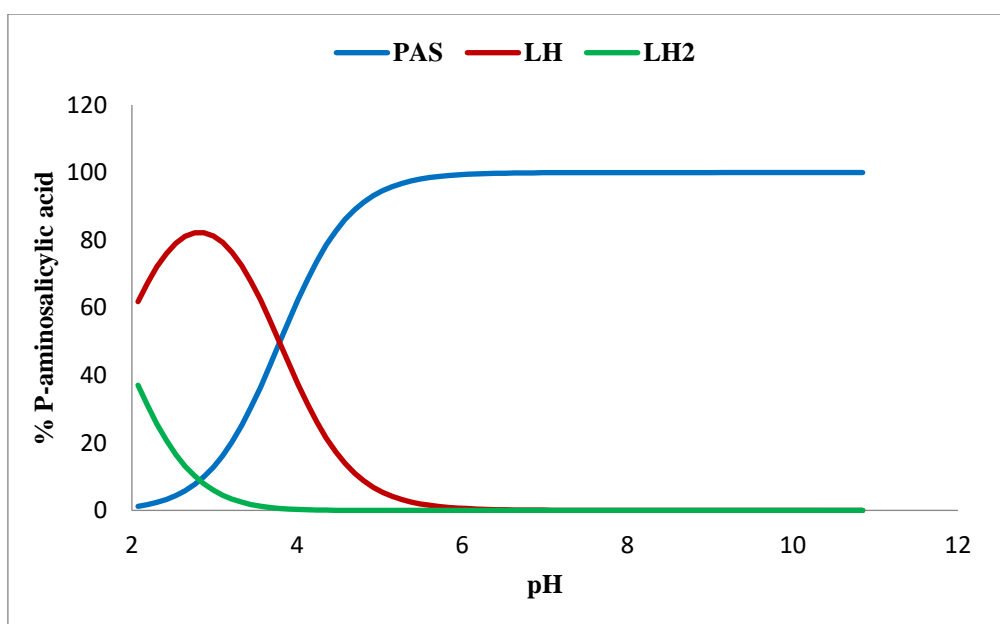


Figure 3.27: Distribution curve for the protonation of PAS.

The LH species predominates at pH between 2.5 and 3.5. Below pH 2.7, the predominant species is LH₂ in an aqueous solution of the ligand.

PAS has three protonation sites, but only two are observed for the pH under consideration. PAS shows two pK_a values of 3.78 and 1.85 arising from the carboxylic acid group and an amino group. The pK_a of the phenolic hydroxy group of the p-aminosalicylic acid is 13.74 as a result of the strong intramolecular hydrogen bond,⁴¹⁻⁴⁴ and could not be observed because it is higher than the pH under consideration.

3.5.3.2 Copper complexation

The formation function for Cu(II) PAS titration is given in Figure 3.28. Only three species were formed in this titration, CuPAS, CuPASH and CuPASH₁. The predominant species is CuPAS with $\log \beta_{ML} = 2.21$. R_f^H and R_{lim}^H are very low, and this gives confidence in the proposed model. There is a fanning back of the curve indicating the formation of hydroxo (CuPASH₁) species.

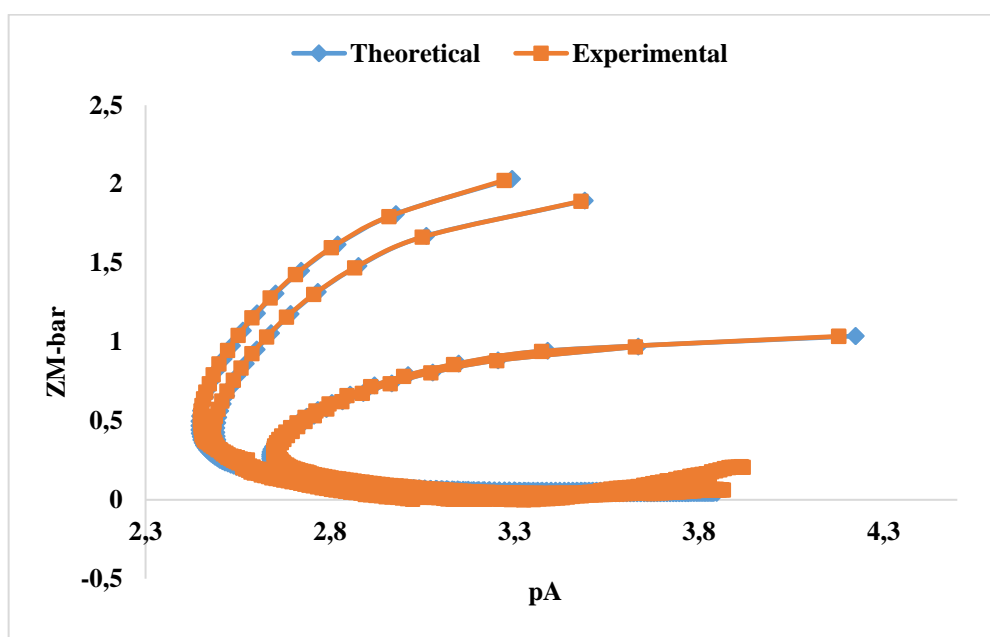


Figure 3.28: Z_M-bar as a function of pA for the Cu(II) PAS complex.

Figure 3.29 shows the deprotonation function Q-bar for the Cu(II) PAS complex. Between pH 2.44 and 3.27, the Q-bar value is zero indicating that no proton has been displaced due to complexation. At pH values above 3.39, the deprotonation function Q-bar rises to intersect the protonation curve, n-bar, at a pH of 4.5, reaching a maximum of 0.14. Above pH 4.8, the Q_M-bar curve rises indicating the formation of hydroxo species.

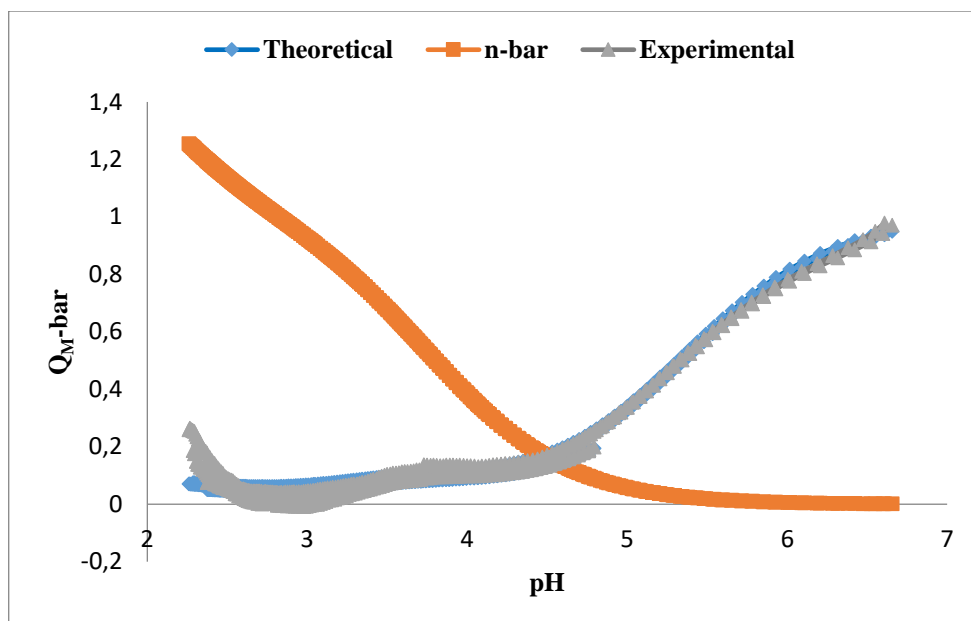


Figure 3.29: Q_M -bar as a function of pH for the Cu(II) PAS complex.

Table 3.12 shows the species and the stability constant obtained for the complexation of Cu(II) with PAS. The theoretical and experimental formation and deprotonation functions were in good agreement; the titration results were also reproducible at various metal: ligand ratios. The reported standard deviations of $\log \beta_{pqr}$ values obtained from potentiometry are reasonably low.

Table 3.12: Stability constants ($\log \beta_{pqr}$) for Cu(II) PAS complex $\beta_{pqr} = [M_p L_q H_r] / [M]^p [L]^q [H]^r$, $I = 0.15$ mol dm⁻³ (NaCl), $T = 25$ °C. S. dev. denotes standard deviation in $\log \beta_{pqr}$; R_f^H is the Hamilton R-factor and R_{lim}^H its limit, n_T is the number of titrations, (n_p) is the number of titration points.

Complexes	p	q	r	$\log \beta_{pqr}$	S. dev.	R_f^H	R_{lim}^H	$n_T(n_p)$
CuPASH	1	1	1	5.59	0.02			
CuPAS	1	1	0	2.21	0.01	0.0 04	0.001	4(641)
CuPASH-1	1	1	-1	-2.74	0.007			

The species distribution curve for the complex of PAS and Cu(II) is shown in Figure 3.30. At pH 2.1, there is 60% of the free metal ion species. Around pH 2.09-3.15, the CuPASH species began to form, rising to a maximum of 40%. The proportion of this species began to fall at pH 3.3 when the formation of CuPAS commenced with a maximum of 51% in the solution;

CuPASH₁ was formed at the expense of the CuPAS species. The highest amount of CuPASH₁ species present in the solution was 19%.

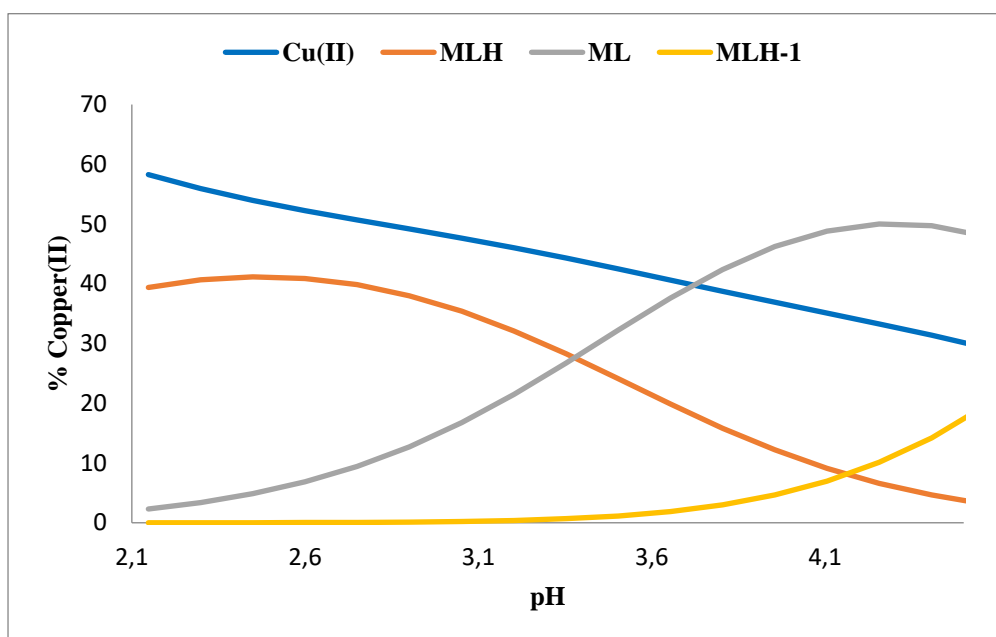


Figure 3.30: The distribution curve for the Cu(II) PAS complex (metal to ligand ratio 1:1).

3.5.3.3 Discussion

Table 3.13 shows the equilibrium constant for the deprotonation reaction of CuPASH ($\log \beta_{MLH} - \log \beta_{ML} = (5.59 - 2.21)$), i.e. 3.38. This pK_a is closer to that of the amino group in aniline (4.72) than the pK_a of phenol group in methyl salicylate (9.87)²⁷ suggesting that the amino nitrogen is protonated in the formation of MLH. The proposed structure for CuPASH is depicted in Figure 3.31.

Table 3.13: Equilibrium constants of the reaction of Cu(II) with PAS

The reaction progress	Cu(II)
$MLH \rightleftharpoons ML + H^+$	3.38
$ML \rightleftharpoons MLH_{-1} + H^+$	4.96

The complex is formed by the coordination of the metal to the carboxylic and phenolic groups, the amino nitrogen group being protonated. ML is formed by the deprotonation of the amino group in MLH, ($\text{MLH} \rightleftharpoons \text{ML} + \text{H}^+$). The MLH_{-1} species is formed by the deprotonation of ML ($\text{ML} \rightleftharpoons \text{MLH}_{-1} + \text{H}^+$) leading to a complex with $\text{p}K_a$ of 4.96. The deprotonation occurs at a much lower pH than the deprotonation of the phenolic OH group of the free ligand, suggesting a metal ion induced proton loss.⁴⁶ The structures of the complexes are shown below for MLH, ML and MLH_{-1} respectively. The complexes all contain six-membered rings, indicating that quite stable complexes are formed.

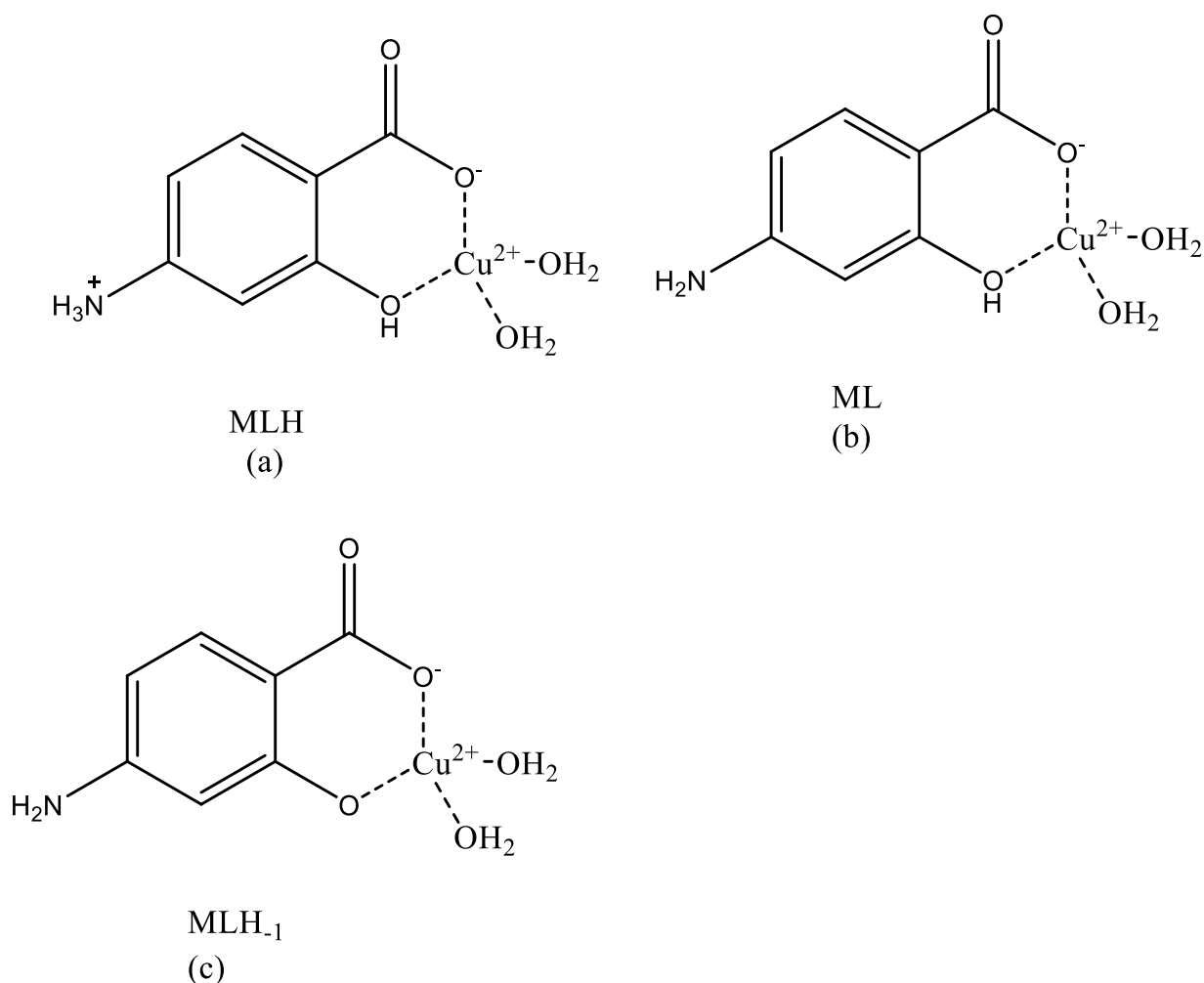


Figure 3.31: Possible structures for MLH, ML and MLH_{-1} in the Cu(II) PAS system.

Titration were carried out with Ni(II) and Zn(II) metals, but no complexation could be detected under the conditions of our experiment.

References:

1. A. E. Martell and R. D. Hancock, in J. P. Fackler Jr (Ed.), *Metal Complexes in Aqueous Solutions*, Modern Inorganic Chemistry Series, Plenum Press, New York, 1996.
2. M. Rhazia, J. Desbrierech, A. Tolaimatea, M. Rinaudob, P. Vottero, A. Alagui and M. Elmeray, *Eur. Polym. J.*, 2002, **38**, 1523-1530.
3. N. Takuhiro, *Biophys. Chem.*, 1998, **71**,173-184.
4. N. N. Golovnev, O. S. Romanova and N. V. Busygina, *J. Anal. Chem.*, 1999, **55**, 508-511.
5. R. J. Motekaitis, A. E. Martel, J. M. Lehn and E. I. Watanabe, *J. Inorg. Chem.*, 1982, **21**, 4253–4257.
6. P. M. May and K. Murray, *Talanta*, 1988, **35**, 927-932.
7. P. M. May, K. Murray and D. R. Williams, *Talanta*, 1988, **35**, 825-830.
8. F. Marsicano, C. Monberg, B. S. Martincigh, K. Murray, P. M. May and D. R. Williams, *J. Coord. Chem.*, 1988, **16**, 321-339.
9. G. E. Jackson and M. J. Kelly, *J. Chem. Soc. Dalton Trans.*, 1990,1889-1893.
10. G. Kim, S. Tomasz, A. Levenstam and I. Ari, *Anal. Chim. Acta*, 2015, **888**, 36-43.
11. K. Murray and C. T. Newman, *Equilibrium Simulations for Titration analysis; Manual Version 3.0.1989*. Processing and Chemical Manufacturing Technology Division Council for Scientific and Industrial Research, Pretoria, South Africa.
12. H. Irving and H. S. Rossotti, *J. Chem. Soc.*, 1955, 3397-3405.
13. S. Odisitse and G. E. Jackson, *Bioinorg. Chem. Appl.*, 2014, <http://dx.doi.org/10.1155/2014/863612>.
14. H. Irving and J. P. Williams, *J. Chem. Soc.*, 1953, **75**, 3192-3210.

15. E. T. Nomkoko, G. E. Jackson, B. S. Nakani and S. A. Bourne, *J. Chem. Soc. Dalton Trans.*, 2004, **12**, 1789–1796.
16. V. S. Bagotskii and V. Sergeevich. *The Fundamentals of Electrochemistry* 2nd Ed. Hoboken, N. J, Wiley- Interscience, 2006.
17. A. O. Santini, H. R. Pezza, J. E. De Oliveira and L. Pezza, *J. Braz. Chem. Soc.*, 2008, **19**, 162-168.
18. S. Odisitse, G. E. Jackson, T. Govender, E. G. Kruger and A. Singh, *Dalton Trans.*, 2007, 1140-1149.
19. G. E. Jackson and B. S. Nakani, *J. Chem. Soc. Dalton Trans.*, 1996, 1373–1377.
20. A. I. Vogel, *Vogel's Textbook of Quantitative Inorganic Analysis*, 4th Ed. Longman Group, London, 1978.
21. H. M. Irving, M. G. Miles and L. D. Petit, *Anal. Chim. Acta*, 1967, **38**, 475-488.
22. G. Gran, *Analyst*, 1952, **77**, 661-671.
23. G. H. Jeffery, J. Bassett, J. Mendham and R. C. Deney, *Vogel's Textbook of Quantitative Chemical Analysis*, 5th Edition. Longman, London, 1989.
24. A. E. Martel and R. J. Motekaitis, *Coord. Chem. Rev.*, 1990, **100**, 323-361.
25. G. G. Guilbault, D. N. Kramer and P. Goldberg, *J. Phys. Chem.*, 1963, **67**, 1747–1749.
26. J. C. Rossotti and H. Rossotti, *J. Chem. Educ.*, 1965, **42**, 375-378.
27. L. D. Pettit and H. K. J Powell, *Stability Constant Database*. Academic Software, Timble, Otley, York, LS21 2PW, UK. 1993.
28. SPARC calculator; <http://ibml2.chem.uga.edu/sparc>. (accessed 3 April 2016)
29. F. A. Nada, G. Ahmed and A. A. Rasha. *Int. J. Electrochem. Sci.*, 2011, **6**, 5097-5113.
30. B. K. Magare, M. N. Farooqui, R. S. Shelke and M. B. Ubale, *Orient. J. Chem.*, 2009, **25**, 387-390.
31. L. Robert, *J. Org. Chem.*, 1960, **25**, 290-290.

32. L. Kathryn and K. J. Franz, *Chem. Rev.*, 2009, **109**, 4921-4960.
33. E. Kimura, T. Shiota, T. Koike, M. Shiro and M. Kodama, *J. Am. Chem. Soc.*, 1990, **112**, 5808-5811.
34. C. F. Baes and R. E. Mesmer, *The hydrolysis of cations*, Wiley-Interscience Publication, New York, 1976.
35. G. R. Nageswara and M. M. Annapurna, *J. Pharm. Educ. Res.*, 2010, **1**, 44-50
36. S. Youngme, C. Pakawatchai and H. K. Fun, *Acta Crystallogr.*, 1998, **C54**, 451-453.
37. S. Youngme, C. Pakawatchai, H. K. Fun and K. Chinnakali, *Acta Crystallogr.*, 1998, **C54**, 1586-1588.
38. A. Ciobanu, F. Zalaru, C. Zalaru, F. Dumitrascu and C. Draghici, *Acta Chim. Slov.*, 2003, **50**, 441-450.
39. S. M. Malathy, M. Kuppayee, M. N. Ponnuswany, J. Manonmani, M. Kandasamy, K. Sivakumar and H. K. Fun, *Cryst. Res. Technol.*, 2006, **41**, 517.
40. A. Nielsen, N. A. Bond and C. J. Mckenzie, *Acta Crystallogr.*, 2005, **E61**, m478-m480.
41. Y. Yousif and F. Al-Imarah, *J. Inorg. Nucl. Chem.*, 1980, **42**, 779-791.
42. E. Mentasti, F. Secco and M. Venturini, *Inorg. Chem.*, 1980, **19**, 3528-3534.
43. V. Gupta, J. Shtapak and D. Sharma, *J. Inorg Nucl. Chem.*, 1981, **43**, 3019-3027.
44. R. Corigli, F. Secco and M. Venturini, *Inorg. Chem.*, 1982, **21**, 2992-2998.
45. C. K. Gross and P. G. Seybold, *Int. J. Quantum Chem.*, 2000, **80**, 1107-1115.
46. T. S. Planka, B. Gyurcsik, N. V. Nagy, A. Rockenbauer, R. Sipos, S. Sima and M. Melnik, *J. Inorg. Biochem.*, 2008, **102**, 101-109.

Chapter 4

Spectroscopic and Bioavailability Studies

4.1 UV-Visible spectroscopy

4.1.1 Introduction

Transition metals are elements whose atoms have a partially filled *d*-subshell or which can give rise to cations with an incomplete *d*-subshell. Colour in transition metal compounds is due to charge transfer transition or *d-d* transition. The *d*-orbitals of the free transition metal are degenerate; the *d*-orbitals interact with the ligand electron cloud, which results in the *d*-orbitals becoming non-degenerate. When the *d*-level is not filled, it is possible to promote an electron to a higher energy *d*-orbital by absorption of a photon of light. The visible region of the spectrum often possesses the appropriate energy for such transition.

4.1.2 Theory

Ultraviolet-visible spectrophotometry (UV-Vis) is an absorption spectroscopy in which a molecule absorbs light in the ultraviolet/visible region of the electromagnetic spectrum (200-400 nm). Absorption of the ultraviolet radiation results in the excitation of the electrons from the ground state to a higher energy state. The energy of the ultraviolet radiation that is absorbed is equal to the energy difference between the ground state and the higher energy state. This technique is usually applied to inorganic ions, molecules and complexes in solution.¹ It has features for sample identification and is useful for quantitative measurement. It is a frequently used technique because of its simplicity, versatility, speed, accuracy and cost-effectiveness.² A spectrum is obtained when the absorbance is plotted against the wavelength. The principle is based on the Beer-Lambert law which states that, for a given ideal solution, there is a linear relationship between concentration and absorbance provided that the path length is kept constant.

This can be expressed in the following form;

$$A = \log_{10} \frac{I_0}{I} = \epsilon C b \quad (4.1)$$

where A = Absorbance

I_0 = Intensity of light incident upon sample cell

I = Intensity of the transmitted light

C = Molar concentration of solute

b = Length of the sample cell (cm)

ϵ = molar absorptivity

If the analyte solution is a combination of different species, the total absorbance, at a specific wavelength (A^λ), can be expressed as

$$A^\lambda = b (\epsilon_1^\lambda C_1 + \epsilon_2^\lambda C_2 + \epsilon_3^\lambda C_3 + \dots + \epsilon_n^\lambda C_n) \quad (4.2)$$

where the superscript λ is the wavelength and subscripts 1, 2, 3...n denote absorbing species.

Equation, 4.2 can be simplified, as follows:

$$A^\lambda = b \sum \epsilon_i^\lambda C_i \quad (4.3)$$

If A, b and C are known, then ϵ can be calculated. The wavelength of absorption differs from species to species; the maximum wavelength of absorption can be related to the structure of the species. λ_{\max} values can, therefore, be used to predict structures of complexes.³ One important method, Billo's method, of correlating λ_{\max} and ligand field strength is quite well understood and thus enables the ligating atoms to be determined.⁴

The calculated λ_{\max} is expressed as

$$\lambda_{\max} = \frac{10^3}{n_i \nu_i} \quad (4.4)$$

where n_i is the number of equatorial donor groups, and ν_i is the ligand field of the complex.

Many authors⁵⁻⁷ have used UV-Visible spectroscopy to predict the structures of Cu(II) complexes.

4.1.3 Experimental

Solutions of Cu(II)/EMB, Ni(II)/EMB Cu(II)/ISO, Cu(II)/PAS were prepared in deionised water respectively. The pH values of the solutions were adjusted with NaOH/HCl. The pH was determined using a CRISONmicro pH meter equipped with a Ω Metrohm glass electrode. The precise amount of NaOH/HCl added was noted. The concentrations of the absorbing species were calculated at every pH using the equilibrium constants determined in Chapter 3. The absorbances of these solutions were measured with a Hewlett Packard 8452A Diode Array spectrophotometer from 200 nm to 800 nm. A blank was used to correct the absorbance. The precise absorbance and the extinction coefficients of individual species could not be measured due to the presence of mixed species in solution. However, it was possible to deconvolute the spectra to yield spectra for the individual species. This was done using the program UV-SPEC.⁸ The deconvolution was performed one wavelength at a time using the speciation model. The smoothness of the spectra lends confidence to the potentiometric models. The value of λ_{\max} calculated for the visible spectrometric band was obtained from the deconvoluted spectra.

4.1.4 Results and Discussion

4.1.4.1 Cu(II) EMB-System

Figure 4.1 displays the UV-Visible electronic spectra for Cu(II) EMB at different pH values. At low pH, there is little complex formation and the spectrum is that of $[\text{Cu}(\text{OH}_2)_6]^{2+}$ with maximum absorption > 800 nm. The peak changes shape, increases in intensity and shifts to higher wavelength with a gradual increase in pH. Also, there is a blue shift from 688 nm in the pH range 4.26 to 7.45 and finally shifts further as the pH increases up to 10.61. From the potentiometric results, the species formed in this region are ML_2 , ML_2H_{-1} and ML_2H_{-2} . There

is the probability of hydrolysis at high pH. Based on the ligand field theory, the gradual shift from 688 nm to 646 nm with increasing pH indicates that the donor atoms in the high pH region exert higher ligand field strength. There was no precipitate throughout the entire pH range of study.⁹

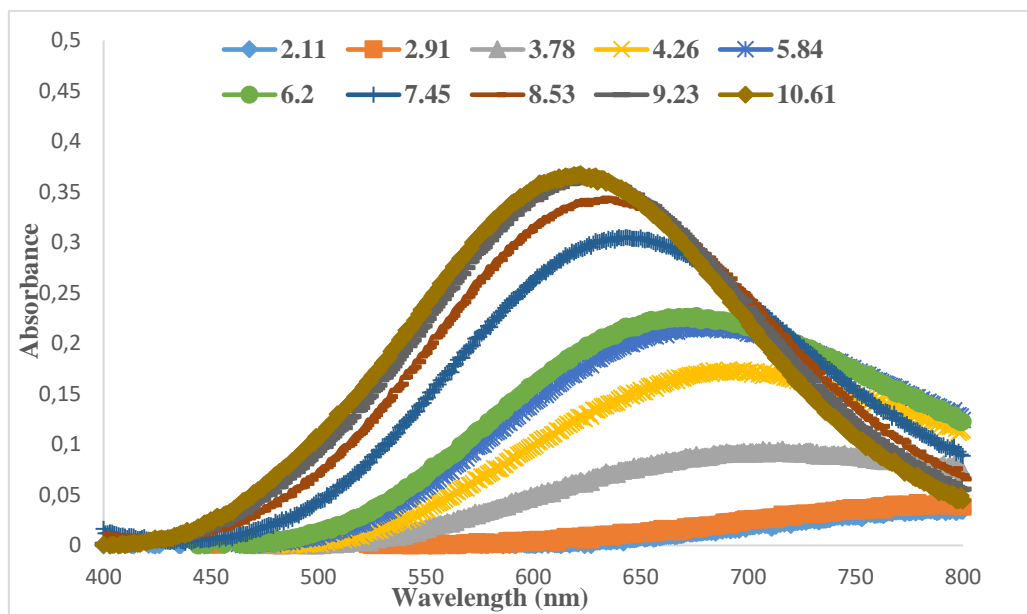


Figure 4.1: UV-Visible electronic absorption spectra for Cu(II) EMB with [M (0.02M – L (0.01M)] at different pH values.

UV-spectra of different species for the Cu-EMB system are revealed in Figure 4.2. The comparative evaluation of the potentiometric titration and the UV/Vis data indicate the subsequent formation of various complexes as a function of pH and metal to ligand ratio.

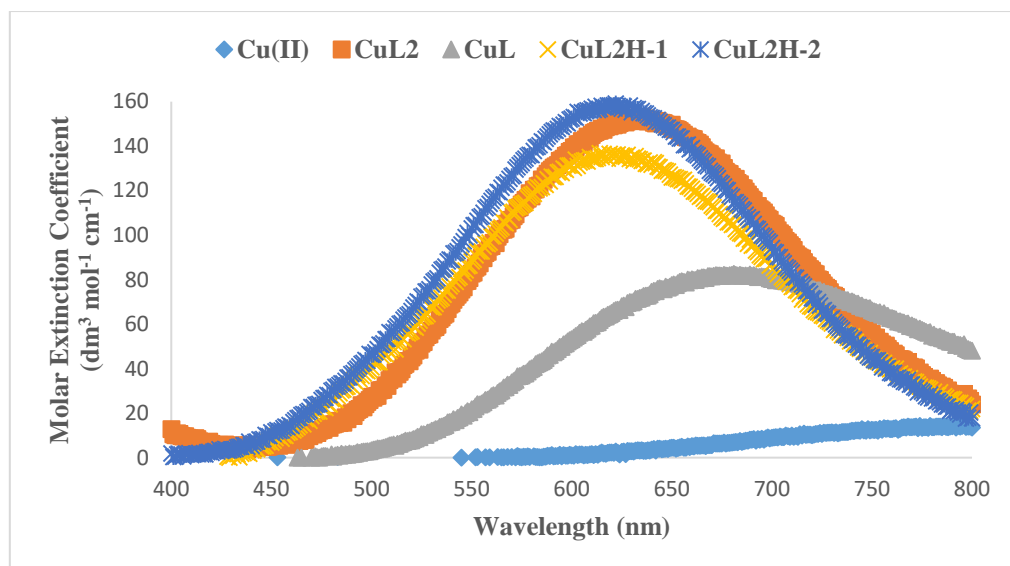


Figure 4.2: UV-spectra of different species for the Cu EMB₂ system.

The smooth graph indicates that the model is appropriate. In an equimolar solution of the complexes, CuL was the major species; this has also been predicted for a pH-metric experiment taking a 1:1 ratio of Cu(II): EMB.¹⁰ The spectra confirm this in Figure 4.2. The ML complex has a single peak in the visible region due to the $E_g \rightarrow T_{2g}$ transition. The very close λ_{\max} values (Table 4.1) of 684 nm ($\epsilon = 82.18 \text{ dm}^3 \text{ mol}^{-1} \text{ cm}^{-1}$) for Cu(EMB) and 680 nm for $[\text{Cu(II)(en)}]^{2+}$,¹¹ suggest that these species have similar coordination mode. It has been reported that mono- and bis(ethylenediamine)copper(II) complexes in aqueous solution have distorted octahedral structure with two elongated axial bonds.¹¹

Using Billo's method, and assuming coordination by 2N and 2O atoms (H_2O or OH), a value of 663 nm is calculated, i.e. the OH and H_2O have the same ligand field parameter. Hence, from the electronic spectral results, it is not possible to decide if the ethanolic groups of EMB are coordinated or not.

In the case of excess ligand, bis-complexes are present between pH 6-11. There is a large spectral shift in going from CuL to CuL₂, indicating that there is a difference in the coordination mode. The λ_{\max}^{d-d} value for CuL₂ is 630 nm, which is higher than λ_{\max} of 545 nm for

$[\text{Cu(II)(en)}_2(\text{OH}_2)_2]^{2+}$.¹² Since the two ligands, en and EMB, differ only in the two ethanolic groups, this suggests that the OH is somehow involved in the coordination, perhaps replacing the two coordinated water molecules found in $[\text{Cu(II)(en)}_2(\text{OH}_2)_2]^{2+}$. The difference in shift observed from ML_2 to ML_2H_{-1} and ML_2H_{-2} was not so large, suggesting that the species $\text{CuL}_2\text{H}_{-1}$ and $\text{CuL}_2\text{H}_{-2}$ possess the same coordination mode. These predicted results indicate the same structures as proposed by the potentiometric result and are in good agreement with the observed λ_{max} .

Table 4.1: UV-Vis spectra ϵ_{max} ($\text{dm}^3 \text{mol}^{-1} \text{cm}^{-1}$) and λ_{max} (nm) exp. and calc. values with possible donor groups for Cu(II) EMB complexes.

Species	Experimental λ_{max} (nm)	ϵ_{max} ($\text{dm}^3 \text{mol}^{-1} \text{cm}^{-1}$)	Calculated λ_{max} (nm)	Possible donor atoms
CuL	684	82.18	663	2N, 2O
CuL₂	630	155.3	552	4N
CuL₂H₋₁	624	134.34	552	4N
CuL₂H₋₂	622	159.10	552	4N

4.1.4.2 Ni(II) EMB-System

The absorption spectra as a function of pH for Ni(II) EMB are given in Figure 4.3. At low pH values, the solution is made up of hydrated $[\text{Ni(OH}_2)_6]^{2+}$. As the base concentration is increased, the intensity of the absorption band at 480 nm increases (curves from pH 9.3 to 10.61).

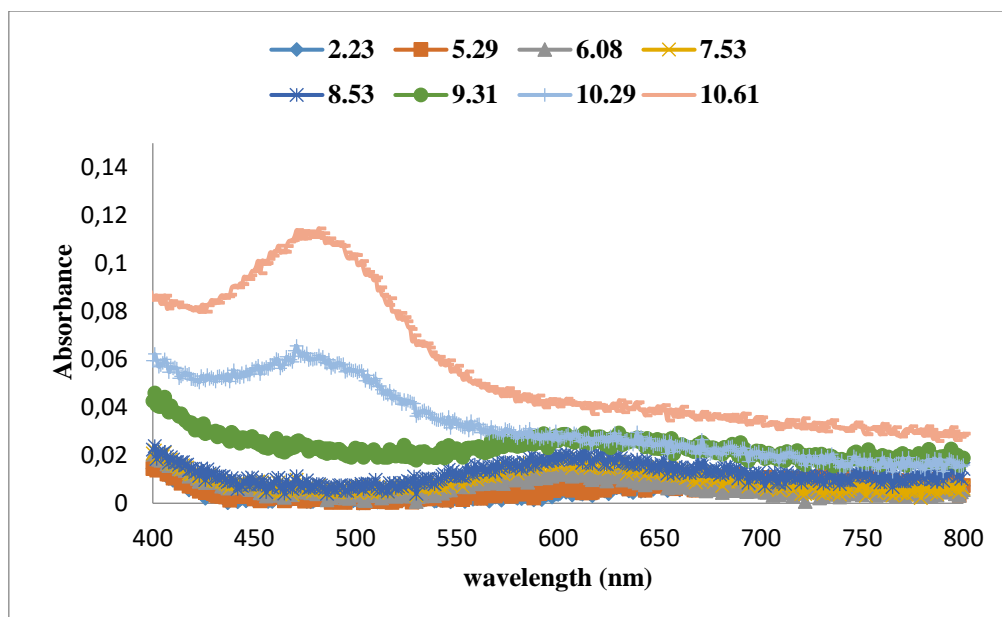


Figure 4.3: UV-Visible electronic spectra for Ni(II) EMB at different pH values.

The NiLH₋₁ and NiLH₋₂ species presented similar spectroscopic parameters, supporting the same coordination in all the Ni(II) ions. At pH 5.29 the solution colour starts to change. Studies have shown that for nickel (II) complexes there is often a change of UV-Visible spectra representing a regular shift of the complex from octahedral to square-planar structures when two or more amino nitrogens coordinate.^{13,14}

Ni(II) complexes of diamine ligands are known to produce, in solution, an equilibrium mixture of complexes.¹⁵ In this study, a peak was observed at 610 nm, prominent up to pH 9.3, which shifts to 477 nm at pH 10.29. With a further increase in pH, the absorbance remains constant but the extinction coefficient increases, as shown in Figure 4.4. Factors such as [OH⁻], added electrolyte and temperature could affect the geometry.¹⁶

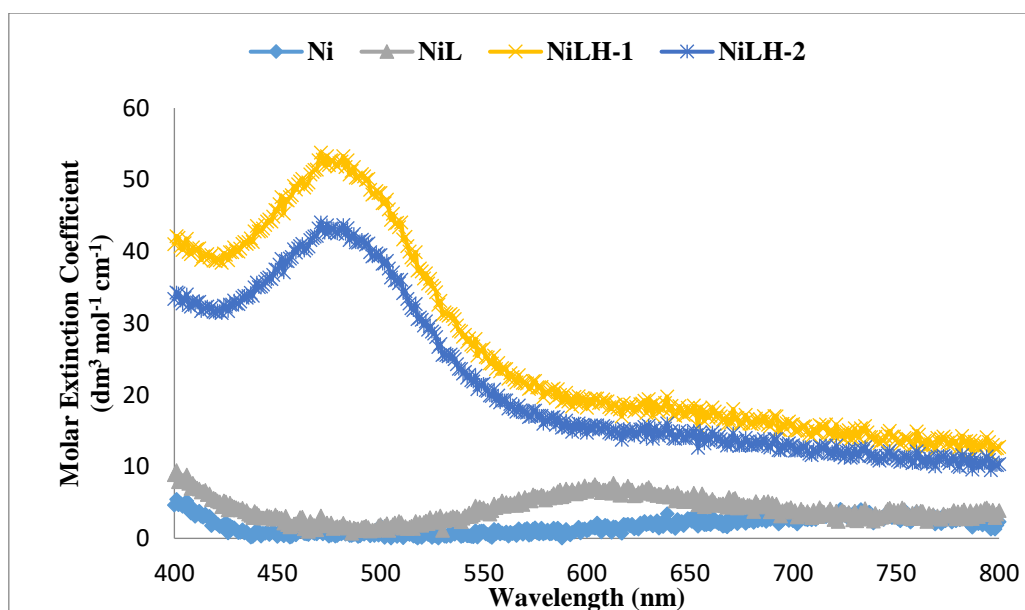


Figure 4.4: UV-spectra of different species for the Ni(II) EMB system.

Nickel(II) amine complexes exhibit characteristic bands for the transition ${}^3A_{2g} \rightarrow {}^3T_{1g}(F)$ [588-572 nm] and ${}^3A_{2g} \rightarrow {}^3T_{1g}(P)$ [377-353 nm].^{17,18} Table 4.2 shows the wavelength and molar extinction coefficient values corresponding to maximum absorption of the Ni(II) species formed in solution with possible donor groups for this ligand.

Table 4.2: UV-vis spectra ϵ_{\max} ($\text{dm}^3 \text{mol}^{-1} \text{cm}^{-1}$) and λ_{\max} (nm) exp. and calc. values with possible donor groups for Ni(II) EMB complexes.

Species	Experimental	ϵ_{\max} ($\text{dm}^3 \text{mol}^{-1} \text{cm}^{-1}$)	Possible donor atoms
	λ_{\max} (nm)		
NiL	604	7	2N, 2O
NiLH ₁	482	53	2N, 2O
NiLH ₂	482	44	2N, 2O

The experimental value ($\lambda_{\max} = 604$ nm) for NiL is close to the λ_{\max} of 617 nm reported for Ni-N,N'-(S,S)-bis[1-carboxy-2-(imidazole-4-yl)ethyl]ethylenediamine (BCIEE) system.¹⁹ These values strongly support the transition from ${}^3A_{2g} \rightarrow {}^3T_{1g}(F)$ for the NiL with an octahedral

geometry. The widely reported electronic spectral studies of nickel(II) amine complexes indicate that they are octahedral and paramagnetic.²⁰ As the base concentration is increased, at pH 8.53, the solution starts to change colour from light green to yellow. This corresponds to a new band at 482 nm (Figure 4.4) which increases in intensity as the pH is raised. This band is assigned to a $^1A_{1g} \rightarrow ^1A_{2g}$ transition, which is expected for absorption by square-planar species.^{21,22} In the pH range 8.53-10.61, NiLH₁ and NiLH₂ predominate. The molar extinction coefficient increased from 7 dm³ mol⁻¹ cm⁻¹ for NiL to ~ 50 dm³ mol⁻¹ cm⁻¹ for MLH₁ and MLH₂. Diamagnetic and square-planar geometry has been reported for Ni(II) complexes coordinating to amino nitrogen atoms.²³⁻²⁵ This result is in agreement with the potentiometric results.

4.1.5.1 Cu(II) ISO-System

The UV-visible electronic absorption detected for the Cu-ISO spectrum is shown in Figure 4.5 below. At low pH 2.33-3.42, the spectrum is the same as that of $[(Cu(OH_2)_6]^{2+}$. As the base concentration increased, the absorption bands shifted towards shorter wavelength with an increase in intensity for pH values of 3.7 and 4.07.

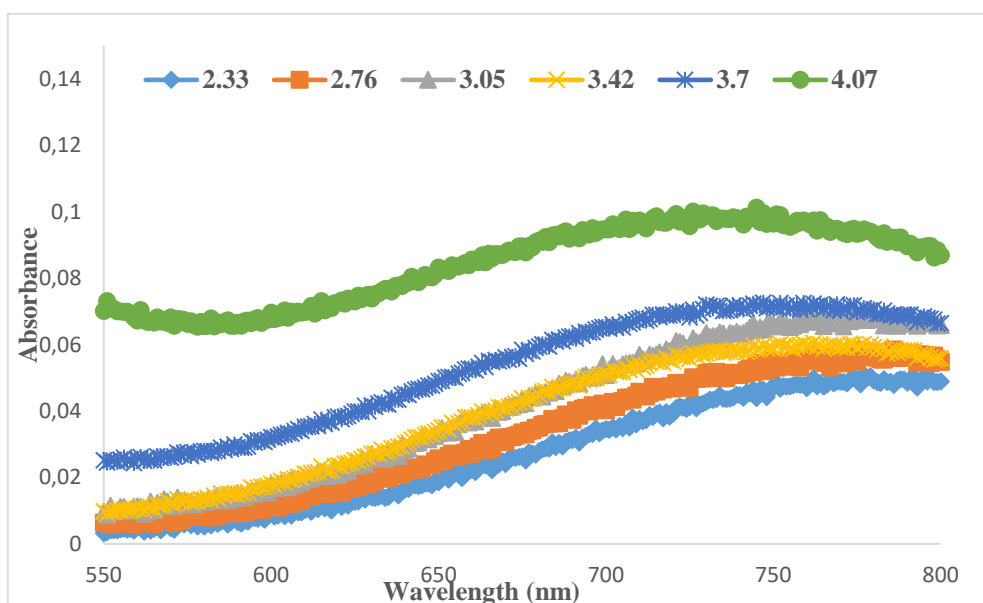


Figure 4.5: UV-Visible electronic absorption spectra for Cu(II) ISO with [M (0.015 M) – L (0.03 M)] at different pH values.

The calculated absorption spectra for the individual species are shown in Figure 4.6. At pH 3.5, the formation of MLH species has already begun; this is in support of the speciation curves in Figure 3.5.

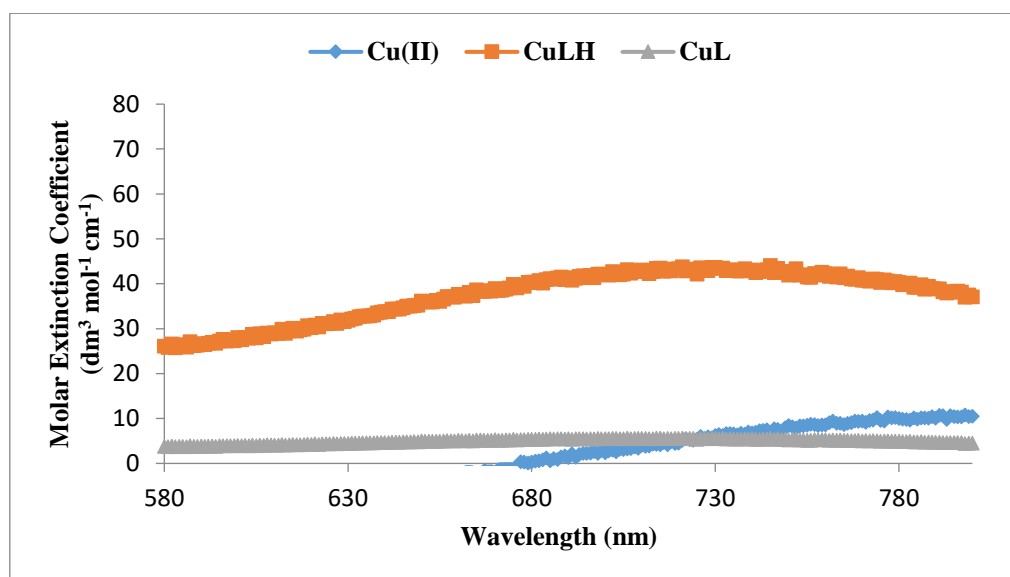


Figure 4.6: Calculated spectra of Cu(II) ISO individual species.

The values of λ_{\max} and ϵ_{\max} for CuLH are estimated as 746 nm and $42.53 \text{ dm}^3 \text{ mol}^{-1} \text{ cm}^{-1}$. The λ_{\max} for the CuLH is similar to λ_{\max} of $[\text{Cu}(\text{NH}_3)(\text{OH}_2)]^{2+}$ (745 nm). Similar values have also been reported for L-3,4-dihydroxyphenylalanine and δ -DL-hydroxylysine.^{26,27} This suggests that the hydrazide amino nitrogen atoms of ISO are coordinated to the copper, which means that the pyridine nitrogen is protonated. This is in agreement with the potentiometric results. Unfortunately, the low concentration of ML does not make it possible to calculate the spectroscopic data of this species.

4.1.6.1 Cu(II) PAS-System

The UV-Visible electronic absorption spectra for a copper complex of p-aminosalicylic acid are shown in Figure 4.7. Note that only a limited pH range was studied, as at higher pH

precipitate was observed. According to the potentiometric results MLH, ML and MLH₋₁ are formed within this pH range.

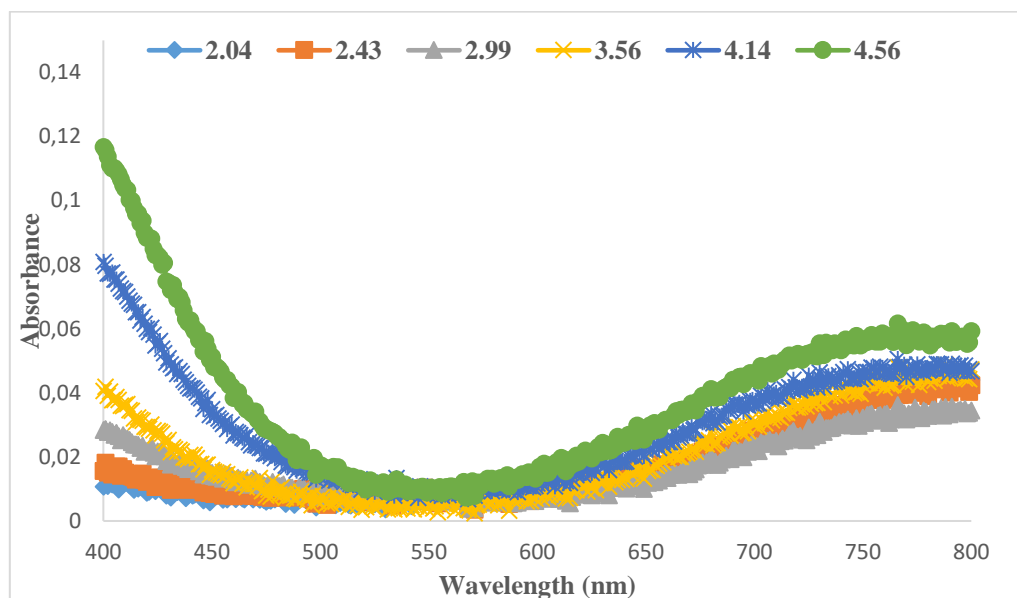


Figure 4.7: UV-Visible electronic absorption spectra for Cu(II) PAS with [M (0.01 M) – L (0.02 M)] at different pH values.

The deconvoluted spectra for the Cu(II) PAS individual species are revealed in Figure 4.8 below. At low pH, there is little complex formation and the spectrum is that of $[\text{Cu}(\text{OH}_2)_6]^{2+}$ with maximum absorption > 800 nm. The experimental λ_{max} and molar extinction coefficient for ML and MLH₋₁ are valued as 743 nm, $28.33 \text{ dm}^3 \text{ mol}^{-1} \text{ cm}^{-1}$ and 736 nm, $8.35 \text{ dm}^3 \text{ mol}^{-1} \text{ cm}^{-1}$ respectively. There is a decrease in the λ_{max} of MLH₋₁ when compared to ML. This may be attributed to deprotonation of the phenolic OH group of the free ligand. For this to occur at such a low pH, the metal ion must be involved in a metal ion induced proton loss,²⁸ resulting in the spectral change. These results support the structure proposed from the potentiometric results in Figure 3.31.

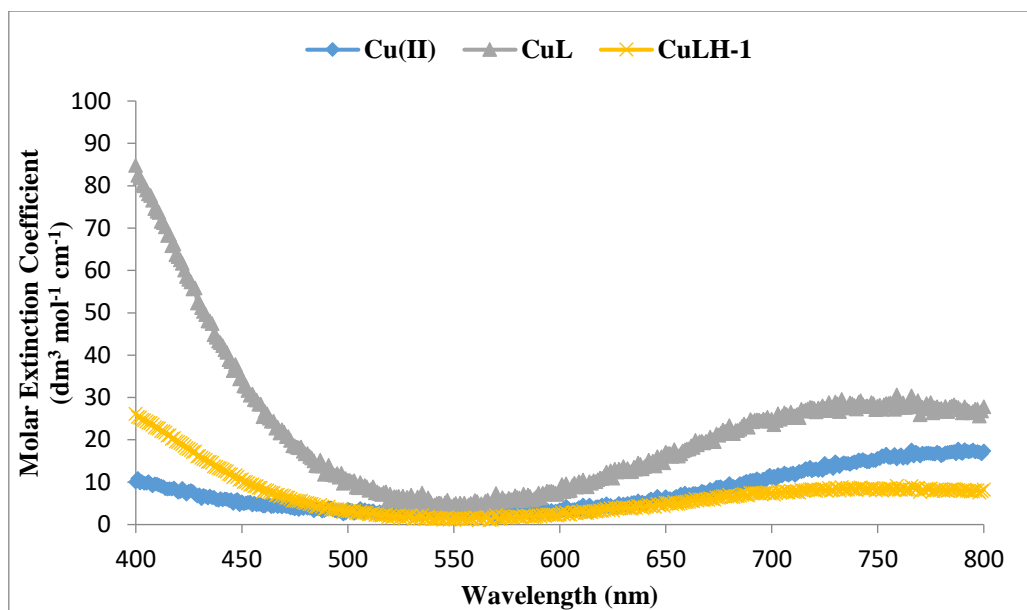


Figure 4.8: Deconvoluted spectra of Cu(II) PAS individual species.

4.2 Dermal Absorption Study

4.2.1 Introduction

One of the aims of this work was to develop new anti-TB drugs by re-engineering existing drugs to improve lipophilicity/hydrophilicity of the ligand and hence bioavailability. This was done by synthesising metal complexes of the drugs. The effect of the metal ion on bioavailability was assessed by measuring the effect of the metal on the rate of diffusion of the ligand through an artificial membrane as a model for skin and comparing this rate with the partition coefficient determined in 1-octanol.

4.2.2. Octanol/Water Partition Coefficients

Partitioning is the movement of molecules from one phase to another. The partition or distribution coefficient (D) is the ratio of the concentration of a compound in two phases of a mixture of two immiscible solvents at equilibrium. These coefficients are a measure of differential solubility of the compound between two solvents. One of the solvents is water and the other one is hydrophobic, such as octanol. It is useful in estimating the distribution of drugs within the body. It indicates the lipophilic-hydrophilic character of the drug molecule. The structural activity relationship of a series of drugs can be studied and the change in lipophilicity can measure the extent of complexation of a drug.

Lipophilicity of an organic compound is frequently described with reference to the partition coefficient.²⁹⁻³¹ Since partition coefficients can range over many orders of magnitude, they are usually expressed in logarithmic form. $\log P$ can be defined as the ratio of the concentration of the unionised compound at equilibrium, between organic and aqueous phases.

$$\log P = \log \frac{[\text{unionized compound}]_{org}}{[\text{unionized compound}]_{aq}} \quad (4.5)$$

The octanol: water system has been widely used as a model of the lipid phases as it mimics the lipid membrane/water systems found in the body.³² Partition coefficients can be measured using the following methods: shake flask method, slow stirring method, electrochemical method. The most common method of determining partition coefficients is the shake flask method because it is accurate for both neutral and charged compounds, and knowing the chemical structure of the compound beforehand is not important.³³⁻³⁵ Factors such as temperature, pH, mutual phase saturation concentration, as well as the nature of the solvent used and solute examined affect the measured value of the partition coefficient.³⁶

Some drugs may be poorly absorbed after oral administration even though they are available predominantly in the unionised form in the gastrointestinal tract. This is attributed to the low lipid solubility of the unionised molecule. This parameter, therefore, influences the transport and absorption processes of drugs, and it is one of the most widely used properties in quantitative structure-activity relationships. In the human body, the drug must traverse several body tissues before they can impart their therapeutic effect. Transport across the skin and bio-membrane, in general, is a process of limited diffusion governed by the drug's chemical and physical properties such as lipophilicity.³⁷ The degree of ionisation is determined by the pK_a of a drug for the unionised drug. If a drug is lipid soluble, it will be well absorbed into the systemic circulation, and if poorly lipid soluble, it will be poorly absorbed. For optimum absorption, the drug should be soluble in the fluid at the absorption site and highly lipid soluble to facilitate the partitioning of the drug in the lipoidal membrane and into the systemic circulation. It is noteworthy that there should be a balance in the hydrophilicity and lipophilicity of drugs for optimum bioavailability. A positive $\log P_{\text{oct/aq}}$ (log 1 to 3), indicates the ability to diffuse across the membrane. $\log P_{\text{oct/aq}}$ greater than 5 suggests that the drug is insoluble and can aggregate in the absence of fluid.³⁸

4.2.3 Experimental

The partition coefficients of the pure drugs as well as those of their metal complexes were determined using the shake flask method. The organic phase was saturated with water.³⁹ A 0.0001 M solution of the drug was prepared in deionised water. 5 ml of the solution was dispersed into ten glass vials, and the pH of the solution was adjusted using 0.100 mol dm⁻³ NaOH.^{40,41} 5 ml of 1-octanol (99%) was added to each solution. The mixture was shaken for five minutes and allowed to stand at a constant temperature of 25 ± 0.1 °C. Two ml of each phase was pipetted into a vial, and the concentrations of the drug were determined spectrophotometrically. Triplicate readings were taken, and the average was calculated. For measurement of the partition coefficients of the metal complexes, an analogous procedure was used with solutions containing metal and drug in a 1:1 molar ratio.

4.2.4 Results and Discussion

4.2.4.1 Isoniazid

Figure 4.9 shows the speciation graph, and the partition coefficients $\log P_{\text{oct/aq}}$ of ISO as a function of pH. A notable feature about Figure 4.9 is that all the $\log P_{\text{oct/aq}}$ values were negative. Negative values of $\log P_{\text{oct/aq}}$ suggest that ISO is hydrophilic.⁴²

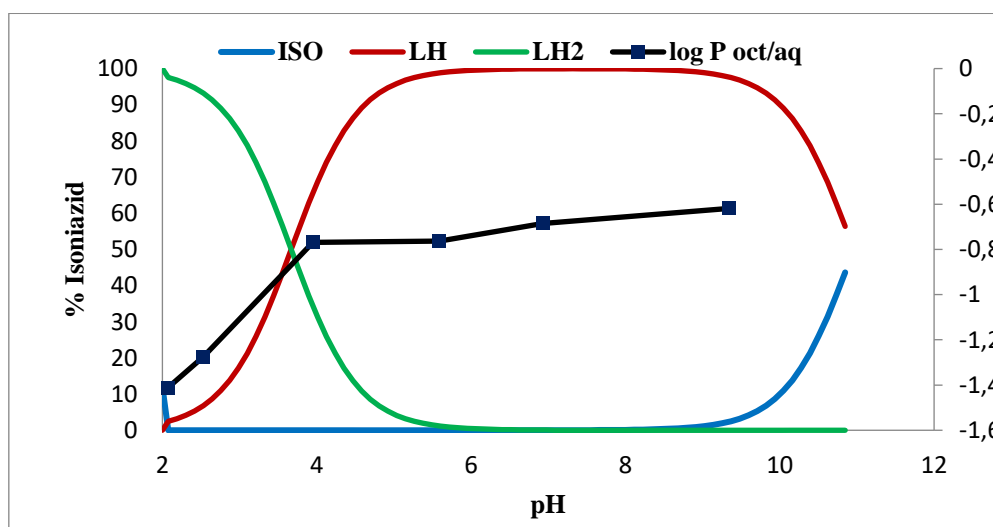


Figure 4.9: Log $P_{\text{oct/aq}}$ and speciation graph as a function of pH for ISO system.

From Figure 4.9 the speciation graph shows that from pH 3.77-9.36 the predominant species in solution is LH; the value of $\log P_{\text{oct/aq}}$ at this pH is -0.61 and can be assigned to the presence of LH species. The $\log P_{\text{oct/aq}}$ value of -0.67 has been reported in literature for isoniazid.⁴³

4.2.4.2 Cu-Isoniazid Complex

The distribution coefficient curve and the speciation graph for the Cu-ISO system plotted as a function of pH is shown in Figure 4.10. It is evident that complexes of Cu(II) ISO are more soluble in water than in 1-octanol since the $\log P_{\text{oct/aq}}$ values were negative.

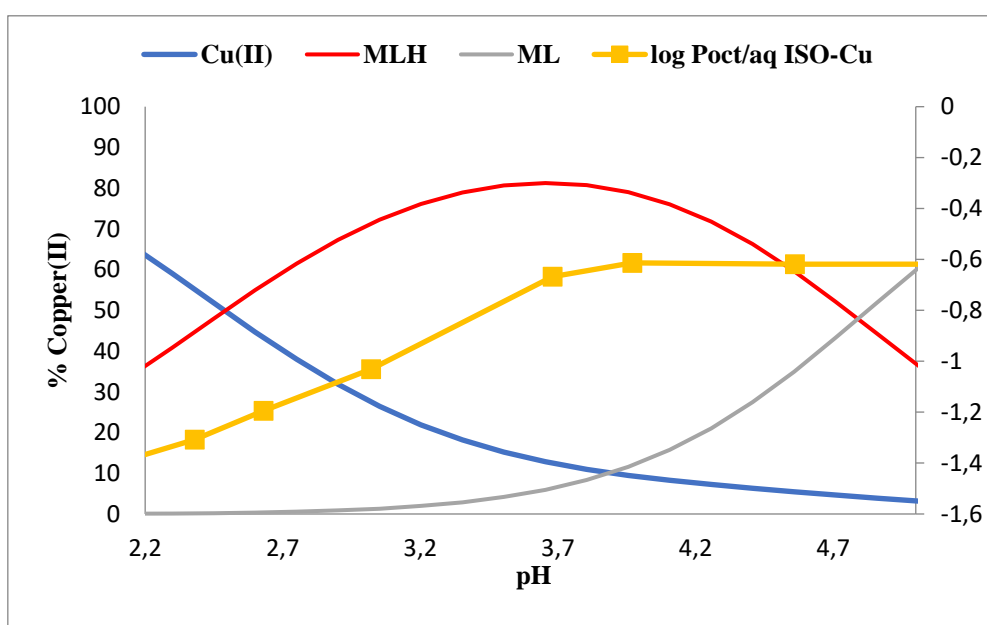


Figure 4.10: Log $P_{\text{oct/aq}}$ and speciation graph as a function of pH for 1:1 Cu-ISO system.

At pH 2.2 complexation has commenced. The distribution coefficient did not change significantly between pH 2.5 and 4.8. The speciation graph for Cu(II) ISO mirrors the formation of the two complexes, MLH and ML. $\log P_{\text{oct/aq}}$ increases from -1.40 at pH 2.2 to stabilise at -0.60 after pH 3.7 when the ISO is fully complexed. The results suggest that both species, MLH and ML, have the same partition coefficient of -0.60.

4.2.4.3 Ni-Isoniazid Complex

The negative values of $\log P_{\text{oct/aq}}$ for Ni(II) ISO show that this complex is hydrophilic (Figure 4.11). The partition coefficient is rationalised with reference to the speciation diagram.

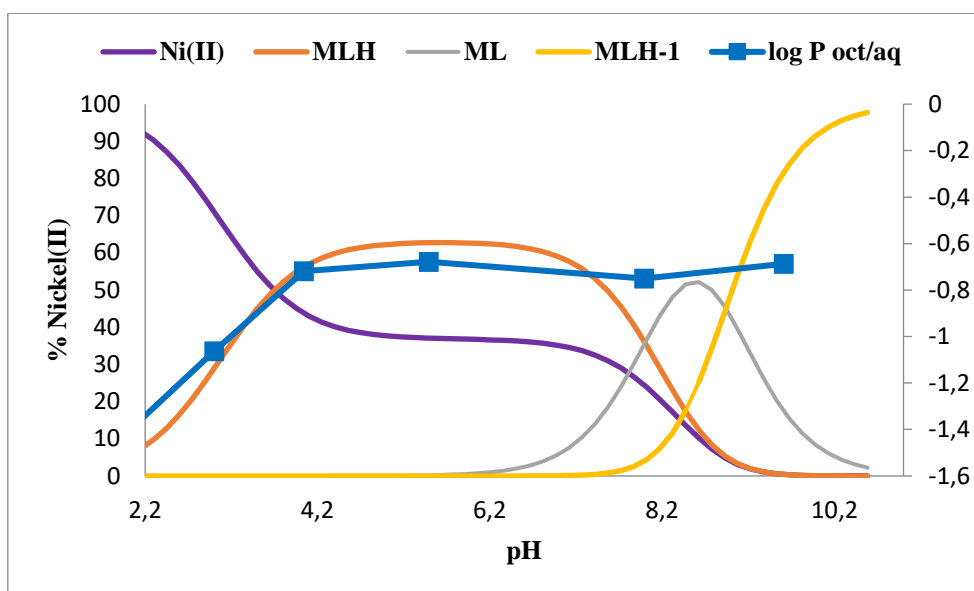


Figure 4.11: Log $P_{\text{oct/aq}}$ and speciation graph as a function of pH for 1:1 Ni(II) ISO system.

Complexation commenced at pH 2.2. In the pH range 4.4-7.99, the predominant species is MLH. Therefore the $\log P_{\text{oct/aq}}$ values of -0.75 can be attributed to the presence of MLH species. The partition coefficient did not change very significantly with pH (from 7.99-9.61). The speciation curves showed that mixed species were observed at the same pH values. Therefore the $\log P_{\text{oct/aq}}$ values were not for a single species. The $\log P_{\text{oct/aq}}$ value of -0.68 can be attributed to the ML and MLH₁ present at these pH values on the speciation graph.

4.2.4.4 Zn-Isoniazid Complex

The $\log P_{\text{oct/aq}}$ and the speciation graph as a function of pH are shown in Figure 4.12. The negative values of $\log P_{\text{oct/aq}}$ for Zn(II) ISO show that this complex is hydrophilic.

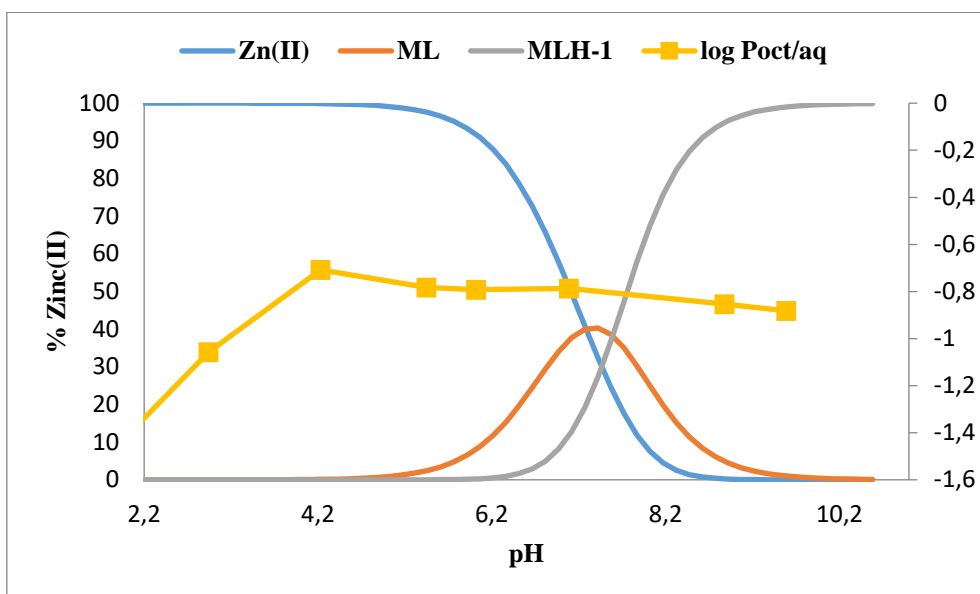


Figure 4.12: Log $P_{oct/aq}$ and speciation graph as a function of pH for the 1:1 Zn(II) ISO system.

The speciation graph shows the existence of three ligand species in the pH range 2.2 to 10.2.

Log $P_{oct/aq}$ of -0.85 can be ascribed to the ML and MLH-1 species present between pH 7.4 and 9.8.

4.2.4.5 Rifampicin and its Metal Complexes

The partition coefficients log $P_{oct/aq}$ as a function of pH for rifampicin (RFN) and its complexes are shown in Figure 4.13. The partition coefficient could not be rationalised by reference to a speciation graph because the pKa of rifampicin is lower than the pH of our present potentiometric study. The log $P_{oct/aq}$ values for the ligand and the complexes are all positive indicating that the drug is lipophilic and is likely to diffuse into lipid bilayers. The log $P_{oct/aq}$ of RFN increased from pH 2.4 to 3.36 after which it levelled off at a log P value of 2.3 throughout the entire pH range; it is close to the reported value of 2.4 reported for RFN.⁴⁴

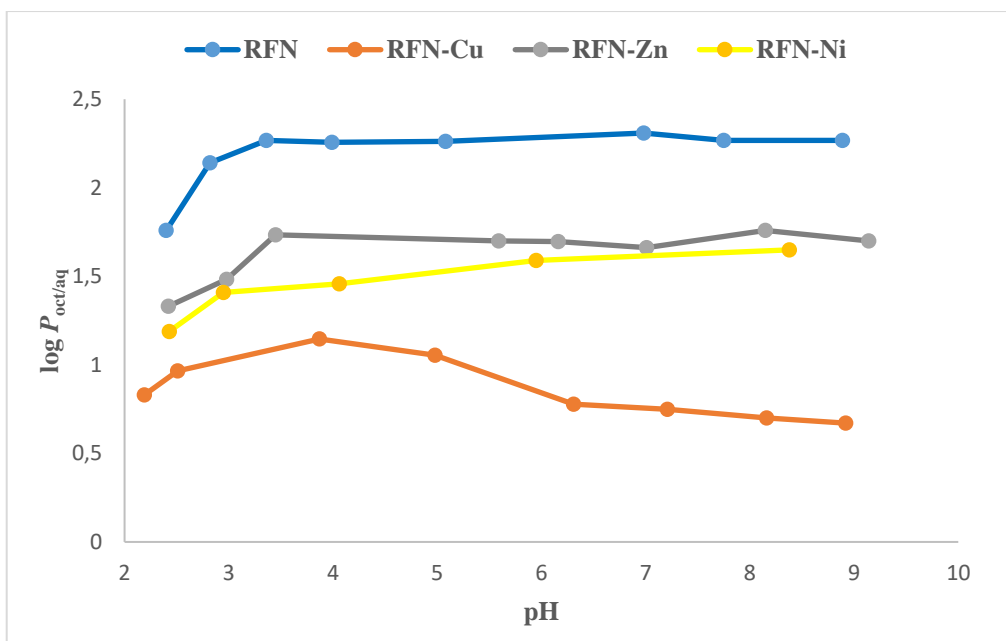


Figure 4.13: $\log P_{oct/aq}$ of RFN and its metal complexes as a function of pH.

The incorporation of metals into the system has reduced the value of $\log P_{oct/aq}$; this can imply increasing the rate of diffusion of the ligand through the membrane. The reduction of $\log P_{oct/aq}$ by the metals suggests that the drug will be more water-soluble and will not aggregate in the absence of fluid.

4.2.4.6 Pyrazinecarboxamide and its Metal Complexes

The partition coefficients $\log P_{oct/aq}$ of PZA complexes as a function of pH is shown in Figure 4.14 below. The partition coefficient could not be explained in terms of speciation distribution because the pK_a of PZA could not be detected under the conditions of our potentiometry experiment. The $\log P_{oct/aq}$ values for the complexes were rationalised with respect to $\log P$ of PZA. The $\log P_{oct/aq}$ for PZA is in close agreement with the value of -0.60, reported in the literature.⁴⁶ For PZA-Cu the value of $\log P$ increased from -0.82 (pH 3.62) to -0.52 (pH 5.85) after which a constant $\log P$ value of -0.50 was observed from pH 6.62. For PZA-Ni the $\log P_{oct/aq}$ increased steadily with the increase in pH. For PZA-Zn the $\log P_{oct/aq}$ value of -0.51 was observed throughout the pH range. $\log P_{oct/aq}$ for PZA-Zn is thus independent of pH.

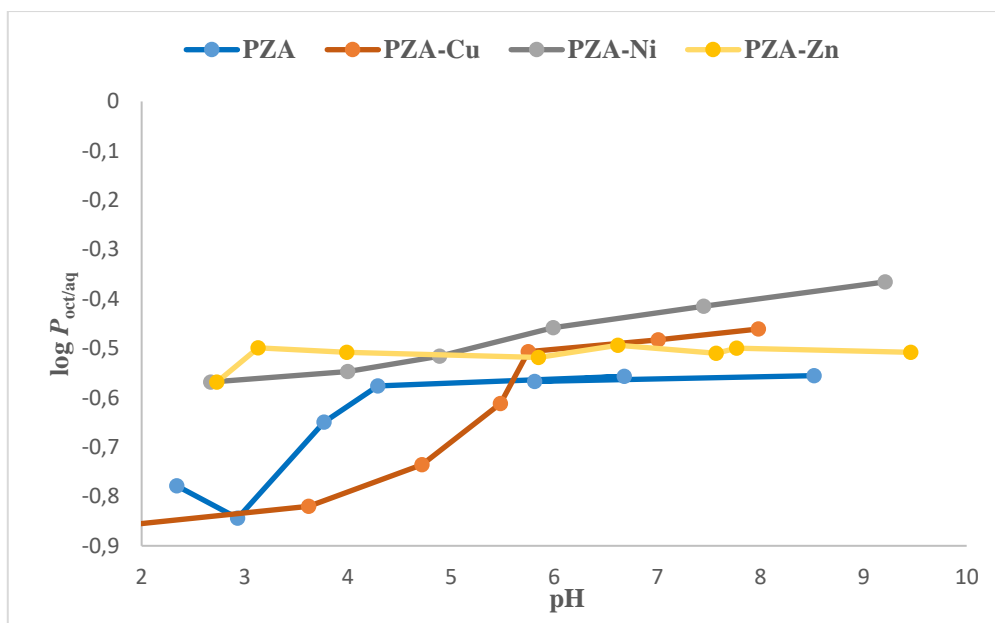


Figure 4.14: $\log P_{\text{oct/aq}}$ of PZA and its metal complexes as a function of pH.

It was observed that the incorporation of metals does not have a significant effect on the partition coefficient of PZA.

4.2.4.7 *P-aminosalicylic acid*

Partition coefficients $\log P_{\text{oct/aq}}$ of PAS and speciation curves as a function of pH are shown in Figure 4.15. The $\log P$ values are all positive, indicating that the ligand is lipophilic.

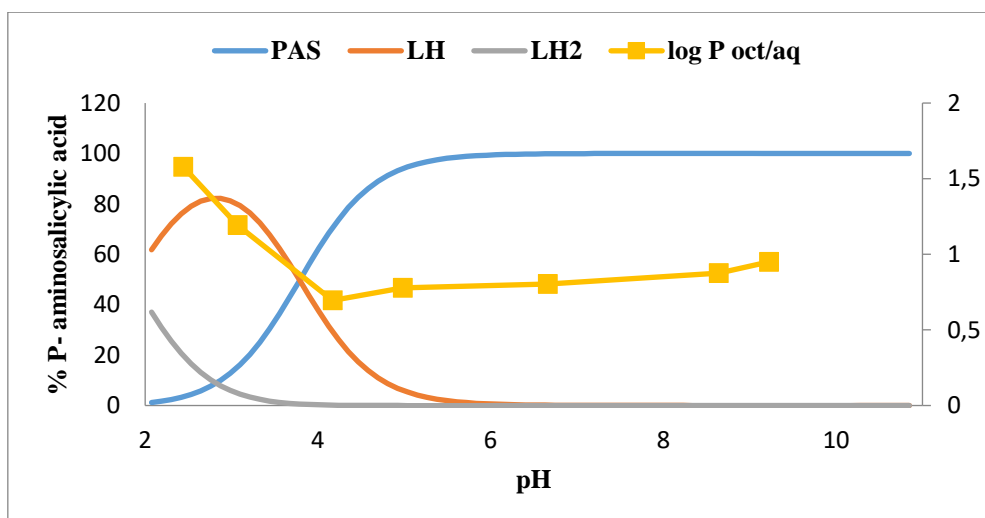


Figure 4.15: $\log P_{\text{oct/aq}}$ and speciation graph as a function of pH for the PAS system.

The speciation diagram for PAS shows the presence of LH and LH₂ species between pH 2.0 and 4.0. The log $P_{\text{oct/aq}}$ value of 1.58 can be assigned to the LH and LH₂ species. As the pH increases, the value of $P_{\text{oct/aq}}$ is reduced to about 0.80 and was steady throughout the entire pH range. The speciation graph reveals the presence of PAS between pH 4.0 and 11.0, and therefore log $P_{\text{oct/aq}}$ of 0.87 can be attributed to the presence of PAS. A log $P_{\text{oct/aq}}$ value of 0.91 has been reported in the literature for PAS.⁴⁷

4.2.4.8 *P-aminosalicylic acid-Cu(II) complex*

The distribution curve and the speciation graph for Cu(II) PAS as a function of pH are given in Figure 4.16. The distribution curve shows that log P decreased with an increase in pH (from pH 2.86 to 3.70) after which it became constant.

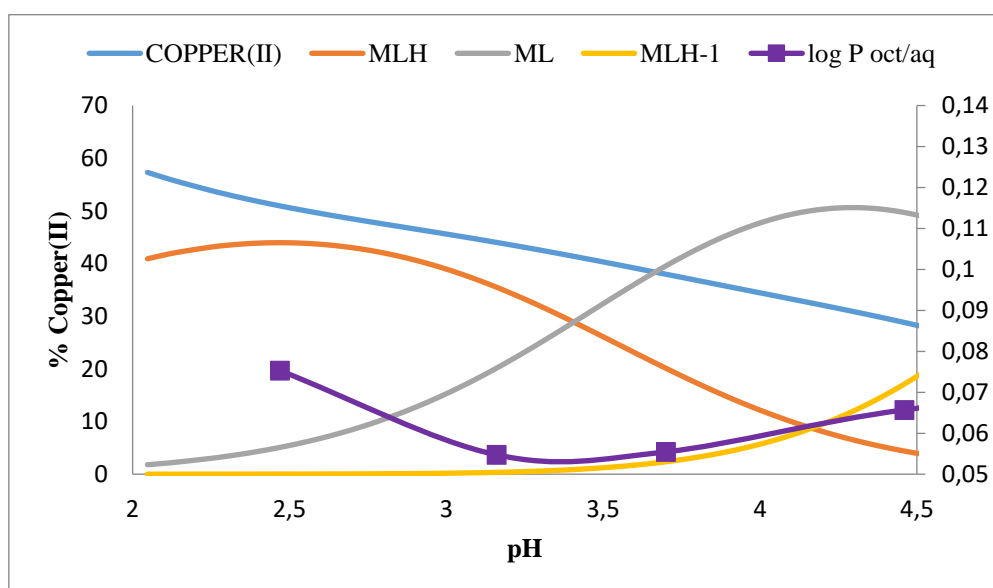


Figure 4.16: Log $P_{\text{oct/aq}}$ and speciation graph as a function of pH for the 1:1 Cu(II) PAS system.

From the speciation curve, around pH 2.09 -3.15, MLH is the predominant species; the log $P_{\text{oct/aq}}$ value of 0.075 at this pH range can be assigned to MLH species. The speciation curve reveals the presence of ML and MLH₋₁ species from pH 3.13 to pH 4.46; the distribution

coefficient did not change significantly in this pH range. Therefore the $\log P_{\text{oct/aq}}$ were not for a single species. The $\log P_{\text{oct/aq}}$ value of 0.066 can be attributed to the ML and MLH₋₁ species present at these pH values on the speciation graph.

4.2.4.9 *P-aminosalicylic acid and its Ni(II) and Zn(II) complexes*

The octanol/water partition coefficients as a function of pH for PAS and its Ni(II) and Zn(II) complexes are given in Figure 4.17. The shapes of the distribution curves were not due to metal complexation as, from potentiometric results, no complexation could be detected under the conditions of our experiment. Instead, the partition coefficient reflects the speciation of the ligand on its own.

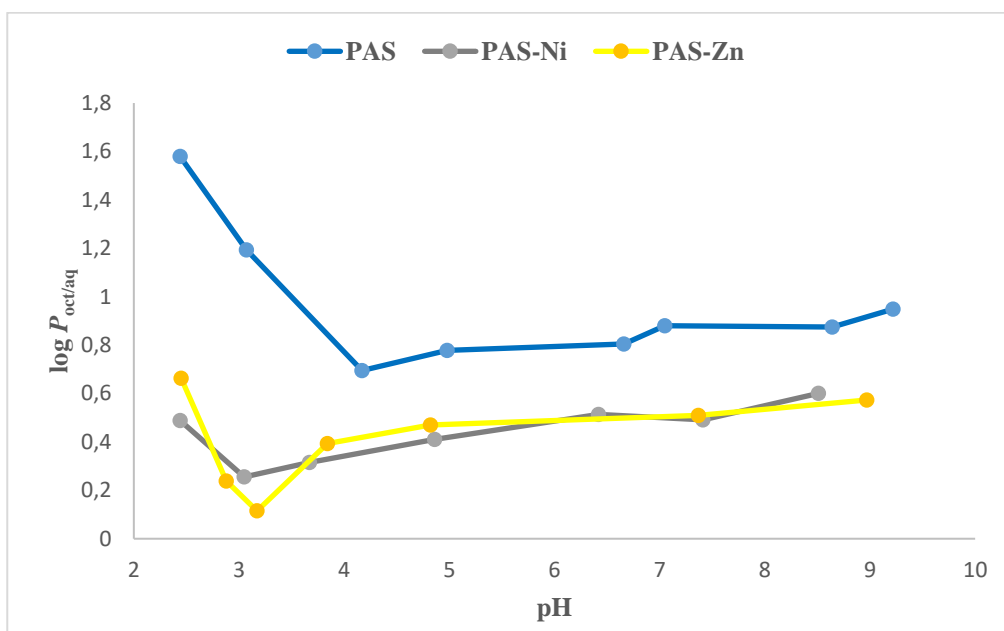


Figure 4.17: $\log P_{\text{oct/aq}}$ of PAS complexes as a function of pH.

Although no metal complexation takes place, the presence of the metal has had a small effect on the partition coefficient, decreasing it by ~ 0.4 log units. The reason for this behaviour is not known.

The ligand is more lipophilic at acidic pH for both the ligand as well as when the metal was incorporated. The pK_a of the carboxylic group is 3.78, which explains the decrease in $\log P_{\text{oct/aq}}$. A partition coefficient of 1.6 could therefore be assigned to the PAS when the carboxylic group is protonated (i.e. neutral) and this drops to 0.8 when the carboxylic group ionises.

4.2.5 Conclusion

The distribution graph for ISO and its complexes was rationalised in terms of the speciation graph; it was observed that the $\log P_{\text{oct/aq}}$ values were all negative, suggesting that they are hydrophilic. The partition coefficient data are consistent with the species revealed by the speciation graph.

A positive $\log P_{\text{oct/aq}}$ value obtained for RFN and its metal complexes implies they are lipophilic. The $\text{p}K_{\text{a}}$ of RFN which is lower than the pH of our present potentiometric study made the rationalisation by reference to speciation graph impossible. However, the presence of metals reduced the $\log P_{\text{oct/aq}}$ value of RFN from 2.30 to ~ 1.05 log units.

The values of $\log P_{\text{oct/aq}}$ are all negative for PZA and its complexes. The presence of metals does not have much effect on the partition coefficient.

PAS, as well as its metal complexes, are lipophilic since the $\log P$ values are positive. The results of $\log P_{\text{oct/aq}}$ values for PAS with copper agrees well with the speciation graph obtained from the potentiometric study. Metal complexation was not detected for nickel and zinc under our potentiometric conditions, but their presence decreased the $\log P_{\text{oct/aq}}$ value of PAS by ~ 0.4 log units.

4.4 Franz Diffusion Cells

4.4.1 Introduction

The skin is the largest organ in the body; it creates a boundary between the body and the outer environment and is metabolically active.^{48,49} Solute can penetrate through the skin *via* a transepidermal and a transappendageal route. The amount of drug that diffuses through the skin is determined by factors such as the physicochemical properties of the drug and the medium, in addition to the dosing conditions.

Permeability through biological membranes is significant in the absorption and distribution of medications. Poor permeability can arise due to several structural features, as well as membrane-based efflux mechanisms. Poor permeability can result in poor absorption across the gastrointestinal mucosa or poor distribution throughout the body. Dermal absorption of water has been tested in various species, including red cell membranes of dog, cat and beef.⁵⁰ The permeability coefficient (K_p) is the velocity of drug passing through the membrane in cm h^{-1} . The equation below gives the relation between permeability coefficient and steady-state flux:

$$K_p = \frac{J}{C_i} \quad (4.6)$$

where, J is the amount of permeant crossing the membrane at a constant rate ($\text{mg cm}^{-2} \text{h}^{-1}$), and C_i is the concentration of a ligand in the donor phase. The amount of permeant crossing the membrane J can be expressed as:

$$J = \frac{Q}{A.t} \quad (4.7)$$

The steady-state flux J dictates the rate and ease with which the permeant crosses a membrane under specified conditions. It is a dynamic property expressed in the unit of area per time (h).⁴⁶ The temperature is kept constant, and the magnitude of the diffusion coefficient is dependent

on the properties of the drugs and the diffusion medium as well as the interaction between them. The diffusion coefficient is an important parameter indicative of the diffusion mobility. It is prescribed for a given pair of species. The higher the diffusivity (of one substance with respect to another), the faster they diffuse into each other.

Q (mg) is the quantity of ligand/complex transported through the membrane in time t (h), and A is the area of exposed membrane in cm^2 . The amount of permeant crossing the membrane is calculated from the slope of the graph.⁴² The Franz diffusion cell method is one of the most common systems employed in *in vitro* skin diffusion studies, and it provides insight into the relationship between skin, drug and formulation^{51,52}, and primarily it is developed to determine the absorption and the rate of penetration of transdermal medication.⁵³ The Franz cell is used with excised human or animal skin. Artificial membranes are also employed when the biological membrane is not readily available. For a biological membrane, factors such as the time obtained, conditions of preservation and treatment, age, sex and weight of the membrane must be taken into consideration during the studies. These factors do not apply when an artificial membrane is used. The artificial membrane should possess minimum diffusion resistance to drugs and act as a barrier between the donor and acceptor phases.⁵⁴⁻⁵⁶ Artificial membrane has shown to be a promising model for biological membrane; it increases permeation rate and drastically reduces transport time from over 10 to 2 h.⁵⁷⁻⁵⁹ By eliminating the complexity of human and animal skin, the simple homogenous material is particularly useful for studying the basic mechanisms controlling passive transport.⁶⁰⁻⁶²

Ottaviani *et al.*⁶³ investigated the permeability coefficient of some drugs through human skin and an artificial membrane comprising a dimethylsiloxane (silicone) membrane. Silicone membranes have been extensively used as simple lipid-like membrane models for *in vitro* percutaneous penetration studies,⁶⁴⁻⁶⁶ because they offer a nonporous, hydrophobic, and relatively inert, reproducible barrier.⁶⁷ The permeability coefficients obtained through human

skin ($\log K_p$) and through a silicone membrane using a diffusion cell ($\log K_{p(\text{sil})}$) are listed in Table 4.3 below.

Table 4.3: Permeability coefficients obtained through human skin ($\log K_p$) and silicone membrane using diffusion cell ($\log K_{p(\text{sil})}$)

Compound	$\log K_p$ ⁶⁸	$\log K_{p(\text{sil})}$ ⁶⁴
Nicotine	-5.26	-4.29
Phenol	-5.64	-4.45
4-nitrophenol	-5.81	-5.08
Lidocaine	-5.32 ⁶⁹	-4.05
Salicylic acid	-5.45	-4.70
Thymol	-4.83	-3.68

The results showed that the artificial membrane could mimic the main properties of human stratum corneum.

The Franz cell is based on vertical diffusion between donor and acceptor phases. In the present study, a horizontal Franz cell (Figure 4.18) fitted with an artificial membrane (Cerasome 9005), was used. Cerasome 9005 was purchased from Germany (Lipoid GmbH, Ludwigshafen, 2008). This membrane is a lipid solution which imitates human stratum corneum, which is the outer layer of the epidermis; it forms a barrier to protect underlying tissues from infection, dehydration, chemical and mechanical stress. The lipids of the human stratum corneum regulate skin permeability. The most suitable method of imitating partition into a biological membrane is using a membrane composed of numerous phospholipids as a model system.⁷⁰

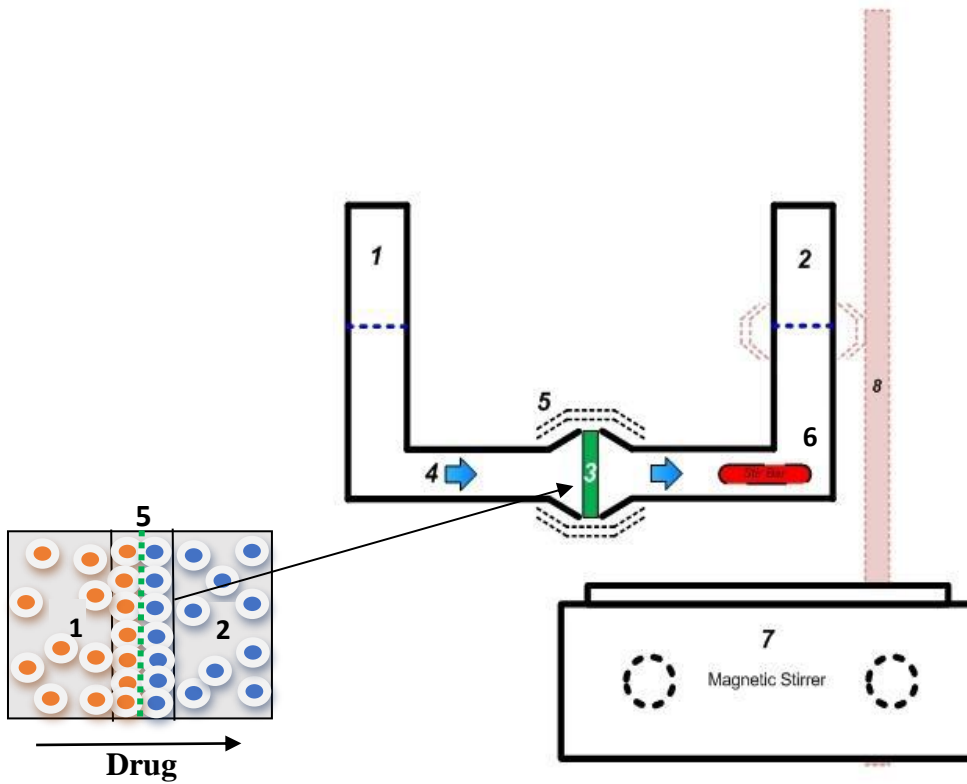


Figure 4.18: A modified Franz diffusion cell apparatus.

1. Donor phase filled with 20 ml ligand/complex.
2. Receiver phase filled with 0.02 M HCl.
3. The artificial membrane (0.065 g).
4. Passive diffusion direction.
5. Clamp.
6. Stirrer bar.
7. Magnetic stirrer.
8. Burette stand for the clamp.

4.4.2 Experimental

The receiver cell was filled with 20 ml of 0.02 M HCl. The ligand/complex solutions (0.002 M) were prepared in 0.02 M HCl, and a 20 ml sample at pH 2.0 was placed in the donor phase compartment along with semi-permeable membrane used as a barrier between donor and receptor compartments. The experiment was carried out at pH 2.0 to mimic the acid condition of the stomach. The artificial membrane was prepared using a filter paper (Whatman, 2.54 cm² disc and thickness 0.002 cm) which was submerged in Cerasome 9005, dried for a few minutes at room temperature. To determine the quantity of lipid absorbed, the membrane was weighed before and after soaking in Cerasome 9005. The available diffusion area between the cells was 0.6217 cm². The medium was magnetically stirred for uniform drug distribution and was maintained at a temperature of 25 °C; samples were removed at different times. During the experiment, both cells were covered to prevent evaporation. The concentration of the ligand in the complexes was determined spectrophotometrically. The wavelength of maximum absorption was determined for the ligands ISO, RFN, PAS and PZA as 263 nm, 479 nm, 265 nm and 269 nm respectively. Measurements were done in triplicate, using the points from 0-56 hours. Results are expressed as mean \pm SE.

4.4.3 Results and Discussion

4.4.3.1 Isoniazid and its Metal Complexes

Plots of the variation of ISO concentration with time at pH 2 are shown in Figure 4.19. Table 4.4 shows the diffusion flux, J , permeability coefficient K_p and shown graphically in Figures 4.20 and 4.21, respectively.

The steady-state flux was calculated from the gradient in Figure 4.19, and the permeability coefficient (K_p) obtained from the relationship between the flux, and the initial concentration of ISO added to the donor phase.

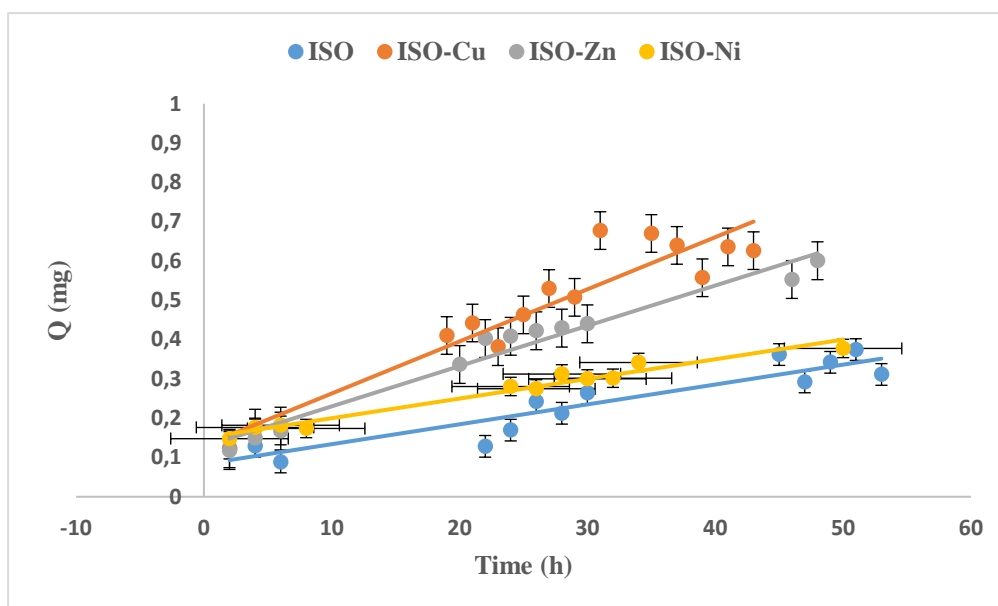


Figure 4.19: Variation in the amount of ISO vs time through a Cerasome 9005 membrane at pH 2.00.

ISO has a molecular weight of $137.14 \text{ g mol}^{-1}$, which is less than 600 g mol^{-1} and so is ideally suited for passive diffusion across the skin and biomembranes.⁷¹

Table 4.4: Flux of diffusion J ($\text{mg cm}^{-2}\text{h}^{-1}$) and permeability coefficient K_p (cm h^{-1}) of ISO and its metal complexes through Cerasome 9005 membranes at pH 2.00.

Drug and Metal Complexes	J ($\text{mg cm}^{-2}\text{h}^{-1}$) $\times 10^{-3}$	K_p (cm h^{-1})
ISO	8.6 ± 1.1	0.068 ± 0.009
ISO-Cu	20.6 ± 2.3	0.400 ± 0.045
ISO-Ni	7.2 ± 1.2	0.200 ± 0.031
ISO-Zn	15.8 ± 1.1	0.145 ± 0.011

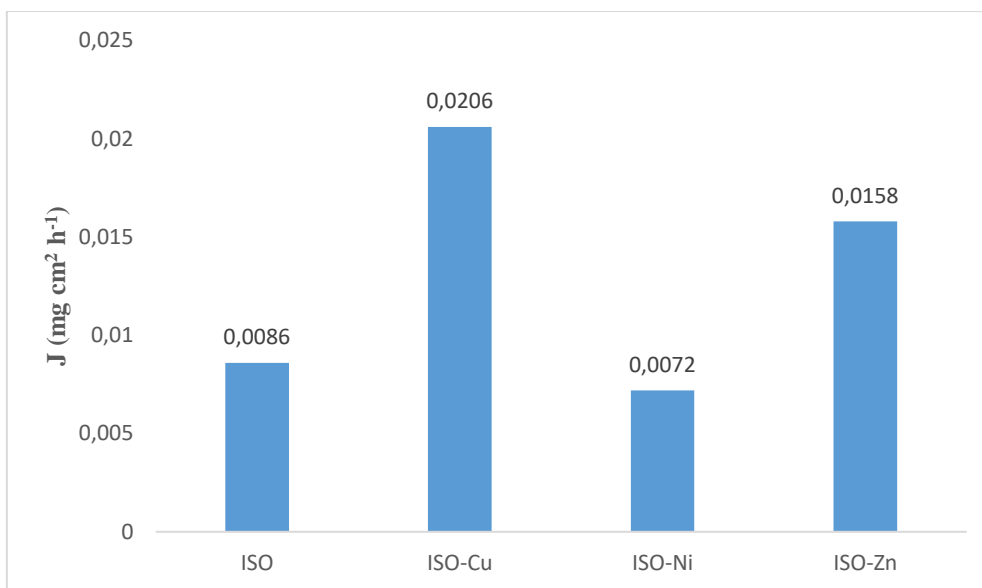


Figure 4.20: Influence of metals on the flux of ISO through Cerasome 9005 membrane in modified Franz cell from 0-56 hrs at pH 2.00.

From Figure 4.20, above, the steady-state flux, which is the total amount of ISO that permeates the membrane per unit area per unit time, is in the order $\text{Cu(II)} > \text{Zn(II)} > \text{ISO} > \text{Ni(II)}$. Note that this flux is dependent on the initial concentration in the donor phase, which was not the same in each experiment. The presence of Cu(II) and Zn(II) has increased the rate at which ISO passes through the membrane.

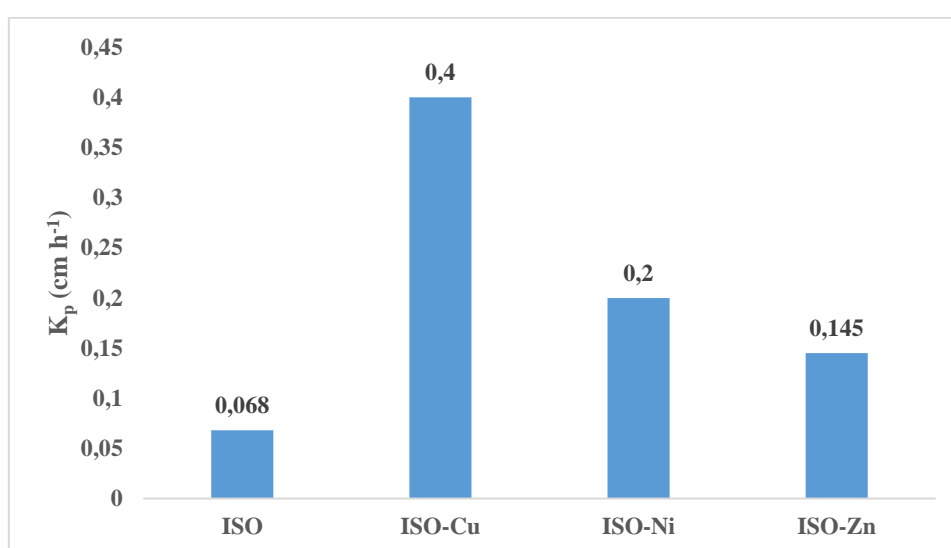


Figure 4.21: Effect of metals on the permeability of ISO through Cerasome 9005 membrane at pH 2.00.

Included in Figures 4.19 and 4.21 are the results for ISO without coordinating metal. From Figure 4.21, it is clear that the metals can promote the passage of the ligand through the membrane. The permeability is in the order Cu(II) > Ni(II) > Zn(II). ISO possesses three ionisation constants (pK_a), 1.8 (hydrazine nitrogen); 3.5 (pyridine nitrogen) and 10.8 (acidic group) with an overall isoelectric point (pI) of 1.82. Since the pH of the vehicle is higher than that of the pI , the ISO molecule will, therefore, carry a net negative charge.⁷² The permeability of ISO has been reported as $0.033 \pm 0.006 \text{ cm h}^{-1}$ where porcine skin was used.⁷³ In our experiment, the permeability coefficient was $0.068 \pm 0.009 \text{ cm h}^{-1}$ which is higher than reported but is expected for an artificial membrane.⁷⁴

4.4.3.2 Rifampicin and its Metal Complexes

The variation of the concentration of RFN with time through Cerasome 9005 membrane at pH 2.00 is revealed in Figure 4.22.

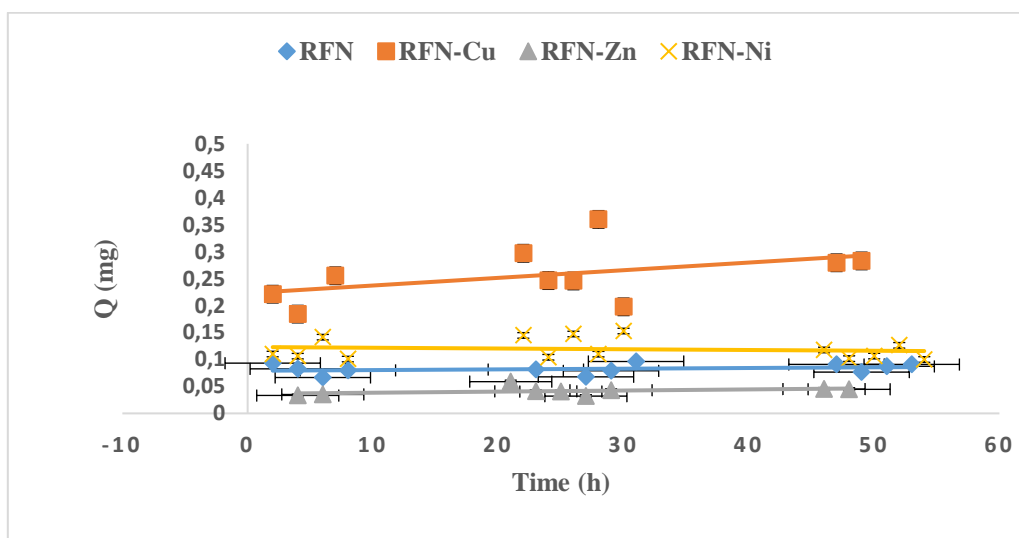


Figure 4.22: Variation in the amount of RFN vs time through Cerasome 9005 membrane at pH 2.00.

The value of the steady flux J ($\text{mg cm}^{-2} \text{h}^{-1}$) and the permeability coefficient K_p (cm h^{-1}) are shown graphically on Figures 4.23 and 4.24 respectively. The corresponding standard deviations for RFN and its complexes are shown in Table 4.5.

The flux of RFN is independent of time and this is reflected in the standard error.

Table 4. 5: Flux of diffusion J ($\text{mg cm}^{-2} \text{h}^{-1}$) and permeability coefficient K_p (cm h^{-1}) of RFN and its metal complexes through Cerasome 9005 membrane at pH 2.00.

Drug and Metal Complexes	J ($\text{mg cm}^{-2} \text{h}^{-1}$) $\times 10^{-3}$	K_p (cm h^{-1})
RFN	0.34 ± 0.3	0.003 ± 0.002
RFN-Cu	2.5 ± 2.5	0.07 ± 0.06
RFN-Zn	0.21 ± 0.5	0.002 ± 0.003

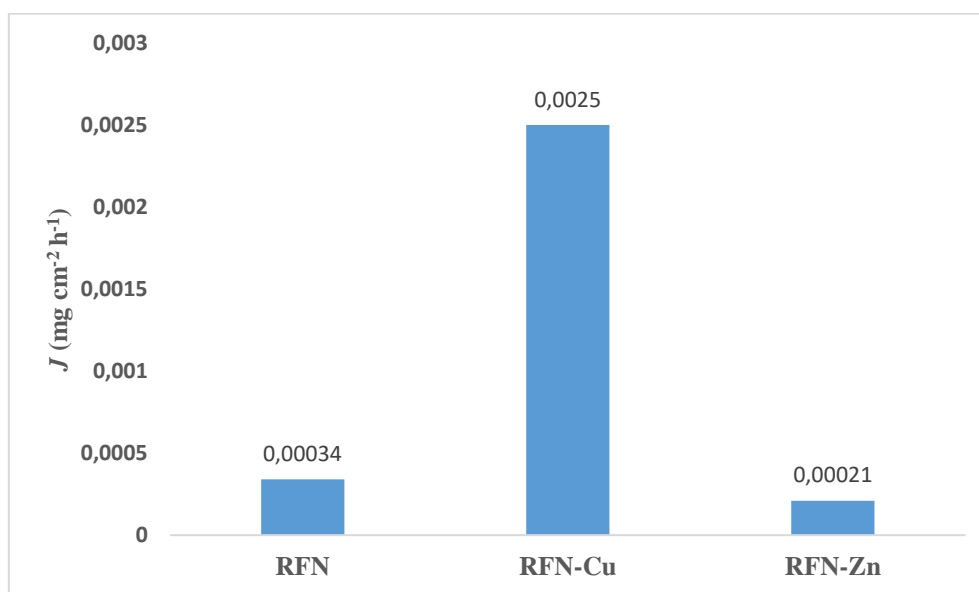


Figure 4.23: Influence of metals on the flux of RFN through Cerasome 9005 membrane in modified Franz cell from 0-56 hrs at pH 2.00.

From Figure 4.23 and 4.24, it was observed that the incorporation of copper improved the amount of RFN crossing the membrane significantly. Zn(II) did not enhance the amount of ligand diffusing through the membrane. This finding may have implications for the study of

the mechanism of action of RFN and possible copper supplement for improving the activity of RFN.

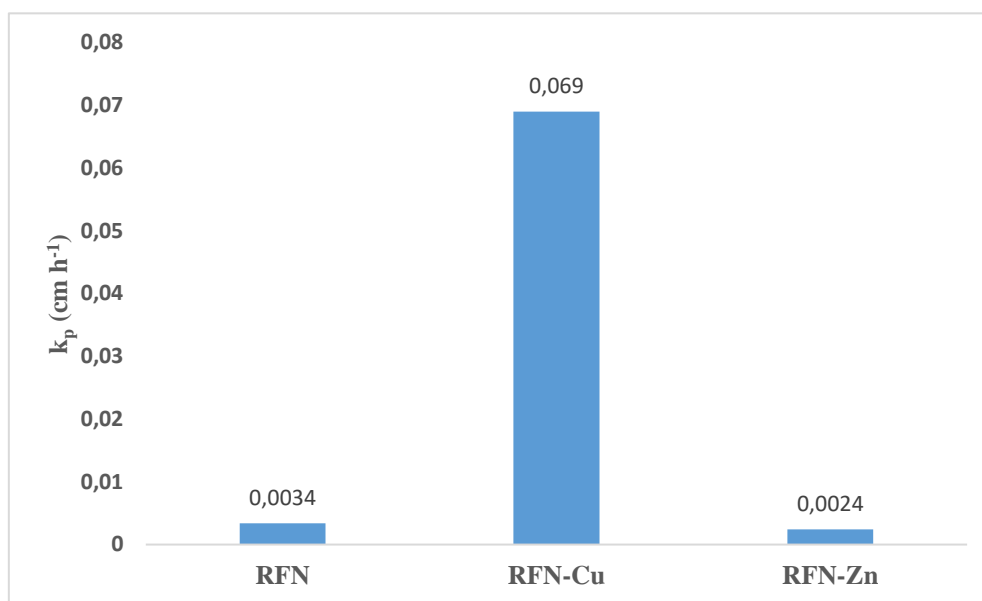


Figure 4.24: Effect of metals on the permeability of RFN through Cerasome 9005 membrane at pH 2.00.

The permeability coefficient of RFN has previously been determined in three segments of the rat intestine by employing the everted gut sac model; the apparent permeability coefficient values were 4.856×10^{-6} , 2.11×10^{-6} and 2.149×10^{-6} cm sec⁻¹ in the duodenum, jejunum and ileum respectively.⁷⁵ A permeability coefficient of 0.0034 ± 0.0020 cm h⁻¹ (9.4×10^{-7} cm s⁻¹) was obtained when an artificial membrane was used in the present study. The incorporation of copper enhanced the permeability of RFN 20-fold.

4.4.3.3 *P-aminosalicylic acid and its Metal Complexes*

A plot of the amount of PAS, against time, passing through the Cerasome 9005 membrane at pH 2.00 is depicted in Figure 4.25.

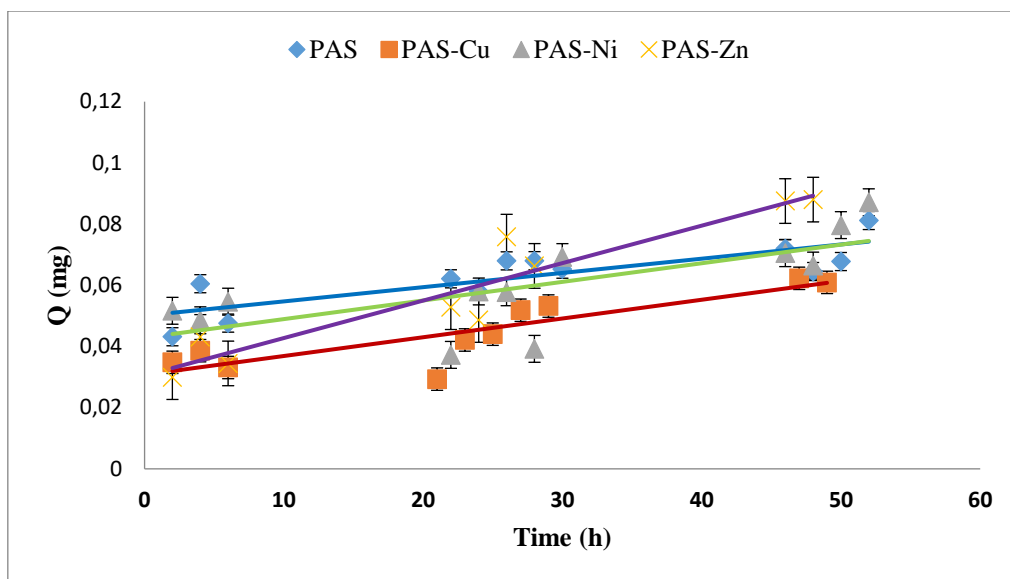


Figure 4.25: Variation in the amount of PAS vs time through Cerasome 9005 membrane at pH 2.00.

Flux values J ($\text{mg cm}^{-2} \text{h}^{-1}$), permeability coefficient K_p (cm h^{-1}) and their corresponding standard errors (SEs) for the metal complexes of PAS are shown in Table 4.6. The flux value J and permeability coefficient K_p are presented graphically in Figures 4.26 and 4.27, respectively.

Table 4.6: Flux of diffusion J ($\text{mg cm}^{-2} \text{h}^{-1}$) and permeability coefficient K_p (cm h^{-1}) of PAS and its metal complexes through Cerasome 9005 membrane at pH 2.00.

Drug and Metal Complexes	J ($\text{mg cm}^{-2} \text{h}^{-1}$) $\times 10^{-3}$	K_p (cm h^{-1})
PAS	0.8 ± 0.2	0.14 ± 0.03
PAS-Cu	1.0 ± 0.2	0.15 ± 0.03
PAS-Ni	1.1 ± 0.3	0.13 ± 0.04
PAS-Zn	1.9 ± 0.3	0.27 ± 0.04

The incorporation of Zn(II) increased the diffusion of the ligand through the membrane, while Cu(II) and Ni(II) did not improve diffusion (Figure 4.26). The effect of incorporation of metals on permeability of the ligand is shown in Figure 4.27. In the light of this result, if Zn(II) is incorporated into PAS then an increase in drug absorption could be expected.

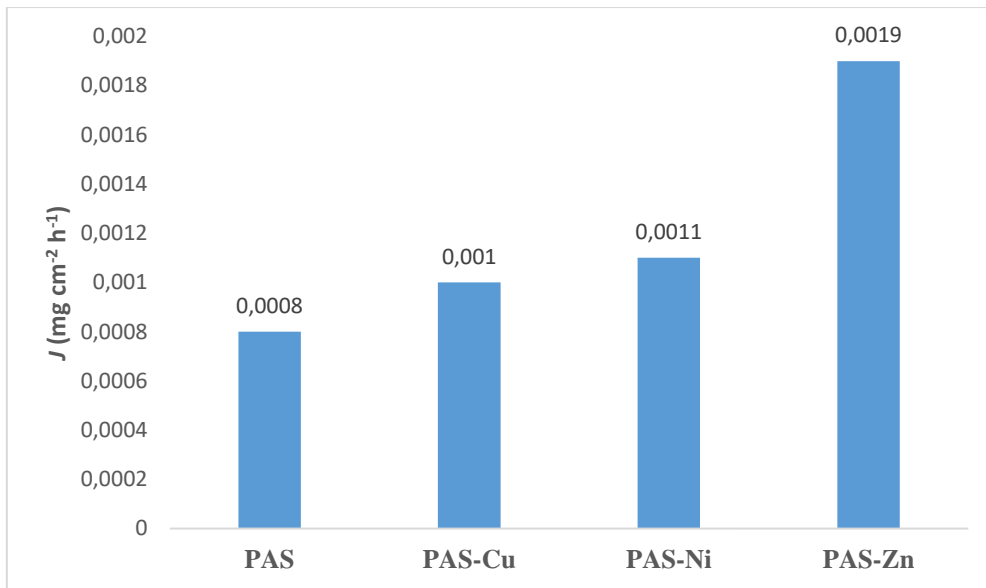


Figure 4.26: Influence of metals on the flux of PAS through Cerasome 9005 membrane in modified Franz cell from 0-56 hrs at pH 2.00.

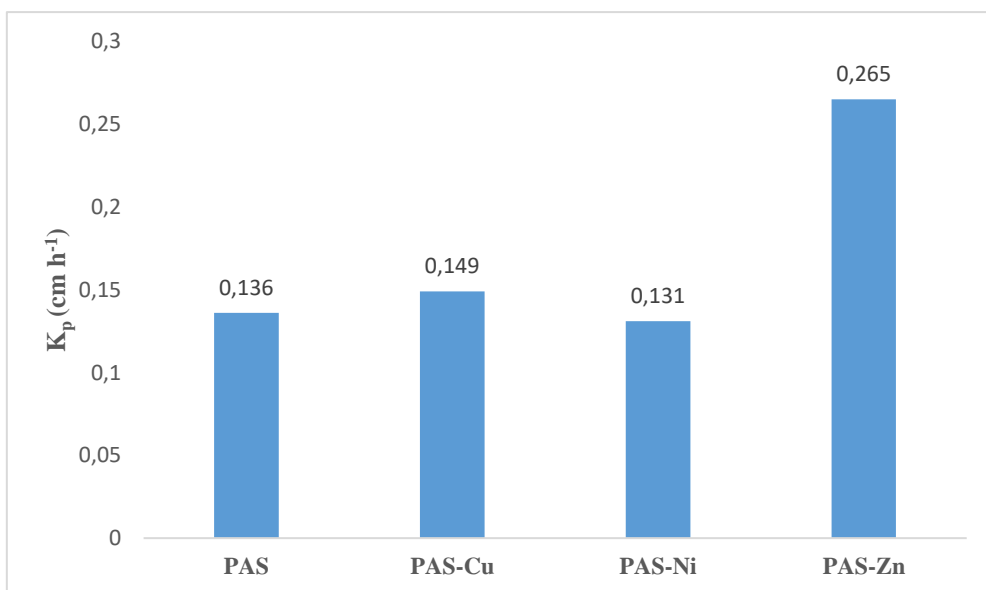


Figure 4.27: Effect of metals on the permeability of PAS through Cerasome 9005 membrane at pH 2.00.

4.4.3.4 Pyrazinecarboxamide and its Metal Complexes

The effect of metals on the diffusion of PZA through Cerasome 9005 membrane at pH 2.00 was studied for 54 h. The results are presented in Figure 4.28.

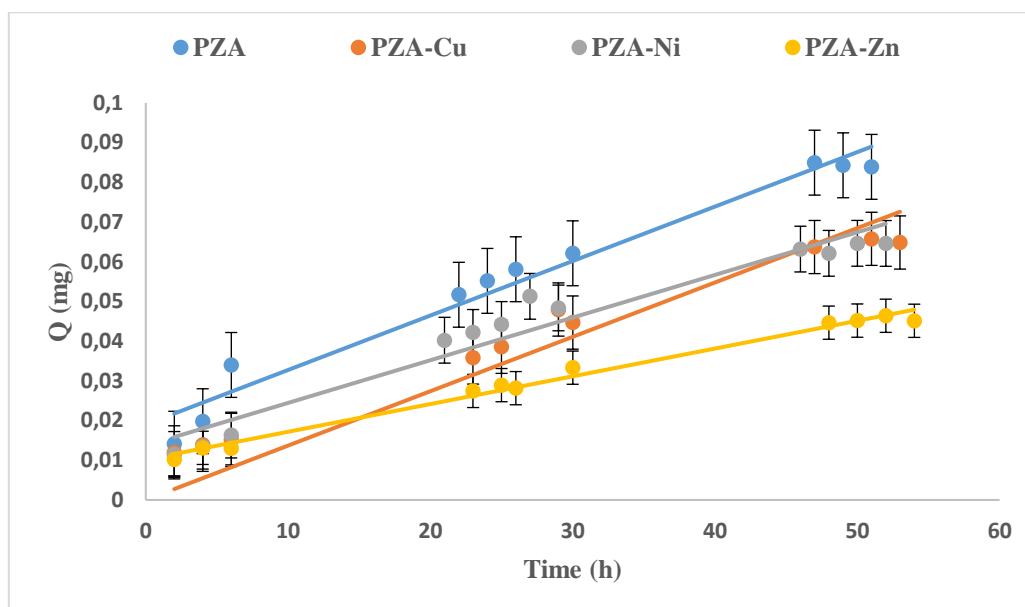


Figure 4.28: Variation in the amount of PZA vs time through Cerasome 9005 membrane at pH 2.00.

The flux value and permeability coefficients are presented in Table 4.7 and are shown graphically in Figures 4.29 and 4.30 respectively.

Table 4.7: Flux of diffusion J and permeability coefficient K_p of PZA complexes through Cerasome 9005 membrane at pH 2.

Drug and Metal Complexes	J ($\text{mg cm}^{-2} \text{h}^{-1}$) $\times 10^{-3}$	K_p (cm h^{-1})
PZA	2.0 ± 0.1	0.100 ± 0.006
PZA-Cu	1.70 ± 0.09	0.098 ± 0.005
PZA-Ni	0.2 ± 0.1	0.103 ± 0.009
PZA-Zn	1.10 ± 0.04	0.089 ± 0.004

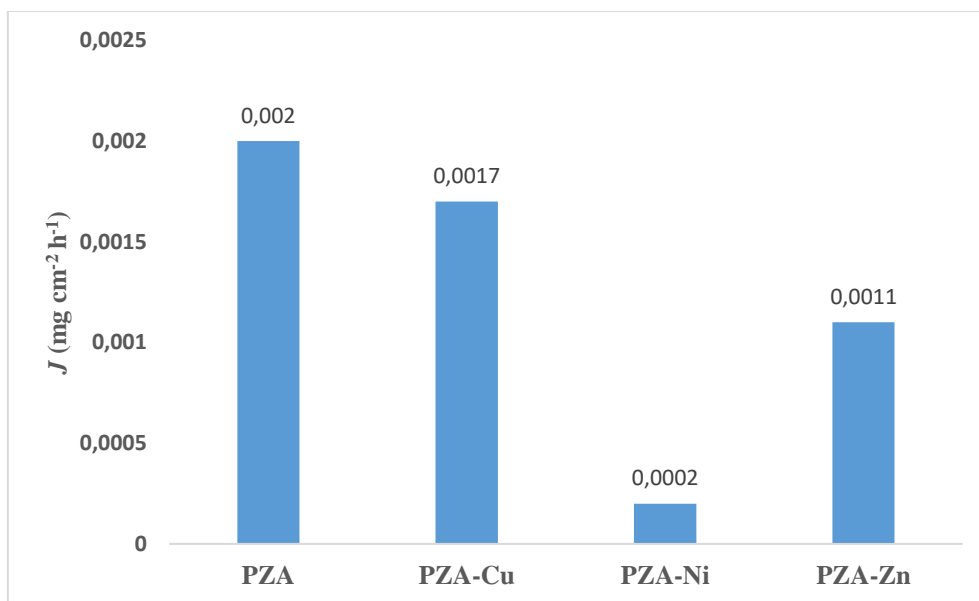


Figure 4.29: Influence of metals on the flux of PZA through Cerasome 9005 membrane in modified Franz cell from 0-56 hrs at pH 2.00.

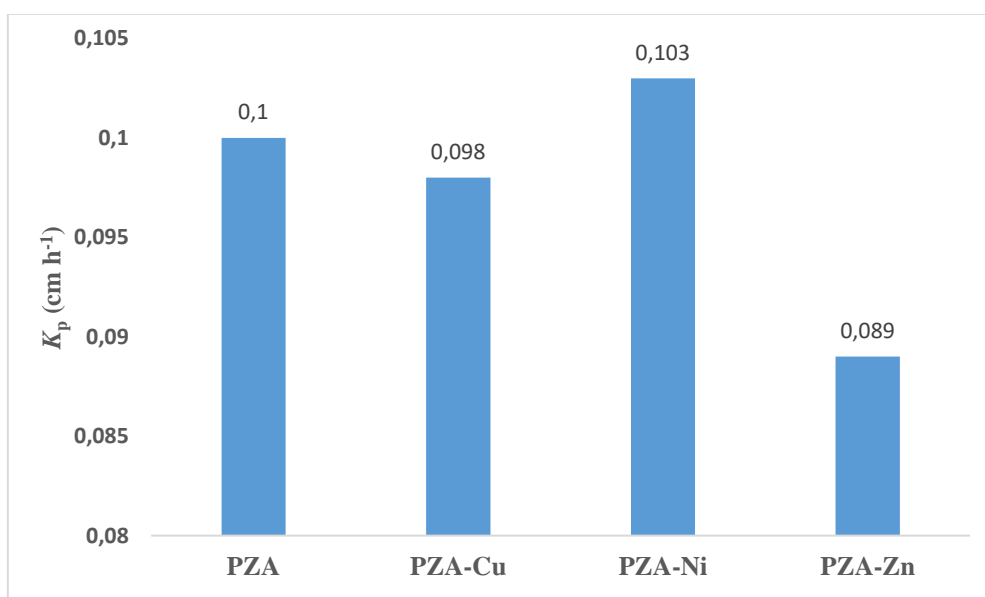


Figure 4.30: Effect of metals on the permeability of PZA through Cerasome 9005 membrane at pH 2.00.

It was observed that the presence of Cu(II), Ni(II) and Zn(II) did not significantly have an impact on the diffusion and permeability coefficient of PZA through the membrane.

4.4.3.5 Comparison of permeability coefficients K_p for the ligands and complexes.

The plot of the permeability coefficients K_p for the ligands (ISO, RFN, PAS and PZA) and their complexes are shown in Figure 4.31.

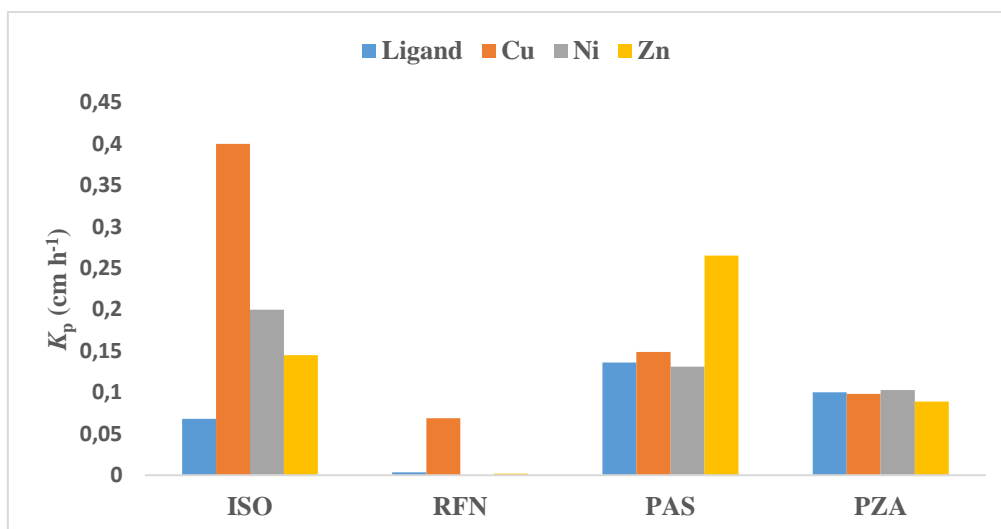


Figure 4.31: Comparison of the permeability coefficients for the ligands and complexes.

Studies have shown that the permeability of a series of related drugs can be compared for a selection of a drug candidate with a high permeability.⁷⁶ The result of the comparison in the present study shows that the permeability coefficients of the ligands are in the order $\text{PAS} > \text{PZA} > \text{ISO} > \text{RFN}$, with K_p values 0.136, 0.100, 0.068 and 0.003 cm h^{-1} respectively. The presence of the ligand alone serves as a control.

The presence of Cu(II), Ni(II) and Zn(II) improved the permeability coefficient of ISO with K_p values between 0.145 and 0.400 cm h^{-1} ; Cu(II) enhanced the RFN permeability coefficient with a K_p value of 0.07 cm h^{-1} , while Zn(II) enhanced the permeability coefficient of PAS with a K_p value of 0.265 cm h^{-1} . The incorporation of Cu(II), Ni(II) and Zn(II) had no effect on PZA. The values of K_p were then compared with that of metoprolol which was chosen as the reference compound for permeability and $\log P$. The intestinal permeability of metoprolol was reported as 0.54 cm h^{-1} and the drug is classified as a high-permeability drug.⁷⁷ The K_p values obtained

in the present study are all lower than the K_p of the reference compound (metoprolol). Therefore the drugs, as well as their complexes, can be classified as low-permeability drugs.

4.4. Relationship between logarithm of permeability coefficient $\log K_p$ and octanol/water partition coefficient $\log P_{\text{oct/aq}}$ of the ligand and complexes.

Previous studies by Potts and Guy⁷⁸ have analysed permeability data using a model which depends upon the size of the drug (MW), and its octanol/water partition coefficient. A correlation between $\log K_p$ and $\log P_{\text{oct/aq}}$ was therefore investigated since the two parameters have been determined. Tables 4.8-4.11 show the permeability and partition coefficient values of the ligands in the presence of the different metals. Graphical representations of these data appear in Figures 4.32-4.35.

Table 4.8: The permeability and partition coefficient values of ISO in the presence of the different metals.

Drug and Metal Complexes	$-\log P_{\text{oct/aq}}$	$-\log K_p$
ISO	0.61 ± 0.02	1.167 ± 0.016
ISO-Cu	0.61 ± 0.03	0.398 ± 0.002
ISO-Ni	0.71 ± 0.03	0.699 ± 0.004
ISO-Zn	0.78 ± 0.02	0.839 ± 0.006

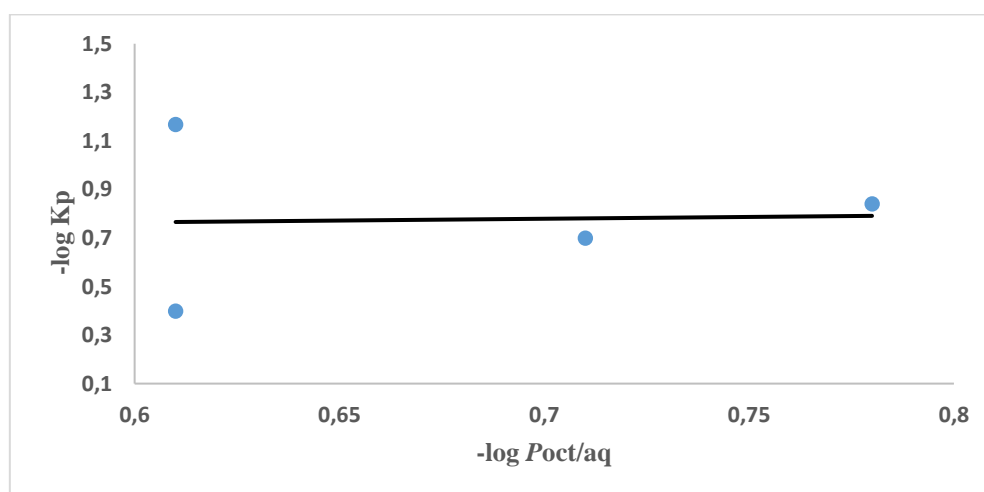


Figure 4.32: Logarithm of permeability coefficient $\log K_p$ plotted against logarithm of partition coefficient for ISO.

Table 4.9: The permeability and partition coefficient values of RFN in the presence of the different metals.

Drug and Metal Complexes	$-\log P_{\text{oct/aq}}$	$-\log K_p$
RFN	2.310 ± 0.008	2.47 ± 0.22
RFN-Cu	0.750 ± 0.018	1.16 ± 0.04
RFN-Ni	1.640 ± 0.014	-
RFN-Zn	1.750 ± 0.007	2.98 ± 0.74

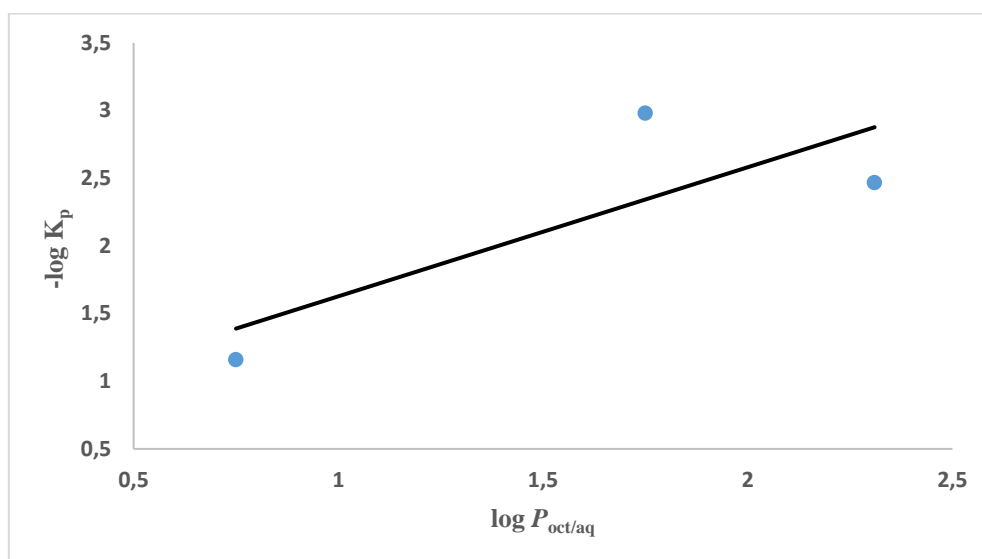


Figure 4.33. Logarithm of permeability coefficient $\log K_p$ plotted against logarithm of partition coefficient for RFN.

Table 4.10: The permeability and partition coefficient values of PAS in the presence of the different metals.

Drug and Metal Complexes	$\log P_{\text{oct/aq}}$	$-\log K_p$
PAS	0.800 ± 0.030	0.867 ± 0.001
PAS-Cu	0.060 ± 0.001	0.827 ± 0.001
PAS-Ni	0.510 ± 0.006	0.883 ± 0.002
PAS-Zn	0.510 ± 0.018	0.577 ± 0.001

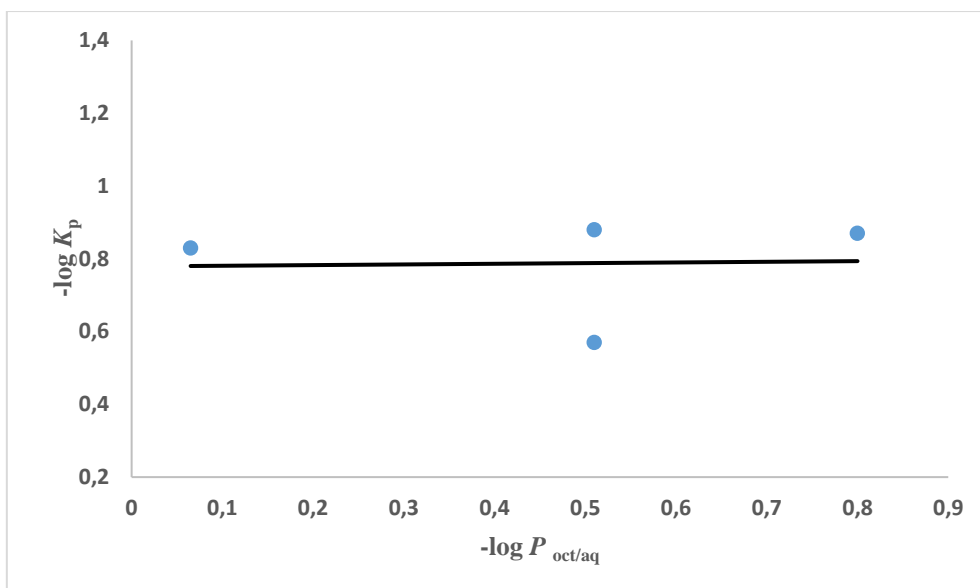


Figure 4.34: Logarithm of permeability coefficient $\log K_p$ plotted against logarithm of partition coefficient for PAS.

Table 4.11: The permeability and partition coefficient values of PZA in the presence of the different metals.

Drug and Metal Complexes	$-\log P_{\text{oct/aq}}$	$-\log K_p$
PZA	0.560 ± 0.018	1.0000 ± 0.001
PZA-Cu	0.510 ± 0.017	1.0087 ± 0.001
PZA-Ni	0.420 ± 0.002	0.9871 ± 0.001
PZA-Zn	0.510 ± 0.002	1.0451 ± 0.001

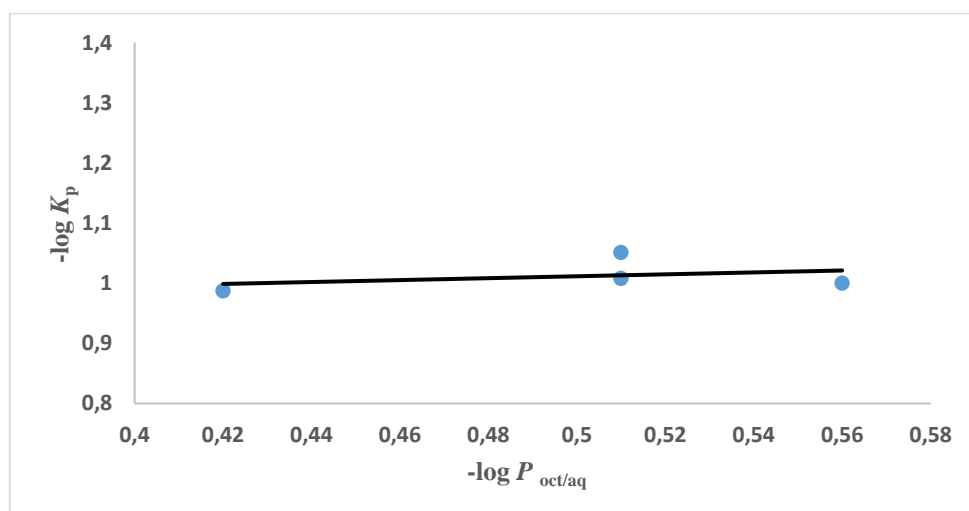


Figure 4.35: Logarithm of permeability coefficient $\log K_p$ plotted against logarithm of partition coefficient for PZA.

Figures 4.32-4.35 show the possible correlation between the logarithm of permeability coefficient $\log K_p$ and the octanol/water partition coefficient $\log P_{\text{oct/aq}}$ of the ligands alone as well as in the presence of metal ions. The correlation coefficients obtained from Figures 4.32, 4.34 and 4.35 are 0.0015, 0.0014, and 0.1130 for ISO, PAS and PZA respectively. The values are far from 1 demonstrating that there is no correlation between the logarithm of permeability and the logarithm of octanol/water partition coefficient of the ligands. The correlation coefficient obtained for RFN, in Figure 4.33, is 0.6449 which indicates that 65% of $\log K_p$ could be explained by $\log P_{\text{oct/aq}}$. However, the very low diffusion and associated errors encountered with RFN make this suspect.

Since Potts and Guy⁷⁸ did not distinguish between ligands, we therefore decided to plot the $\log K_p$ vs $\log P_{\text{oct/aq}}$ as well as the $\log K_p$ vs molecular weight (MW) data obtained for all ligands and their complexes together (Figures 4.36 and 4.37).

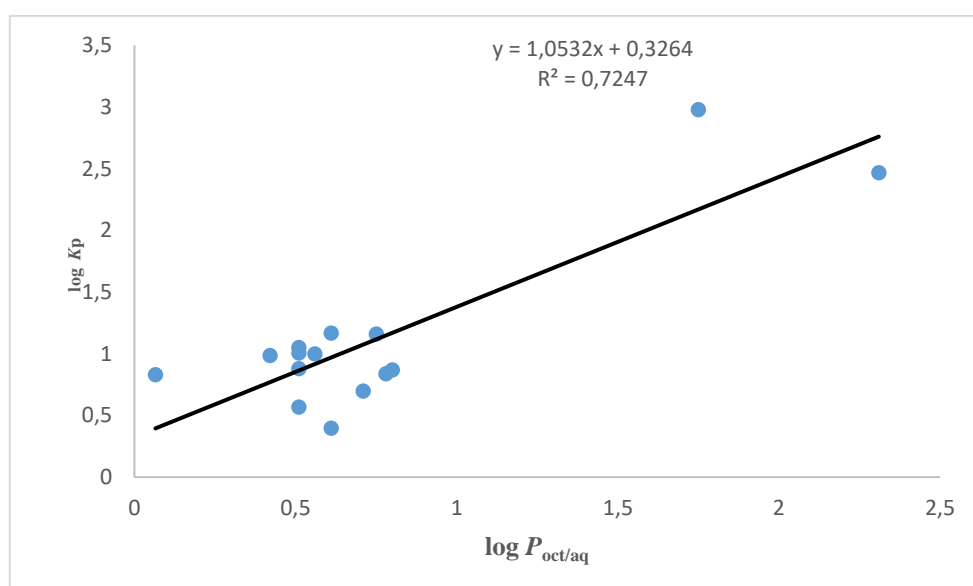


Figure 4.36: Logarithm of permeability coefficients $\log K_p$ plotted against logarithm of partition coefficient for all ligands and complexes.

The correlation coefficient obtained from Figure 4.36, $R^2 = 0.72$, indicates that there is a correlation between permeability and partition coefficient.

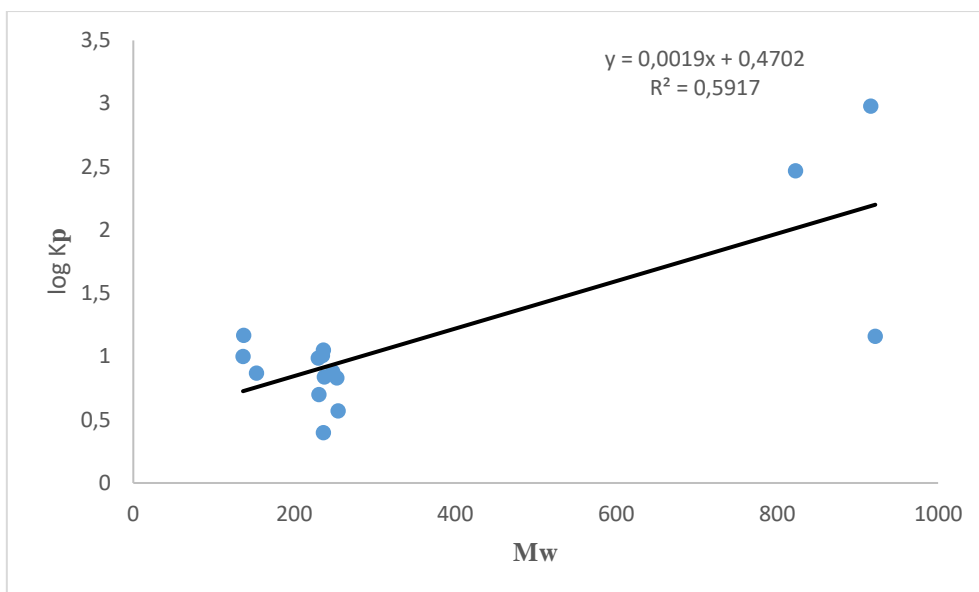


Figure 4.37: Logarithm of permeability coefficients $\log K_p$ plotted against molecular weight for all ligand and complexes.

Linear regression analysis of $\log K_p$ vs MW (Figure 4.37) gave an R^2 value of 0.59. The results of the correlation from Figures 4.36 and 4.37 show that there is a correlation between $\log K_p$ and either $\log P_{\text{oct/aq}}$ or MW .

Potts and Guy⁷⁸ have proposed a quantitative structure-permeability relationship model which depends upon both the size of the drug (MW) and $P_{\text{oct/aq}}$.⁷⁸

$$\text{Log } K_p = \text{Log } (D^0/h) + f \text{Log } K_{o/w} - \beta MW \quad (4.8)$$

where, D^0 is the diffusivity of a hypothetical molecule having zero molecular weight, h is the membrane thickness, f is a constant which accounts for the difference between the partitioning domain presented by octanol and the membrane lipids, and β' is a constant which includes a conversion factor for the substitution of molecular weight for molecular volume.

The average value of the intercept $\log (D^0/h)$, the slope (β') and f after considering species Cu(II), Ni(II) and Zn(II) complexes of ISO, PAS and PZA, as well as Cu(II) and Zn(II) complexes of

RFN, each solvated with 2H₂O molecules, were as follows: $\log (D^0/h) = 0.26 \pm 0.16, \beta' = 0.00078 \pm 0.0001$ and $f = 0.76 \pm 0.24$. Equation 4.8 can thus be written as

$$\text{Log } K_p = 0.26 + 0.76 \text{ Log } P_{\text{oct/aq}} - 0.00078 MW \quad (4.9)$$

Multiple linear regression analysis of $\log K_p$ upon $\log P_{\text{oct/aq}}$ and MW gave an R^2 value of 0.77, which means that there is a correlation between $\log K_p$ and $\log P_{\text{oct/aq}}$ or MW . The values of $\text{Log } (D^0/h), f,$ and β' found by Flynn for 90 drugs⁷⁹ were -2.72, 0.71 and 0.0061 respectively. The diffusivity of these charged complexes is higher than expected and f is similar as the charge of the complex has a similar effect on the octanol and membrane partitioning. This further supports the conclusion that for a labile drug and its complexes, factors other than size and partition coefficient are significant.

4.5 Conclusion

The amount of ISO transferred from aqueous solution to organic layer changes with pH and with the presence of different metal ions. The result showed that ISO, as well as the metal complexes under study, had $\log P_{\text{oct/aq}}$ values below zero, indicating that the ligand and the complexes are hydrophilic. The presence of metal greatly enhanced the permeation of ISO through an artificial membrane in the order $\text{Cu(II)} > \text{Zn(II)} > \text{Ni(II)} > \text{ISO}$. Statistical analysis of the results showed that there was no correlation between the logarithm of partition and permeability coefficients. This implies that $\log P_{\text{oct/aq}}$ is not as good a measure of absorption of ISO as $\log K_p$.

The $\log P_{\text{oct/aq}}$ values for RFN and its complexes are all positive indicating that they are all lipophilic. The comparison of the permeability coefficients of the ligands reveals that RFN, which is the most lipophilic, is the least permeable. This might be attributed to the fact that RFN was entrapped within the membrane hindering the diffusion through the membrane. However, the incorporation of Cu(II) reduced $\log P_{\text{oct/aq}}$ and enhanced the permeability of RFN through the membrane.

The values of the partition coefficients for PAS and its complexes, are positive, indicating that they are lipophilic. The influence of the metal on the flux and the permeability coefficient of the ligand through the Cerasome 9005 membrane shows that Zn(II) was able to improve the bioavailability of p-aminosalicylic acid with an enhancement ratio of 2. However, Cu(II) and Ni(II) do not have any effect on the absorption since the values of the diffusion flux as well as the permeability coefficient are close to those obtained when the metal was not incorporated into the system. The statistical value also indicates that there is no correlation between the two measured parameters since the correlation factor is very much less than 1.

The partition coefficients for PZA and its complexes are all below 0 and are considered low lipophilic. The permeability coefficient K_p for the ligand alone and those of its metal complexes were similar. The presence of the metal does not affect the flux and permeability coefficient of PZA. The statistical analysis indicates that there is no correlation between the logarithm of partition coefficient and permeability coefficient of PZA.

References:

1. H. H. Perkampus, *UV-Vis Spectroscopy and its Application* © Springer-Verlag Berlin Heidelberg, 1992.
2. R. S. Shah, R. R. Shah, R. B. Pawar and P. P. Gayakar, *Int. J. Pharmacy & Life Sci.*, 2015, **5**, 409-502.
3. A. P. B. Lever, *Inorganic Electronic Spectroscopy*, 2nd ed., Elsevier Amsterdam, 1984.
4. E. J. Billo, *J. Inorg. Nucl. Chem. Lett.*, 1974, **10**, 613-617.
5. L. M. Mirica, X. Ottenwaelder, T. D. P. Stack, *Chem. Rev.*, 2004, **104**, 1013-1045.
6. Z. Tyeklar, R. R. Jacobson, N. Wei, N. N. Murthy and K. D. Karlin, *J. Am. Chem. Soc.*, 1993, **115**, 2677-2689.
7. E. K. Efthimiadou, M. E. Katsarou, A. Karaliota and G. Psomas, *J. Inorg. Biochem.*, 2008, **102**, 910-920.
8. G. E. Jackson, *Uv-SPEC*, Private Communication, University of Cape Town.
9. H. Sigel and R. B. Martin, *Chem. Rev.*, 1982, **82**, 385-426.
10. V. K. Gupta, R. Prasad and A. Kumar, *Talanta*, 2003, **60**, 149-160.
11. Y. Inada, K. Ozutsumi, S. Funahashi, S. Soyama, T. Kawashima and M. Tanaka, *Inorg. Chem.*, 1993, **32**, 3010-3014.
12. A. T. Baker, *J. Chem. Edu.*, 1998, **75**, 98-99.
13. M. Mylonas, J. C. Plakatouras, N. Hadjiliadis, A. Krezel and W. Bal, *Inorg. Chim. Acta*, 2002, **339**, 60-70.
14. W. Bal, M. Dyba and H. Kozlowski, *Acta Biochim. Pol.*, 1997, **44**, 467-76.
15. A. Anichini, L. Fabbrizzi, P. Paoletti and R. M. Clay, *Inorg. Chim. Acta*, 1977, **24**, L21-L23.
16. R. G. Bhattacharyya, U. K. Paul, A. P. Chatterjee and S. P. Bag, *Indian J. Chem.*, 1990, **29A**, 986.

17. D. B. Powell and N. Sheppard, *Spectrochim. Acta.*, 1961, **17**, 68-76.
18. C. K. Jorgensen, *Acta Chem. Scand.*, 1954, **8**, 1502-1512.
19. J. G. Martins, P. Gameiro, M. T. Barros and H. M. Soares, *J. Chem. Eng. Data*, 2010, **55**, 3410-3417.
20. C. Conato, S. Ferrari, H. Kozłowski, F. Pulidori and M. Remelli, *Polyhedron*, 2001, **20**, 615-621.
21. M. E. Farago, J. M. James and V. C. G. Trew, *J. Chem. Soc. A*, 1968, 48-52.
22. M. E. Farago, J. M. James and V. C. G. Trew, *J. Chem. Soc. A*, 1967, 820-824
23. T. Komorita, J. Hidaka and Y. Shimura, *Bul. Chem. Soc. Jpn.*, 1971, **44**, 3353-3363.
24. M. Nonoyama and K. Yamasaki, *Inorganica Chim. Acta*, 1971, **5**, 124-128.
25. I. L. Lere, M. G. Beyene, R. K. Upadhyay, *Orient. J. Chem.*, 2013, **29**, 1111-1114.
26. T. Oza, *J. Cryst. Res. Technology*, 1988, **23**, 385-391.
27. P. G. Daniele, G. Ostacoli and O. Zerbinati, *Ann. Chim.*, 1990, **80**, 89.
28. T. S. Planka, B. Gyurcsik, N. V. Nagy, A. Rockenbauer, R. Sipos, J. Sima and M. Menlik, *J. Inorg. Biochem.*, 2008, **102**, 101-109.
29. M. J. Swarbrick and A. Cammarata, *Physical Pharmacy* 3rd ed., New Delhi. Lippincott. Williams and Wilkins, 2001, 3303.
30. Y. S. R. Krishnaiah, V. Satyanarana, and R. S. Karthikeyan, *J. Pharm. Sci.*, 2002, **5**, 124-130.
31. A. Hersey, A. P. Hill, R. M. Hyde and D. J. Livingstone, *Quant. Struct.-Act. Relat.*, 1989, **8**, 288-296.
32. C. Hansch and A. J. Leo. *Substituents Constants for Correlation Analysis in Chemistry and Biology*. Wiley-Interscience: New York, 1979.
33. J. Sangster, *Octanol-Water Partition Coefficient: Fundamentals and Physical Chemistry*, 1st ed., John Wiley & Sons Ltd, Chichester UK, 1997.

34. P. H. Stahl and C. G. Wermuth, Handbook of Pharmaceutical Salts: Properties, Selection and Use. Verlag Helvetica Chimica Acta: Wiley-VCH: Zurich, 2002.
35. Guidelines for Testing Chemicals, Section 1-Physical-Chemical Properties, 105. n-octanol/water partition coefficient; Organisation for Economic Cooperation and Development (OECD) Paris, 1981.
36. J. C. Dearden and G. M. Bresnen, *Quant. Struct.-Act. Relat.*, 1988, **7**, 133-144.
37. G. Klopman and H. Zhu, *Mini-Rev. Med. Chem.*, 2005, **5**, 127-133.
38. C. Y. Botte, F. Dubar, G. I. McFadden, E. Marechal and C. Biot, *Chem. Rev.*, 2012, **112**, 1269-1283.
39. A. Leo, C. Hansch and D. Elkins, *Chem. Rev.*, 1971, **71**, 525-616.
40. T. X. Xiang and B. D. Anderson, *J. Membrane Biol.*, 1994, **140**, 111-122.
41. J. N. Zvimba and G. E. Jackson, *J. Inorg. Biochem.*, 2007, **101**, 148-158.
42. ISO, *Tuberculosis (Edinburgh)*, 2008, **88**, 112-116.
43. S. B. Lakshminarayana, T. B. Huat, P. C. Ho, U. H. Manjunatha, V. Dartois, T. Dick and S. P. S. Rao, *J. Antimicrob. Chemother.*, 2015, **70**, 857-869.
44. N. Washington, G. Lamont, C. G. Wilson, C. Washington and R. Withington, *Int. J. Pharm.*, 1994, **108**, 125-131.
45. A. J. Hickey, Delivery System for Tuberculosis Prevention and Treatment. John Wiley & Sons, 2016.
46. C. Hansch, A. Leo and D. Hoekman, Exploring QSAR Hydrophobic, Electronic and Steric Constants. ACS. Washington, D.C. 1995.
47. S. G. Machatha and S. H. Yalkowsky, *Int. J. Pharm.*, 2005, **294**, 185-192.
48. M. Gaur, M. Dobke and V. L. Lunyak, *Int. J. Mol. Sci.*, 2017, **18**, 208-236.
49. V. A. Ziboh and R. S. Chapkin, Metabolism and Function of Skin Lipids (In Holman, ed.) Progress in lipid research, New York: Permagon, 1988, 27, 81-105.

50. G. T. Rich, R. I. Shaafi, T. C. Barton and A. K. Solomon, *J. General physiol.*, 1967, **50**, 2391-2405.
51. L. Smith, Penetrant Characteristics Influencing Skin Absorption. (In B. W. Kemppainen and W. Reifenrath, *Methods for Skin Absorption*. Florida: CRC Press, 1990, 23-33.
52. T. J. Franz, *J. Invest. Dermatol.* 1975, **64**, 190–195.
53. T. J. Franz, *Curr. Probl. Dermatol.* 1978, **7**, 58–68.
54. J. N. McDougal and M. F. Boeniger, *Crit. Rev. Toxicol.*, 2002, **32**, 291-327.
55. V. P. Shah, J. S. Elkins and R. L. Williams, Evaluation of the Test System Used for *In Vitro* Release of Drugs for Topical Dermatological Drug Products. *Pharm. Dev. Technol.*, 1999, **4**, 377–385.
56. C. T. Ueda, V. P. Shah, K. Derdzinski, G. Ewing, G. Flynn, H. Maibach, M. Marques, H. Rytting, S. Shaw, K. Thakker and A. Yacobi, *Pharmaceut. Forum*, 2009, **35**, 750–764.
57. J. Hadgraft and R. H. Guy, *Advances in Pharmaceutical Sciences*, Academic Press, London, 1992, 43-64.
58. M. Mugawara, Y. Takekuma, H. Yamada, M. Kobayashi, K. Iseki and K. Miyazaki, *J. Pharma. Sci.*, 1998, 960-966.
59. G. Camenisch, G. Folkers and H. Van de waterbeemd. *Int. J. Pharm.*, 1997, **147**, 61-70.
60. J. Zhang, M. Sun, A. Fan, Z. Wang and Y. Zhao, *Int. J. Pharm.*, 2013, **441**, 389-394.
61. G. Oliveira, J. Hadgraft and M. E. Lane, *Int. J. Cosmet. Sci.*, 2012, **34**, 536-545.
62. S. F. Ng, J. J. Rouse, F. D. Sanderson and G. M. Eccleston, *Arch. Pharm. Res.*, 2012, **35**, 579-593.
63. G. Ottaviani, S. Martel and P. A. Carrupt, *J. Med. Chem.*, 2006, **49**, 3948-3954.

64. S. Geinoz, S. Rey, G. Boss, A. L. Bunge, R. H. Guy, P. A. Carrupt, M. Teist, B. Testa, *Pharm. Res.*, 2002, **19**, 1622-1629.
65. Y. Maitani, K. Shimada and T. Nagai, *Chem. Pharm. Bull.*, 1996, **44**, 403-408.
66. S. Y. E. Hou and G. L. Flynn, *J. Pharm. Sci.*, 1997, **86**, 85-91.
67. K. R. Brain, K. A. Walters and A. C. Watkinson, Method for Studying Percutaneous Absorption. *In Dermatological and Transdermal Formulations*; K. A. Walters, Ed.; Marcel Dekker: New York, 2002, 197-269.
68. B. E. Vecchia and A. Bunge. Skin Adsorption Databases and Predictive Equations. *In Transdermal Drug Delivery*, R. H. Guy, J. Hadgraft, Eds; Marcel Dekker: New York, 2003, 57-141
69. M. E. Johnson, D. Blankstein and R. Langer, *J. Pharm Sci.*, 1997, **86**, 1162-1172.
70. Y. W. Choi and J. A. Rogers, *Pharm. Res.*, 1989, **6**, 399-403.
71. T. X. Xiang and B. D. Anderson, *J. Membr. Biol.*, 1994, **140**, 111-122.
72. N. J. Wheate, V. Vora, N. G. Anthony and F. J. McInnes, *J. Incl. Phenom. Macrocycl Chem.*, 2010, **68**, 359-367.
73. T. Caon, C. E. M. Campos, C. M. O. Simoes and M. A.S. Silva, *Int. J. Pharm.*, 2015, **494**, 463-479.
74. C. Zhu, L. Jiang, T. M. Chen and K. K. Hwang, *Eur. J. Med. Chem.*, 2002, **37**, 399-407.
75. T. T. Mariappan and S. Singh, *Clin. Res. Regul. Aff.*, 2008, **23**, 1-10.
76. B. Brodlin, B. Steffansen, C. U. Nielsen(Eds), *Molecular Biopharmaceutics: Aspect of Drug characterisation, Drug Delivery and dosage form Evaluation*, Published by Pharmaceutical Press, London 2010, 135-152.
77. C. Brusewitz, A. Schendler, A. Funke, T. Wagner, R. Lipp, *Int. J. Pharm.*, 2007, **329**, 173-181.
78. R. O. Potts, R. H. Guy, *Pharma. Res.*, 1992, **9**, 663-669.

79. Dermal Exposure Assessment: Principles and Applications, United States Environmental Protection Agency, EPA Interim Report, EPA/600/8-91/011B, January 1992.

Chapter 5

Solid-state studies

5.1 Introduction

This chapter presents an account of the attempted synthesis and characterisation of solid isoniazid (ISO) and pyrazinecarboxamide (PZA) metal complexes. As described in a previous chapter, the equilibria involving the formation of metal complexes of isoniazid, ethambutol (EMB) and p-aminosalicylic acid (PAS) in solution have been studied using glass electrode potentiometry (GEP), and structures have been proposed based on the model. The metal complexes of rifampicin and pyrazinecarboxamide could not be explored because the pK_a values were below the pH range of our studies. To confirm the models proposed for the Cu-complexes of ISO, EMB and PAS, UV-Visible spectroscopy was carried out.

The permeability and the lipophilicity characteristics of the ligands with Cu(II), Ni(II) and Zn(II) ions have also been studied in previous chapters. To establish the structures of the stable complexes, an attempt was made to synthesise and characterise the complexes in solid form for X-ray diffraction studies. Various methods were employed in the synthesis, including co-precipitation, recrystallization and mechanochemistry (both co-grinding and liquid-assisted grinding (LAG)). Mechanochemistry is the synthesis of chemical compounds using mechanical force.¹ It has been employed in organic synthesis and has provided a solvent-free path in reactions involving oxidation and reduction, as well as Wittig condensation and Suzuki Coupling.² Ondruschka and co-workers³ and Bolm and co-workers⁴ have proved that the solvent-free reactivity in mechanochemical synthesis in a planetary mill allows substantial improvement in energy efficiency, compared to a conventional solution-based or microwave-assisted synthesis. Mechanochemistry has also been used in the areas of molecular co-crystals and metal-organic materials. The LAG method has also been recognised as a highly efficient and rapid method for co-crystal screening. LAG uses a sub-stoichiometric amount of a liquid phase to enable, accelerate and template self-assembly reactions including solid, liquid or

gaseous reactants. The mechanochemical method is solvent-free and environmentally friendly. The products obtained in the present study through mechanochemistry were monitored using the PXRD technique. However, they were all found to be physical mixtures of the starting materials.

In an attempt to synthesise isoniazid and pyrazinecarboxamide (pyrazinamide) metal complexes via the solvothermal method, intriguing crystalline phases were obtained, quite different from those expected. The techniques listed below were used to characterise the crystal structures obtained.

5.2 Methodology

5.2.1 Elemental analysis

Elemental analysis experiments were performed on a Fisons EA1108 CHNS-O Elemental Analyzer to determine the percentage of carbon, hydrogen and nitrogen present in the samples. The results were used as a basis for interpreting Fourier electron density maps obtained from single crystal X-ray diffraction.

5.2.2 X-ray Diffraction

5.2.2.1 Single crystal X-ray diffraction

Excellent single crystals of selected complexes were prudently chosen to perform single crystal X-ray diffraction. Crystals were removed from their mother liquor and immediately covered with Paratone N oil (Exxon Chemical Co., TX, USA) to avoid loss of solvent molecules or decomposition. A single crystal was chosen under a microscope and attached to a nylon loop linked to a rigid mounting. Where single crystals were large, they were cut to obtain a suitable size. This was followed by mounting the nylon loop on the goniometer head under a cold stream of nitrogen gas. Single crystal data-collections were performed on a Bruker Kappa Apex II Duo

diffractometer using MoK α radiation ($\lambda = 0.71073 \text{ \AA}$). X-rays were produced by a Bruker K780 generator powered at 50 kV and 30 mA.

Data-collection was carried out at low temperature [173(2) K] using a Cryostream cooler (Oxford Cryosystems, UK) at a nitrogen vapour flow rate of $20 \text{ cm}^3 \text{ min}^{-1}$. Unit cell refinement and data reduction, including Lorentz-polarization corrections, were carried out using the program SAINT.⁵ The program SADABS⁶ was used to correct absorption effects on all intensity data.

For each structure, the space group was determined from systematic absences in the X-ray intensity data. The program XPREP⁷ was used to confirm the space group. This program prepares the input file which is then used for structure solution by direct methods using the SHELXS program.⁸ All non-hydrogen atoms were refined by full-matrix least-squares on F^2 with anisotropic thermal parameters using SHELXL-97⁸ within the X-Seed interface.⁹ All H atoms were initially located in difference electron density maps and were added to the model in idealised positions in a riding model with isotropic thermal parameters having values in the range 1.2-1.5 times those of their parent atoms. The program PovRay in the X-Seed interface was used to generate the figures.¹⁰

5.2.2.2 Powder X-ray diffraction (PXRD)

The experiments were performed on a Bruker D8 Advance diffractometer equipped with a Lynxeye detector using CuK α_1 -radiation ($\lambda = 1.5406 \text{ \AA}$) at 294 K (21 °C). Samples were ground into a fine powder after drying on a filter paper and placed on a zero-background sample holder and scanned over the 2θ range 4° to 40° with 0.015° increments. X-rays were generated by a current flow of 40 mA and an accelerating voltage of 30 kV. A receiving slit of 0.6 mm and primary and secondary slits of 2.5 mm were used.

5.3 Fourier transform infrared (FTIR) spectroscopy

When a complex can be isolated as a solid, vibrational spectroscopy, which includes IR can be used to identify the coordinating groups. IR gives detailed geometrical information from normal coordinate analysis of the data.¹¹ It uses an empirical analysis based on the comparison of structures of known metal-ligand complexes. Whenever stable complexes are prepared, it is standard practice to acquire an IR spectrum, since it is possible to determine the chelating groups by studying shifts of the ligand-based absorption peaks from their positions in the ligand itself. For example, metal-nitrogen bonding has been investigated in several diazepam complexes using FTIR spectroscopy.¹² IR studies were carried out on a Bruker Alpha spectrometer equipped with an ATR platinum Diamond reflectance accessory for solid samples. The samples were scanned over a range of 400-4500 cm^{-1} .

5.4. UV- Vis Spectroscopy

For each of the complexes whose structures were determined in this study, a 2×10^{-5} M solution was prepared in ethanol. The absorbances of these solutions were measured with a Hewlett Packard 8452A Diode Array spectrophotometer from 200 nm to 800 nm. A blank was used to correct the absorbance. The wavelength of maximum absorption was determined from the plot of absorbance against wavelength (nm).

5.5. Attempted synthesis of a Cu-isoniazid complex

5.5.1 Synthesis

In the synthesis 0.0137 g (1.0 mmol) of isoniazid (ISO, $\text{C}_6\text{H}_7\text{N}_3\text{O}$) was dissolved in 6 ml of ethanol-water (1:1 v/v) mixture and 0.0085 g (0.5 mmol) of $\text{CuCl}_2 \cdot \text{H}_2\text{O}$ was dissolved in 6 ml of water. The mixture of the two solutions was placed in a Teflon cup and heated in an autoclave at 100 °C for two days. The coloured solution was maintained at room temperature

for three days, and subsequently, blue crystals suitable for X-ray diffraction were filtered off. Elemental analysis yielded the following: C, 38.0%; H, 4.05%; N, 5.83%. From these data, it was not possible to arrive at a complex formula consistent with the above reactants. Further analytical techniques were carried out to ascertain the nature of the product. The synthesis was initially carried out in aqueous media to emulate the solution studies. Unfortunately, crystals were not obtained. This prompted the use of the alcoholic media employed in the synthesis.

5.5.1.1 X-ray data and structure determination

A blue crystal of dimensions $0.020 \times 0.070 \times 0.140$ mm was mounted on a nylon cryoloop in a random orientation. The determination of the unit cell and data-collection were performed on a Bruker Kappa Apex II Duo diffractometer using graphite-monochromated MoK α radiation ($\lambda = 0.71073$ Å). 1673 independent reflections ($R_{\text{int}} = 0.061$) were obtained after merging all the intensity data collected at 173 K. Analysis revealed that the compound belongs to the triclinic system, space group $P \bar{1}$. The structure was solved by direct methods using the SHELXS program. Instead of the expected presence of the isoniazid molecule in the complex, the metal ion was found to be coordinated to isonicotinate ions, thus indicating that the original drug had been hydrolysed during complex synthesis. (The details of the chemical transformation accompanying the synthesis are discussed in a subsequent section). Phenyl H atoms were placed in idealised positions but H atoms of water molecules were allowed to refine freely. The refinement converged with $R_1 = 0.0469$, $wR_2 = 0.1175$. A full listing of the crystal data and refinement details appears in Table 1. On comparing these data with Cu(II) structures deposited in the Cambridge Structural Database (CSD),¹³ they were found to be very similar to those reported previously for the hydrated copper(II)isonicotinate complex $\text{Cu}(\text{ISONIC})_2(\text{H}_2\text{O})_4$.¹⁴

Table 5.1: Crystal data and details of refinement.

Compound	Cu(ISONIC) ₂ (H ₂ O) ₄	Cu(ISONIC) ₂ (H ₂ O) ₄ Previously reported ¹⁴
Formula	C ₁₂ H ₁₆ CuN ₂ O ₈	C ₁₂ H ₁₆ CuN ₂ O ₈
Molecular weight (g mol⁻¹)	379.82	379.82
Crystal system	Triclinic	Triclinic
Space group	P $\bar{1}$ (No. 2)	P $\bar{1}$
a (Å)	6.3124(15)	6.3334(3) ^a
b (Å)	6.8226(15)	6.8871(3)
c (Å)	9.1702(19)	9.1807(4)
α (°)	99.111(4)	99.433(4)
β (°)	105.144(4)	105.190(4)
γ (°)	108.558(4)	108.213(4)
V (Å³)	348.58(13)	353.7(1)
Z	1	1
No. of reflections collected	1673	1528
Calculated density (g cm⁻³)	1.809	1.783
μ(MoKα) [mm⁻¹]	1.614	1.590
F(000)	195	195
Temperature (K)	173	298
Crystal size (mm)	0.020 × 0.070 × 0.140	0.3 × 0.5 × 0.1
X-ray wavelength (Å)	Mo K α (0.71073)	0.71069
Θ-range (°)	2.4, 28.0	- ^b
Dataset	-8: 8; -8: 9; -12:12	±8, ±7, +11
Total, Unique data, R(int)	7370, 1673, 0.061	1528, 1358, -
Observed data [I > 2σ(I)]	1477	-
N_{ref}, N_{par}	1673, 122	1358, 138
R₁, wR₂, S	0.0469, 0.1175, 1.05	0.0350, 0.052, -
(Δ/σ)_{mean}	< 0.001	-
($\Delta\rho$)_{min, max} (eÅ⁻³)	-1.02, 1.16	-, -

^aThe order in which the unit cell parameters were originally reported was different

^bThe dash (-) in column three indicates that the corresponding parameter was not explicitly reported in the paper

The crystal data and details of refinement reported in the literature¹⁴ refer to a temperature of 298 K, whereas the data reported in the present structure re-determination were collected at a lower temperature of 173K. The molecular structure is depicted in Figure 5.1.

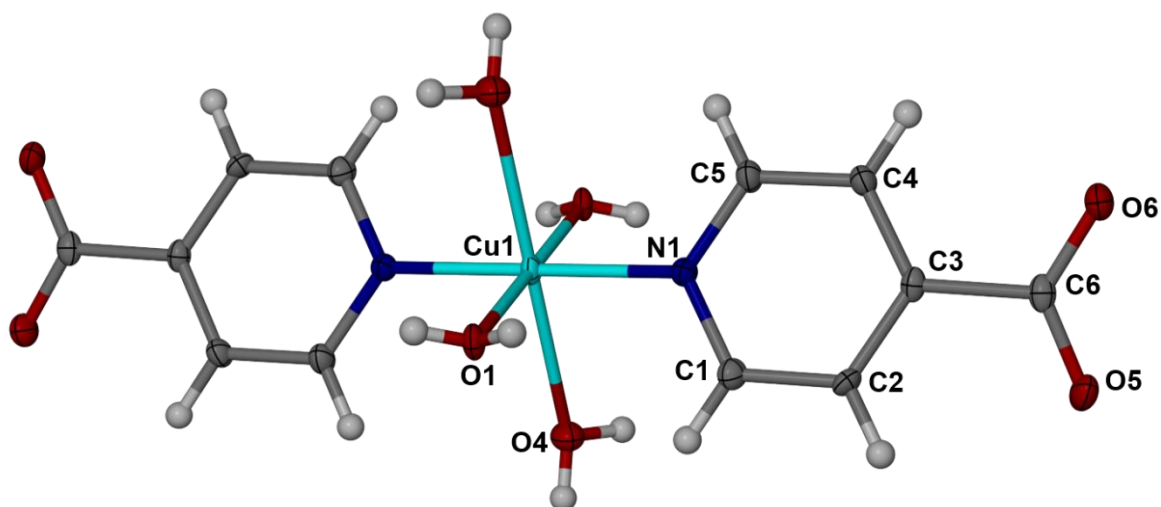


Figure 5.1: The molecular structure of $\text{Cu}(\text{ISONIC})_2(\text{H}_2\text{O})_4$ with atomic labelling and thermal ellipsoids of the non-H atoms drawn at the 50% probability level.

The coordination environment shows that the Cu(II) ion coordinates with two isonicotinate ligands and four water molecules resulting in a distorted octahedral configuration of CuN_2O_4 type. The isonicotinate ions and water molecules both act as monodentate ligands via the pyridine nitrogen and the oxygen atoms respectively. The Cu atom is located on a centre of inversion.

The bond distances obtained from PLATON¹⁵ for Cu-O1 and Cu1-O4 are 1.984(3) Å and 2.426(3) Å respectively. Hence, the coordination around the Cu(II) atom shows an axially-elongated octahedral geometry with Jahn-Teller distortion. The Cu1-O4 bond distance lies in the range (2.275-2.520 Å) reported for Cu(II) complexes with Jahn-Teller distortion, and the equatorial bond distance (Cu1-O1) is slightly longer than those reported for six-coordinated Cu(II) complexes with water molecules (1.950-1.973 Å).¹⁴ The Cu-N distance (1.989(2) Å) is shorter than those reported for six-coordinated Cu(II) complexes with pyridine ligands (2.039-2.055 Å).¹³⁻¹⁴ Selected bond lengths and angles are summarised in Table 5.2.

Table 5.2: Selected bond lengths (Å) and angles (°) for Cu(ISONIC)₂(H₂O)₄.

Bond lengths (Å)		Bond Angles (°)		Bond Angles (°)	
Cu1 – O1	1.984(3)	O1 – Cu1 – O4	93.0(1)	C2 – C3 – C4	120.3(2)
Cu1 – O4	2.426(3)	O1 – Cu1 – O4 ⁱ	86.1(1)	C2 – C3 – C6	119.5(2)
Cu1 – N1	1.989(2)	N1 – Cu1 – O1	90.4(1)	C4 – C3 – C6	120.2(3)
N1 – C1	1.391(3)	O1 – Cu1 – N1	89.6(1)	C3 – C4 – C5	119.4(2)
N1 – C5	1.392(4)	O4 – Cu1 – N1	88.8(1)	N1 – C5 – C4	120.8(2)
C1 – C2	1.395(3)	Cu1 – N1 – C1	118.9(2)	O5 – C6 – C3	116.1(3)
C2 – C3	1.392(4)	Cu1 – N1 – C5	121.9(2)	O5 – C6 – O6	125.8(3)
C3 – C4	1.393(3)	N1 – C1 – C2	120.7(2)	O6 – C6 – C3	118.1(3)
C4 – C5	1.397(3)	C1 – C2 – C3	119.6(2)		
O5 – C6	1.258(5)				
O6 – C6	1.252(5)				

The six atoms form an octahedral array around the copper ion, the angle O1-Cu1- O1ⁱ (i = 1 - x, 1 - y, 1 - z) is 180° due to centrosymmetry and O1-Cu-N1 is 89.6(1)° (Table 5.2). All water H atoms engage in intermolecular hydrogen bonding (Table 3). The O-H...O hydrogen bonds are crucial and contribute to the stability of the crystal structure.

Table 5.3: Hydrogen bond data (distances in Å, angles in degrees) for Cu(ISONIC)₂(H₂O)₄.

D-H...A	d(D-H)	d(H...A)	d(D...A)	∠ (DHA)
O4-H3...O6 ^{iv}	0.88(6)	2.04(6)	2.896(4)	167(5)
O4-H6...O5 ⁱⁱⁱ	0.78(6)	2.06(6)	2.825(5)	167(5)
O1-H7...O5 ⁱⁱ	0.72(6)	1.90(6)	2.615(4)	178(11)
O1-H8...O6 ⁱ	0.77(5)	1.98(5)	2.736(4)	168(6)
C1-H1...O4	0.95	2.60	3.068(4)	111
C5-H5...O1 ^v	0.95	2.48	3.352(4)	154

Symmetry operations: (i) 1 - x, 1 - y, 1 - z; (ii) -1 + x, y, -1 + z; (iii) -x, -y, 1 - z; (iv) 1 - x, -y, 1 - z; (v) 1 + x, y, z

A packing diagram of Cu(ISONIC)₂(H₂O)₄ is shown in Figure 5.2. The oxygen atoms of the carboxylate groups are acceptors of intermolecular hydrogen bonds from the coordinated water molecules of the neighbouring [Cu(ISONIC)₂(H₂O)₄] molecules to form three-dimensional supramolecular complexes. As shown in Figure 5.2, molecules are interconnected in the solid

state by five crystallographically unique intermolecular hydrogen bonds, generating a final three-dimensional supramolecular network.

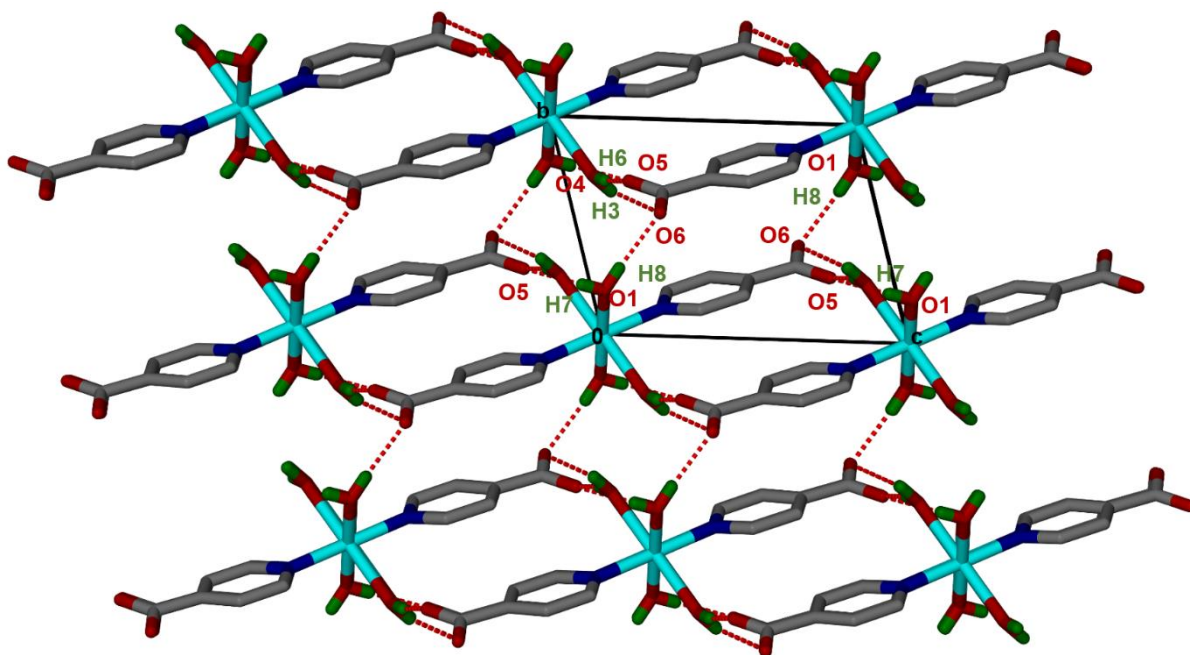


Figure 5.2: Packing diagram illustrating principal H-bonds in $\text{Cu}(\text{ISONIC})_2(\text{H}_2\text{O})_4$.

5.5.1.2 PXRD Data

To further confirm that the complex isolated in the present study was the same phase as that reported previously, the experimental PXRD pattern of the former was compared with that calculated from the single crystal X-ray data reported for $\text{Cu}(\text{ISONIC})_2(\text{H}_2\text{O})_4$.¹⁴ These powder patterns (Figure 5.3) are very similar, with corresponding peaks observed at 2θ values 10.2, 15.2, 16.9, 18.9, 19.7, 23.3, 26.8 and 27.8° , thus revealing that these represent the same crystal phase and therefore supporting the inference from the single crystal X-ray diffraction study that during complex synthesis the isoniazid component had been chemically transformed to the isonicotinate ion.

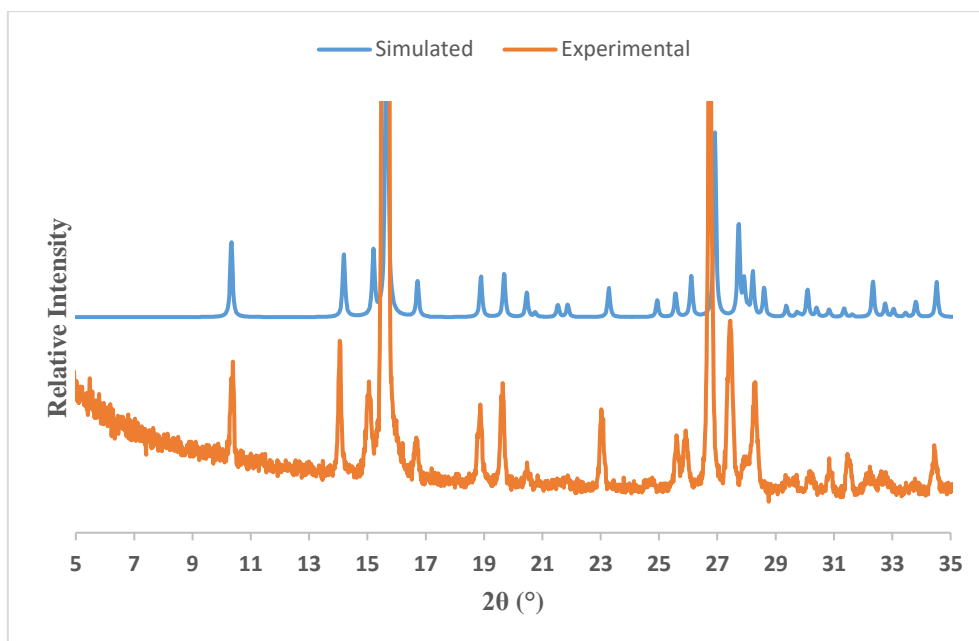


Figure 5.3: Experimental PXRD trace for the complex isolated in the present study and the simulated PXRD trace for $\text{Cu(ISONIC)}_2(\text{H}_2\text{O})_4$.¹⁴ The abnormally high intensity of the peak at 15.2° in the experimental trace is attributed to preferred orientation of crystallites in the sample. Small differences in peak angular positions are due to the different temperatures of the two analyses.

5.5.1.3. Infrared Spectral Data

The IR spectrum of the compound (Figure 5.4) was recorded using a Bruker Alpha spectrometer equipped with an ATR Platinum Diamond reflectance accessory for solid samples. Samples were scanned over a range of $400\text{--}4000\text{ cm}^{-1}$ and the results are presented in Table 5.4.

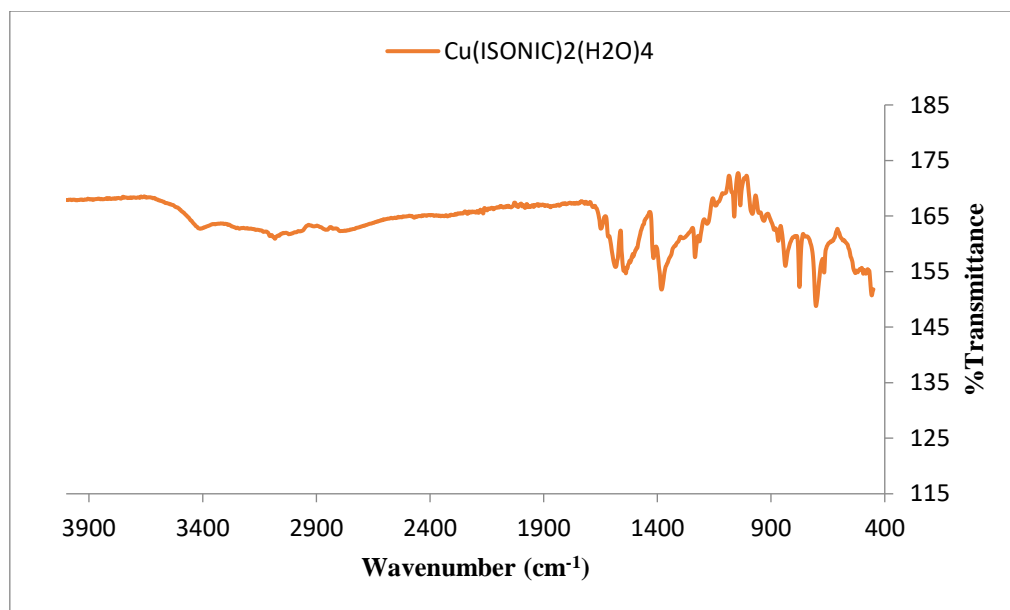


Figure 5.4: The IR spectrum of $\text{Cu(ISONIC)}_2(\text{H}_2\text{O})_4$.

The frequencies and assignments of spectral bands for ISONIC and its copper complex are shown in Table 5.4. The carboxylate stretching vibration in $\text{Cu(ISONIC)}_2(\text{H}_2\text{O})_4$ is dependent on the coordination mode to the copper(II) ion.¹⁶

Table 5.4: The frequencies (in cm^{-1}) and assignments of vibrations of ISONIC and its complex.

Isonicotinate ion in sodium isonicotinate ¹⁶	$\text{Cu(ISONIC)}_2(\text{H}_2\text{O})_4$	Assignments
-	3410(br)	$\nu(\text{OH})$
3070(vw)	3082(w)	$\nu(\text{CH})_{\text{ar}}$
1584(w)	1585(w)	$\nu(\text{C}=\text{C})_{\text{ar}}$
1534(s)	1538(s)	$\nu_{\text{as}}(\text{COO}^-)$
1410(s)	1383(s)	$\nu_{\text{s}}(\text{COO}^-)$
1217(w)	1235(s)	$\nu(\text{C}-\text{O}) + \delta(\text{OH})$
1058(w)	1061(w)	$\delta(\text{CCH})$
848(s)	-	$\beta(\text{COO}^-)_{\text{s}}$
764(s)	775(s)	$\gamma(\text{CCH})_{\text{ar}}$
679(s)	702(s)	$\delta(\text{COO}^-)$
-	667	$\nu(\text{Cu}-\text{O})$
124	155	$\Delta(\nu_{\text{as}}-\nu_{\text{s}})$

The broad band at 3410 cm^{-1} may be attributed to $\nu(\text{OH})$ absorption in H_2O molecules. The Cu–O stretching frequency is observed at 667 cm^{-1} in the complex and agrees with the observations of former workers.¹⁷

5.4. Attempted synthesis of a Cu – pyrazinecarboxamide complex

5.4.1. Synthesis

A mass of 0.0369 g (1.0 mmol) of pyrazinecarboxamide (PZA, C₅H₅N₃O) was dissolved in 5 ml of methanol and 0.0256 g (0.5 mmol) CuCl₂.H₂O was dissolved in 3 ml of ethanol. The mixture of the two solutions was placed in a Teflon cup and heated in an autoclave at 100 °C for two days. Elemental analysis of the resulting crystals indicated C₁₀H₆CuN₄O₄ as the formula of the compound (Anal. Calc. C₁₀H₆CuN₄O₄: C: 38.8%; H, 2.0%; N, 18.1%. Found C, 37.33%; H, 1.90%; N, 18.13%). It is evident from the data above that during the synthesis a complex with a different number of nitrogen atoms from that expected based on the formula of PZA resulted. Further analytical techniques were carried out to ascertain the nature of the complex. Details of X-ray data-collection and structure refinement of the complex are shown in Table 5.5. A blue crystal of dimensions 0.08 × 0.09 × 0.11 mm was mounted on a nylon cryoloop which was placed on the goniometer head under a cold stream of nitrogen gas. Analysis of the structure revealed that the complex belongs to the monoclinic system with space group P2₁/c. X-ray structure determination revealed that the product was in fact catena-[bis(μ₂-pyrazine-2-carboxylato)-copper(II)], with codename Cu(PZONIC)₂ where PZONIC is the 2-pyrazine carboxylate ion, instead of the expected Cu-pyrazinecarboxamide complex. The mechanism for the formation of this unexpected product is discussed later. It was subsequently discovered that the crystal structure of the same crystalline phase had been reported previously in the Cambridge Structural Database (CSD) with refcode BEYPUQ02,¹⁷⁻¹⁸ intensity data having been collected at 283-303 K, while in the present study the crystal was analysed at 173(2) K.

Table 5.5: Crystal data and details of refinement.

Compound	Cu(PZONIC)₂	Cu(PZONIC)₂ Previously reported ¹⁸
Formula	C ₁₀ H ₆ N ₄ O ₄ Cu	C ₁₀ H ₆ N ₄ O ₄ Cu
Molecular weight (g mol⁻¹)	309.7	309
Crystal system	Monoclinic	Monoclinic
Space group	P2 ₁ /c	P2 ₁ /c
a (Å)	5.024(6)	5.034(4)
b (Å)	15.309(2)	15.332(13)
c (Å)	7.020(1)	7.0720(6)
α (°)	90	90
β (°)	106.188(3)	106.6250(10)
γ (°)	90	90
V (Å³)	518.62(1)	523.49(8)
Z	2	2
No. of reflections collected	1302	2928
Calculated density (g cm⁻³)	1.984	1.965
μ(MoKα) [mm⁻¹]	2.124	-
F(000)	310	310
Temperature (K)	173(2)	291(2)
Crystal dimensions (mm)	0.08 × 0.09 × 0.11	0.12 × 0.10 × 0.08
X-ray wavelength (Å)	MoKα (0.71073 Å)	(0.71073 Å)
Θ -range (°)	2.7, 28.4	-
Dataset	-6: 6; -20: 20; -9: 9	-
Total., Unique data, R(int)	11494, 1302, 0.056	-
Observed data [I>2σ(I)]	1078	-
N_{ref}, N_{par}	1302, 88	-
R₁, wR₂, S	0.0305, 0.0821, 1.05	0.0214, 0.0678, 1.020
(Δ /σ)_{mean}	< 0.001	-
Δρ_{min, max} (eÅ⁻³)	-0.48, 0.38	-

The dash (-) in column three indicates that the corresponding parameter was not explicitly reported in the paper

The molecular structure of Cu(PZONIC)₂, the coordination environments around Cu(II) centres and the atom labelling of the complex are shown in Figure 5.5. The complex displayed a square-planar geometry, with the ligand acting in a bidentate mode. Metal ion coordination is effected via the pyrazine nitrogen atoms and carboxylate oxygen atoms of the pyrazine carboxylate

resulting in the formation of five-membered chelate rings. The Cu(II) ion is located on a centre of inversion.

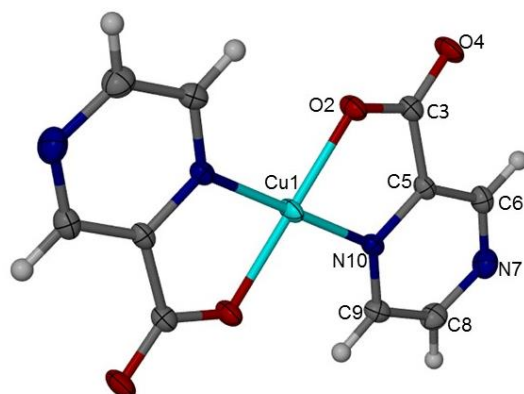


Figure 5.5: The molecular structure of $\text{Cu}(\text{PZONIC})_2$ with atomic labelling and thermal ellipsoids of the non-H atoms drawn at the 50% probability level.

The largest single contribution to the distortion from square-planar geometry is shown by the O2-Cu-N10 angle ($83.80(7)^\circ$), resulting from the formation of the five-membered ring required at the metal atom by the bidentate ligand.

The coordination geometry at the metal centre is in fact distorted octahedral, and the structure is polymeric, as shown in Figure 5.6. Selected bond lengths and angles are listed in Table 5.6.

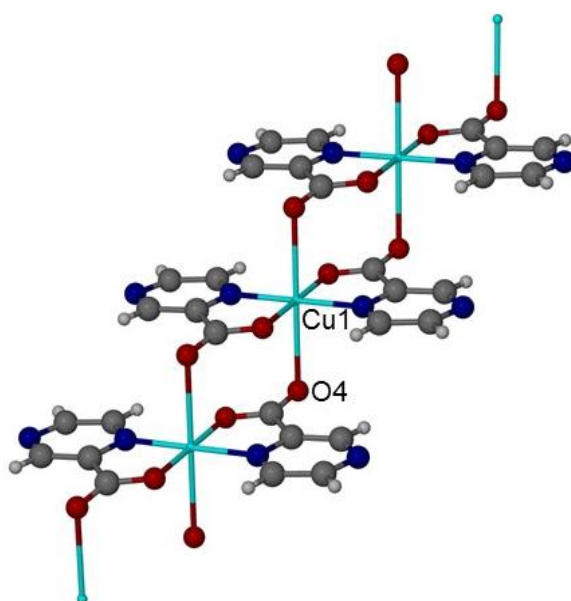


Figure 5.6: A short segment of a polymeric unit of $\text{Cu}(\text{PZONIC})_2$.

The copper ion in Cu(PZONIC)₂ is hexa-coordinate. The axial coordination is due to the weak coordination of the copper ion with a carboxylate oxygen atom of the neighbouring molecule, thus forming a distorted-octahedral coordination sphere. The Cu1–O4 coordination distance of 2.703(2) Å is considerably longer than the usual carboxylate oxygen to copper distance of 1.94(1) Å.¹⁹ The coordination distances Cu1–N10 and Cu1–O2 (1.977(2) and 1.935(2) Å) are comparable with those reported for Cu(II) complexes.²⁰⁻²²

Table 5.6: Selected bond lengths (Å) and angles (°) for Cu(PZONIC)₂.

Bond lengths (Å)		Bond Angles (°)		Bond Angles (°)	
Cu1 – O2	1.935(2)	O2 – Cu1 – N10	83.80(7)	Cu1 – O2 – C3	114.9(2)
Cu1 – O4	2.703(2)	O2 – Cu1 – O4 ⁽ⁱ⁾	92.47(6)	C3 – O4 – Cu1	101.5(2)
Cu1 – N10	1.977(2)	O4 – Cu1 – O2 ⁽ⁱⁱ⁾	87.53(6)	O2 – C3 – C5	114.7(2)
N7 – C6	1.333(3)	O4 – Cu1 – N10	87.68(7)	O4 – C3 – C5	119.6(2)
N7 – C8	1.333(4)	N10 – Cu1 – O4	92.32(7)	O2 – C3 – O4	125.6(2)
N10 – C5	1.340(3)	N10 – Cu1 – O2	96.20(7)	N7 – C6 – C5	121.6(2)
N10 – C9	1.336(3)	C6 – N7 – C8	116.8(2)	N10 – C5 – C3	114.9(2)
O2 – C3	1.283(3)	C5 – N10 – C9	118.6(2)	N7 – C8 – C9	122.8(2)
O4 – C3	1.226(3)	Cu1 – N10 – C5	111.3(2)	N10 – C9 – C8	119.4(2)
C5 – C6	1.386(3)	Cu1 – N10 – C9	130.1(2)		

Symmetry operations: (i) -1+ x, y, z; (ii) - x, 1- y, 1- z

The average conjugated C–C bond distance 1.386(3) Å and the average C–N bond distance 1.333(3) Å compare favourably with the respective known literature values²³ (1.396 and 1.334 Å) while the average endocyclic N–C–C angle, 121.6(2)°, is similar to the value 122.4(1)° previously reported for pyrazine carboxylic acid in the literature.²⁴ The partial packing diagram illustrating principal H-bonds (C–H...O, C–H...N) in Cu(PZONIC)₂ is shown in Figure 5.7.

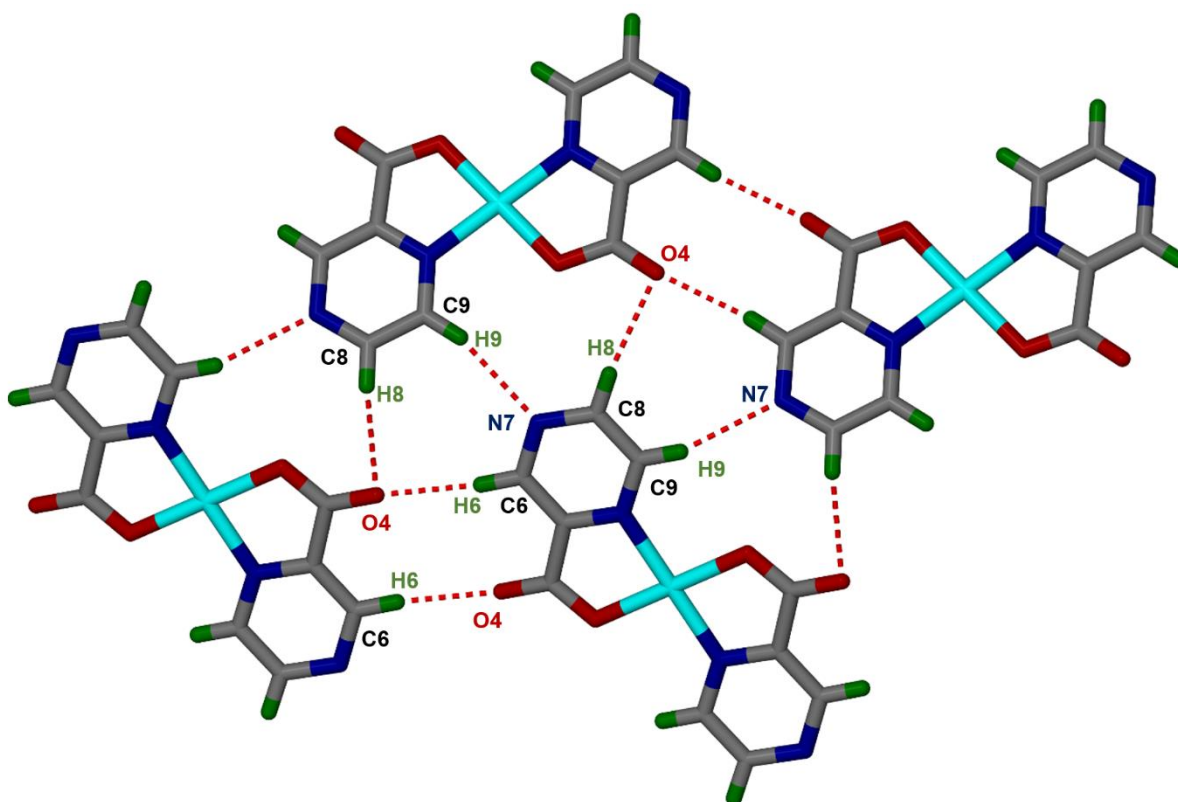


Figure 5.7: Layer formation based on hydrogen bonds (C–H...O, C–H...N) in Cu(PZONIC)₂.

The hydrogen bond lengths and angles for the compound are shown in Table 5.7.

Table 5.7: Hydrogen bond data (distances in Å, angles in degrees).

D–H...A	d(D–H)	d(H...A)	d(D...A)	∠(DHA)
C6–H6...O4 ⁱ	0.95	2.32	3.259(3)	168
C8–H8...O4 ⁱⁱ	0.95	2.50	3.388(3)	155
C9–H9...N7 ⁱⁱⁱ	0.95	2.54	3.458(3)	161

Symmetry operations: (i) 2 - x, 1 - y, 2 - z; (ii) 1 - x, -1/2 + y, 3/2 - z; (iii) -1 + x, 1/2 - y, -1/2 + z

5.4.1.2 PXRD Data

Figure 5.8 shows the PXRD pattern obtained from the experimental sample prepared in the present study and the calculated pattern of the complex structure reported in the literature.¹⁷

There are some intensity differences that can be attributed to preferred orientation effects in the experimental sample, but the otherwise high level of agreement between the two traces is convincing evidence of the identity of the two phases.

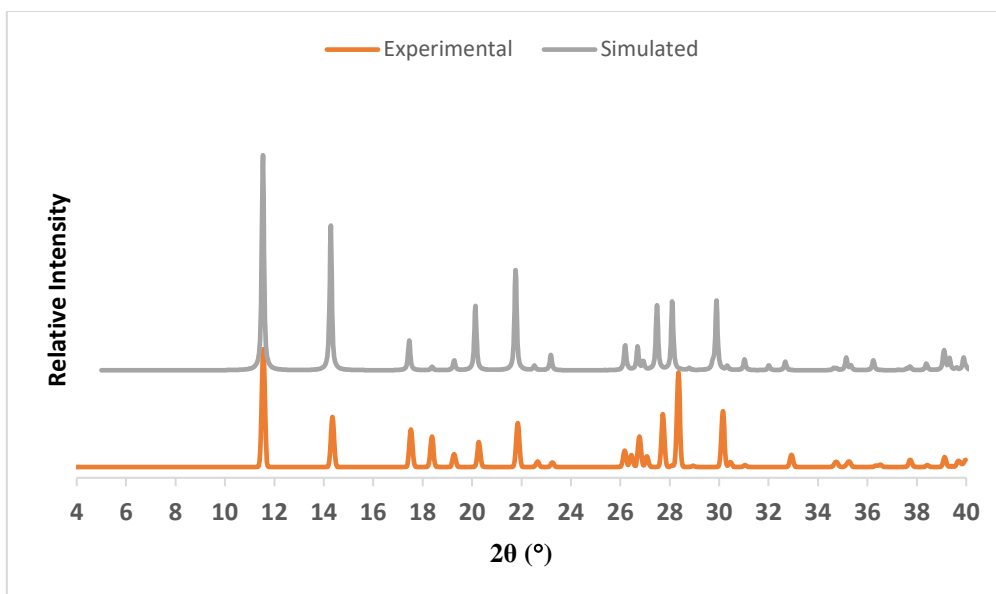


Figure 5.8: Experimental PXRD trace for the complex isolated in the present study and the simulated PXRD trace for Cu(PZONIC)_2 .¹⁸

5.4.2 Infrared Spectral Data

Fourier transform infrared (FTIR) spectroscopy was conducted to determine whether the spectral observations were consistent with the crystal structure. A shift of a band to a lower wavelength is anticipated if the carboxylate functional group is coordinated to the metal. The IR spectrum and the frequencies as well as the band assignments for Cu(PZONIC)_2 are shown in Figure 5.9 and Table 5.8 respectively.

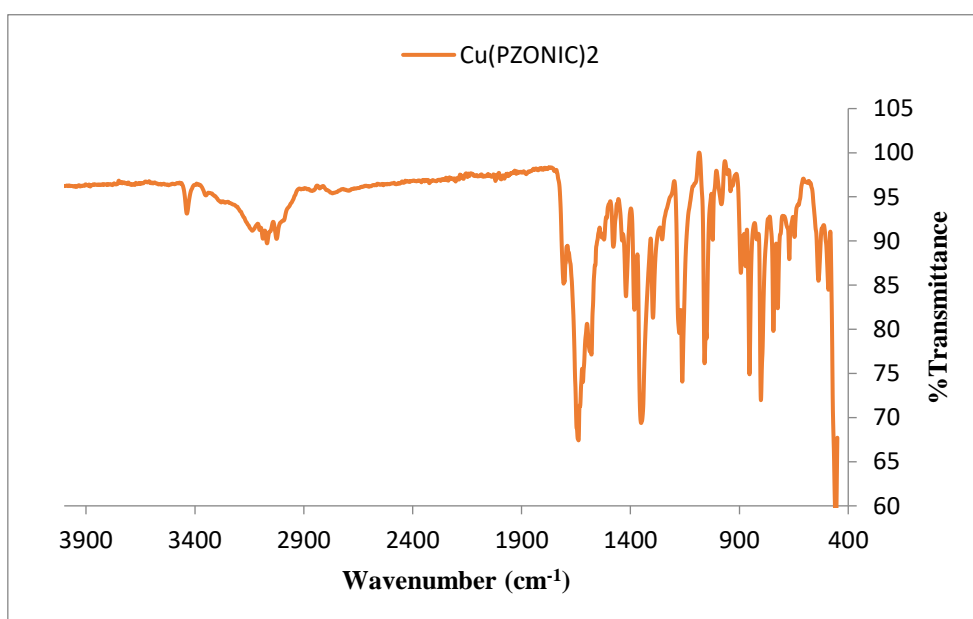


Figure 5.9: The IR spectrum of Cu(PZONIC)_2 .

Table 5.8: The frequencies (cm^{-1}) and assignments of bands in the FTIR spectra of PZONIC and Cu(PZONIC)_2 .

Pyrazinoate ion (PZONIC) in $[\text{Ni(PZONIC)}_2(\text{H}_2\text{O})_2]^{25}$	Cu(PZONIC)_2	Assignment
1585(s)	1581	$\nu(\text{C}=\text{N})$
1660(s)	1642	$\nu(\text{C}=\text{O})$
1290(s)	1297	$\nu(\text{C}-\text{O})$
-	454	$\nu(\text{Cu}-\text{O})$
-	537	$\nu(\text{Cu}-\text{N})$

For the Cu(PZONIC)_2 the sharp band centred at approximately 1581 cm^{-1} can be ascribed to $\nu(\text{C}=\text{N})$. The bands at 1642 cm^{-1} and 1297 cm^{-1} are assigned to $\nu(\text{C}=\text{O})$ and $\nu(\text{C}-\text{O})$ respectively, which are consistent with monodentate carboxylate coordination. The presence of a sharp band at 537 cm^{-1} also confirms the assignment of the $\nu(\text{Cu}-\text{N})$ mode.²⁶

5.4.3 UV-Visible spectroscopy

The UV-spectrum of Cu(PZONIC)_2 in ethanolic solution is shown in Figure 5.10. The spectrum displays bands between 200 and 350 nm. The band at 270 nm is ascribed to the $\pi \rightarrow \pi^*$ transition and the peak at 328 nm is ascribed to the $n \rightarrow \pi^*$ transition of the pyrazine ligand.²⁷

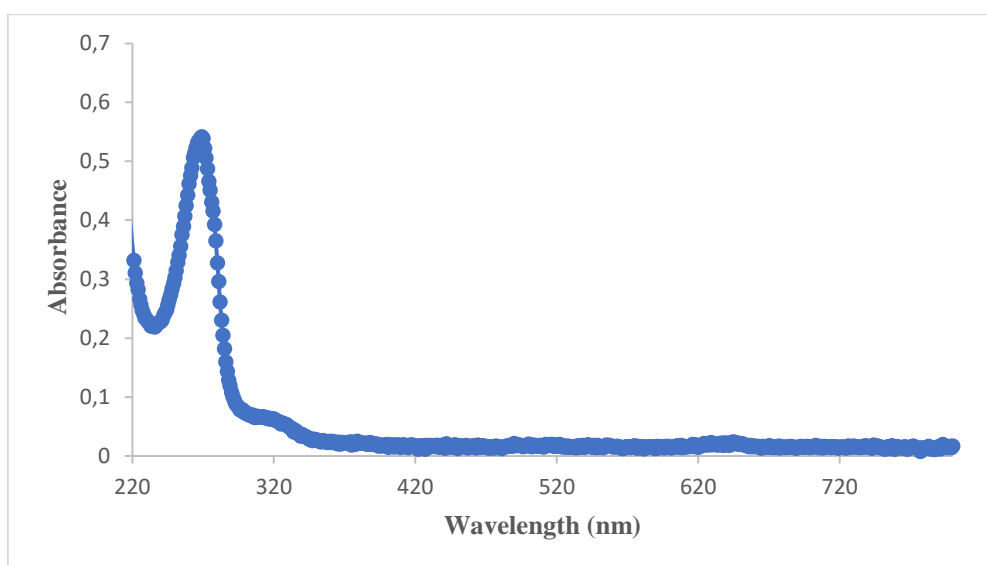


Figure 5.10: UV-Visible spectrum for Cu(PZONIC)_2 in ethanol.

5.5 Attempted Synthesis of Ni²⁺ and Zn²⁺-Pyrazinecarboxamide Complexes.

Due to the demand on the chemical industry to manage the global problem of pollution and the growing energy crisis, there is a need to develop preparative processes that are less expensive and more environmentally friendly. The process of co-grinding reactants using a mortar and pestle provided a solvent-free and hence more 'green' technique for attempted metal complex formation. A mass of 0.0369 g (1.0 mmol) of pyrazine-carboxamide (PZA) was weighed, and the following amounts of the metal salts were weighed: 0.0275 g (0.5 mmol) Zn(CH₃COO)₂ and 0.0265 g (0.5 mmol) Ni(CH₃COO)₂. The PZA and each of the metal salts were co-ground without solvent addition using a mortar and pestle for 4 min, after which the PXRD pattern of the product was monitored. Further sampling and PXRD recording were performed after consecutive periods of 10 min and 20 min to ensure that any reaction that might have occurred had reached completion. The same experiments were performed using the liquid-assisted grinding (LAG) technique with ethanol as solvent, followed by recording of product PXRD traces. However, all products were found to be physical mixtures of the starting materials. The solvothermal method was therefore used in an attempt to form the desired complexes, as described below.

A mass of 0.0369 g (1.0 mmol) of pyrazinecarboxamide was weighed and dissolved in 5 ml of methanol. Two separate 3 ml ethanolic solutions containing respectively 0.0275 g (0.5 mmol) Zn(CH₃COO)₂ and 0.0265 g (0.5 mmol) Ni(CH₃COO)₂ were prepared. The PZA solution was mixed with each of the metal salt solutions and the two resulting solutions were placed in Teflon cups and heated in an autoclave at 100 °C for two days. Crystals were formed and analysed. Elemental analysis data for the complexes are shown in Table 5.9.

Table 5.9: Elemental analysis data for the attempted synthesis of Ni²⁺ and Zn²⁺-pyrazine-carboxamide complexes.

Complexes	Calculated %			Experimental %		
	C	H	N	C	H	N
C ₁₀ H ₁₀ N ₄ O ₆ Ni	35.22	2.94	16.43	35.05	2.75	16.18
C ₁₀ H ₁₀ N ₄ O ₆ Zn	34.54	2.87	16.10	34.49	2.76	16.09

During the synthesis, complexes with a different number of nitrogen atoms from that expected based on the formula of PZA resulted. Thus, other analytical techniques were carried out to establish the nature of the complexes. From single crystals of each of the above complexes, the respective unit cell parameters were measured on the diffractometer and compared with those found for complexes listed in the Cambridge Structural Database (CSD) having similar unit cell parameters. The latter complexes turned out to be the same metal complexes as those reported in the present study, namely diaqua-bis(2-pyrazinecarboxylato)-M(II) complexes, where M = Ni and Zn. The comparative data are listed in Table 5.10. It should be noted that the unit cell parameter estimates for the compounds of the present study were determined and refined using a limited number of CCD detector frames only since full X-ray data-collections were not intended, whereas unit cell data for the compounds cited from the literature are more accurate, but span a large temperature range. Despite these different conditions, the level of agreement confirms that the respective crystalline phases reported in this study and those listed in the CSD are the same. Furthermore, this series of metal complexes appears to be isostructural from the near equality of the corresponding unit cell parameters, common space group and Z value.

Since pyrazinecarboxamide (PZA) was employed in the attempted solvothermal syntheses of the present study and the products in fact contain the 2-pyrazinecarboxylato ligand, it is evident that an undesired chemical transformation had occurred. As described earlier in this chapter,

the analogous transformation occurred when the solvothermal synthesis of the copper complex of PZA was attempted.

Table 5.10: Comparative crystal data for M(PZONIC)₂(H₂O)₂ complexes.

Compound	Ni(PZONIC) ₂ (H ₂ O) ₂ Present study	Ni(PZONIC) ₂ (H ₂ O) ₂ ²⁸	Zn(PZONIC) ₂ (H ₂ O) ₂ Present study	Zn(PZONIC) ₂ (H ₂ O) ₂ ²⁹
Formula	C ₁₀ H ₁₀ N ₄ O ₆ Ni	C ₁₀ H ₁₀ N ₄ O ₆ Ni	C ₁₀ H ₁₀ N ₄ O ₆ Zn	C ₁₀ H ₁₀ N ₄ O ₆ Zn
Molecular weight (g mol⁻¹)	340.93	340.93	347.38	347.38
Crystal system	Monoclinic	Monoclinic	Monoclinic	Monoclinic
Space group	P2 ₁ /c	P2 ₁ /c	P2 ₁ /c	P2 ₁ /c
a (Å)	5.302	5.250(1)	5.155	5.2516(1)
b (Å)	11.032	10.992(1)	10.998	11.1098(3)
c (Å)	10.346	10.285(1)	10.137	10.2151(3)
α (°)	90.00	90.00	90.00	90.00
β (°)	99.00	99.80	99.00	99.817(1)
γ (°)	90.00	90.00	90.00	90.00
V(Å³)	597.70	584.894	567.64	587.265(3)
Z	2	2	2	2
Temperature (K)	173(2)	283-303	173(2)	153(2)

5.5.1 Infrared Spectral Data

The infrared spectra and the assignments based on the frequencies for the above complexes of PZONIC are shown in Figure 5.11 and Table 5.11.

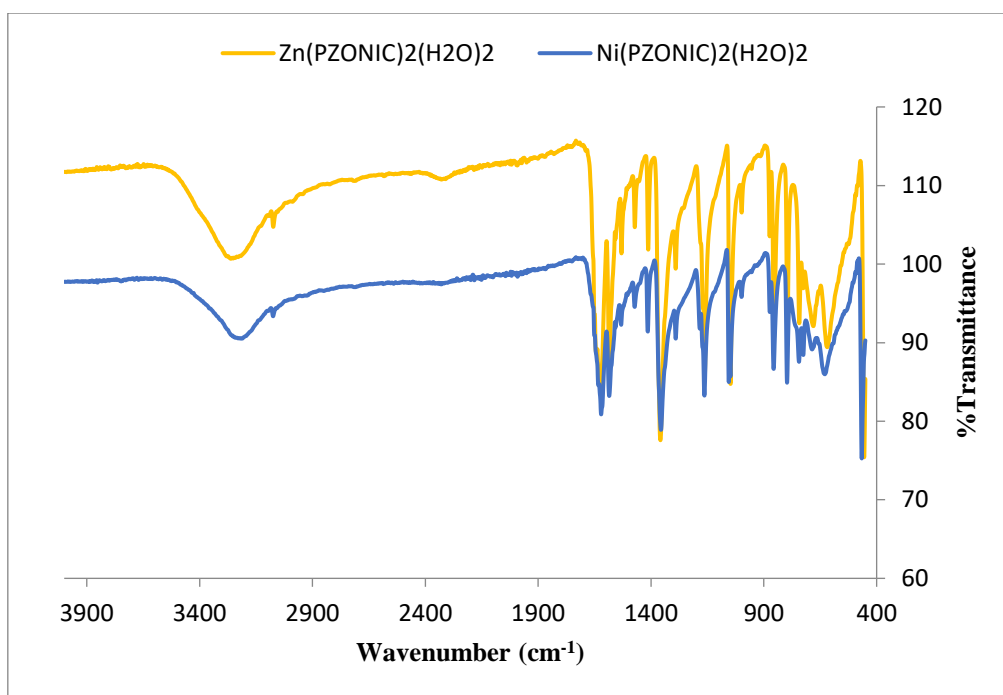


Figure 5.11: The IR spectra of $M(\text{PZONIC})_2(\text{H}_2\text{O})_2$ complexes.

The close resemblance in the spectra of the two complexes is consistent with their established crystal isostructurality.

Table 5.11: FTIR frequencies in (cm^{-1}) and assignments for $M(\text{PZONIC})_2(\text{H}_2\text{O})_2$ complexes

Pyrazinoate ion (PZONIC) in $[\text{Ni}(\text{PZONIC})_2(\text{H}_2\text{O})_2]^{25}$	$\text{Ni}(\text{PZONIC})_2(\text{H}_2\text{O})_2$ (present study)	$\text{Zn}(\text{PZONIC})_2(\text{H}_2\text{O})_2$ (present study)	Assignment
3425	3213	3243	$\nu(\text{OH})$
1585(s)	1586	1585	$\nu(\text{C}=\text{N})$
1660(s)	1621	1623	$\nu(\text{C}=\text{O})$
1290(s)	1289	1291	$\nu(\text{C}-\text{O})$
-	466	455	$\nu(\text{M}-\text{O})$
-	626	604	$\nu(\text{M}-\text{N})$

Comparison of the IR spectrum of free pyrazinoic acid²⁵ with the spectra of the $\text{Ni}(\text{PZONIC})_2(\text{H}_2\text{O})_2$ and $\text{Zn}(\text{PZONIC})_2(\text{H}_2\text{O})_2$ complexes of the present study reveals that on metal complexation considerable changes in frequencies have occurred which can determine

the coordination sites in chelation. The frequencies $\nu(\text{C}=\text{N})$, $\nu(\text{C}=\text{O})$ and $\nu(\text{C}-\text{O})$ for the Ni and Zn complexes are very similar to those listed in Table 5.8 for the corresponding vibrations in $\text{Cu}(\text{PZONIC})_2$, with analogous implications for the mode of ligand coordination. For the Ni and Zn complexes, the broad band spanning the approximate range $3200 - 3400 \text{ cm}^{-1}$ is ascribed to the vibration of OH in the included water molecules.^{25,30} To further support bond formation between the metal and N- and O-donors of the ligand,³¹⁻³³ some moderately intense bands appear in the $400-600 \text{ cm}^{-1}$ region and can be assigned to $\nu(\text{M}-\text{N})$ and $\nu(\text{M}-\text{O})$ [M = Zn, Ni] vibrations.

5.5.2. PXRD

The PXRD patterns of the $\text{Ni}(\text{PZONIC})_2(\text{H}_2\text{O})_2$ and $\text{Zn}(\text{PZONIC})_2(\text{H}_2\text{O})_2$ crystals obtained from the solvothermal syntheses were compared with the respective simulated patterns calculated from the literature data in Figures 5.12 and 5.13. In each case there is very good agreement between experimental and simulated traces. Furthermore, the close resemblance between the PXRD traces of $\text{Ni}(\text{PZONIC})_2(\text{H}_2\text{O})_2$ and $\text{Zn}(\text{PZONIC})_2(\text{H}_2\text{O})_2$ confirms their isostructurality, which had been inferred from a comparison of their unit cell data obtained from single-crystal XRD.

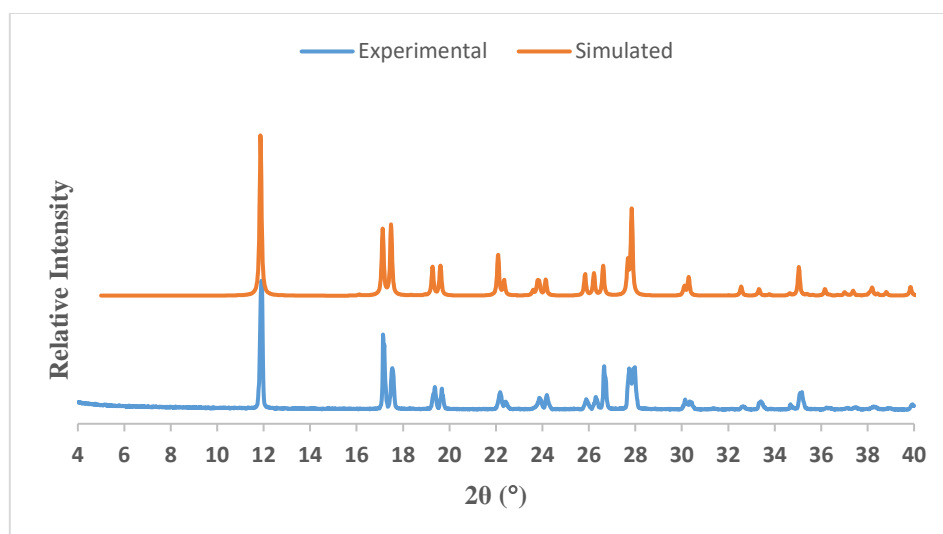


Figure 5.12: Experimental PXRD trace for the complex isolated in the present study and the simulated PXRD trace for $\text{Ni}(\text{PZONIC})_2(\text{H}_2\text{O})_2$.²⁸

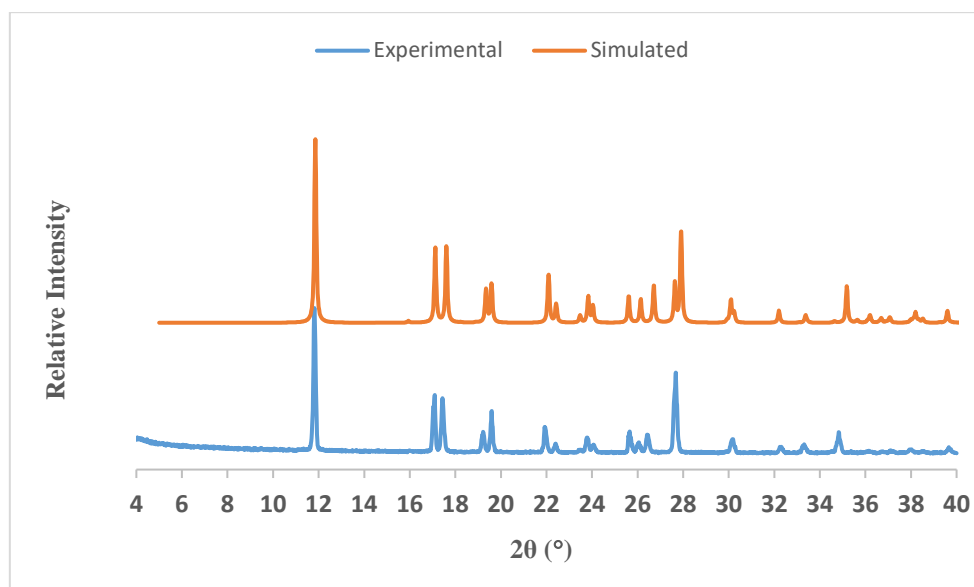


Figure 5.13: Experimental PXRD trace for the complex isolated in the present study and the simulated PXRD trace for $\text{Zn}(\text{PZONIC})_2(\text{H}_2\text{O})_2$.²⁹

5.6 Rationalisation of isolation of unexpected products

The unexpected products obtained in the attempted syntheses of metal-PZA complexes can be attributed to the hydrolysis of PZA to pyrazinoic acid under the harsh reaction conditions employed, namely using the solvothermal method. A similar result was reported when pure PZA was reacted with a water-methanol solution of copper(II) acetate in the presence of 3-nitrobenzoic acid (Figure 5.14), after removal of the initially-produced by-product $\text{Cu}(3\text{-NO}_2\text{bz})_2(\text{H}_2\text{O})_2$ (bz = 3,5-dinitrobenzoate).²²

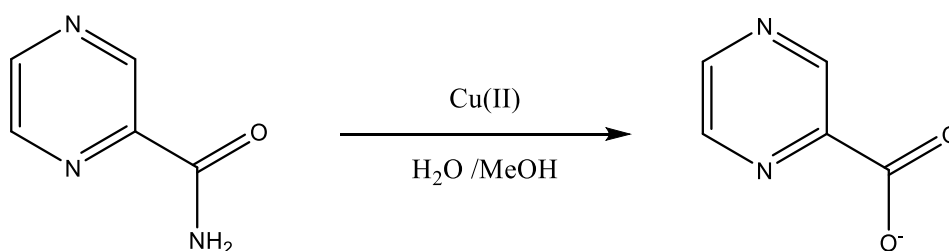


Figure 5.14: Catalytic hydrolytic reaction of pyrazinecarboxamide to pyrazine carboxylate.²²

An analogous hydrolytic reaction was reported to have occurred when pyridine-2-carboxamide underwent prolonged reflux in water in the presence of $\text{Cu}(\text{II})$ ions.²¹

Furthermore, based on the results from our attempted solvothermal synthesis of a Cu-isoniazid complex, where the product unexpectedly contained the isonicotinate ion, we infer that analogous hydrolysis had occurred in that case.

5.6 Conclusion

This chapter provides a summary of the results obtained for the attempted solid-state studies of the Cu-isoniazid, and Cu-, Ni- and Zn-pyrazinecarboxamide complexes.

The study commenced with the use of co-precipitation, refluxing and mechanochemical methods (neat and liquid-assisted co-grinding) in attempts to synthesise Cu, Ni and Zn complexes of a series of anti-tubercular drugs, namely isoniazid, ethambutol, p-amino-salicylic acid, pyrazinecarboxamide and rifampicin. However, despite exhaustive efforts, all experiments resulted in the formation of only physical mixtures of the reactants, as revealed by chromatographic and X-ray diffraction methods. This prompted the use of an alternative procedure, namely solvothermal synthesis, the results of which are summarised below.

Attempted solvothermal synthesis using the various combinations of metal salts and ligands listed above resulted in the formation of unexpected complex products, for which a rationalisation was provided in the previous section.

Experiments using Cu, Ni and Zn salts with isoniazid and pyrazinecarboxamide resulted in the formation of the unexpected complexes $\text{Cu}(\text{ISONIC})_2(\text{H}_2\text{O})_4$ (ISONIC = isonicotinate ion), $\text{Cu}(\text{PZONIC})_2$ (PZONIC = 2-pyrazine-carboxylato ion) and $\text{M}(\text{PZONIC})_2(\text{H}_2\text{O})_2$ where (M = Ni and Zn). These products were fully characterised using elemental analysis, single crystal and powder X-ray diffraction studies, and Fourier transform infrared (FTIR) spectroscopy.

The coordination environment in $\text{Cu}(\text{ISONIC})_2(\text{H}_2\text{O})_4$ as revealed from the X-ray structure shows that Cu(II) coordinates with two isonicotinate ligands and four water molecules, resulting in a distorted octahedral configuration of CuN_2O_4 type. From the hydrogen bond data (primarily O-H...O), it was observed that complex molecules are interconnected in the solid state by five crystallographically unique intermolecular hydrogen bonds, generating a final three-dimensional supramolecular network. The PXRD pattern of the $\text{Cu}(\text{ISONIC})_2(\text{H}_2\text{O})_4$

crystal from the present study was in good agreement with that generated from a previously reported structure determination. The FTIR spectrum reveals the presence of water of crystallisation and the involvement of the pyridine nitrogen atom of the isonicotinate ligand in complexation.

For $\text{Cu}(\text{PZONIC})_2$ the coordination environment around $\text{Cu}(\text{II})$ indicates that the complex displays square-planar geometry, with the ligand acting as bidentate. The FTIR spectrum confirms the coordination of a pyrazine N atom and a carboxylate O atom to the metal centre. The PXRD pattern of $\text{Cu}(\text{PZONIC})_2$ obtained from the experimental sample prepared in the present study and the calculated pattern of the complex structure reported in the literature displayed a high level of agreement, providing convincing evidence of the identity of the two phases.

For $\text{M}(\text{PZONIC})_2(\text{H}_2\text{O})_2$ where $\text{M} = \text{Ni}$ and Zn , the crystal structures are both monoclinic, crystallising in the space group $\text{P}2_1/\text{c}$, with very similar unit cell parameters, and hence they are isostructural. The isostructurality is also established by the close matching of their PXRD patterns.

Based on our finding that attempts to synthesise metal complexes using pyrazinecarboxamide and isoniazid ligands *via* the solvothermal method resulted in complexes containing respectively 2-pyrazine-carboxylato (pyrazinoate) and 2-pyridine-carboxylato (isonicotinate) ligands, it is concluded that such harsh conditions are unfavourable for producing the target complexes.

References:

1. T. Frišćić, *Chem. Soc. Rev.*, 2012, **41**, 3493-3510.
2. D. Paolucci, M. Marcaccio, C. Bruno, D. Braga, M. Polito and F. Paolucci, *J. Organomet. Chem.*, 2005, **24**, 1198-1203.
3. F. Schneider, T. Szuppa, A. Stolle, B. Ondruschka and H. Hopf, *Green Chem.*, 2009, **11**, 1894-1899.
4. A. Bruckmann, A. Krebs and C. Bolm, *Green Chem.*, 2008, **10**, 1131-1141.
5. SAINT, version 7.60a, Bruker AXS Inc, Madison, WI, USA, 2006.
6. G. M. Sheldrick, SADABS, version 2.05, 2007.
7. XPREP, Data Preparation and Reciprocal Space Exploration, version 5.1©Bruker Analytical X-ray Systems, 1997.
8. G. M. Sheldrick, A short history of SHELX, *Acta Crystallogr.*, 2008, **64**, 112-122.
9. L. J. Barbour, *J. Supramol. Chem.*, 2001, **1**, 189-191.
10. Pov-Ray for Windows, Version 3.1e.watcom.win32, The persistence of vision development team, © 1991-1999.
11. K. Nakamoto, *Infrared and Raman Spectra of Inorganic and Coordination Compounds*, A Wiley-Interscience Publication, John Wiley & Sons 1986. ISSN 10: 0471010669.
12. C. Preti, G. Tosi and P. Zannini, *J. Mol. Struct.*, 1979, **53**, 35.
13. Cambridge Structural Database and Cambridge Structural Database System, Version 5.38 (May 2017 update), Cambridge Crystallographic Centre, University Chemical Laboratory, Cambridge, England, 2016.
14. K. Waizumi, M. Takuno, N. Fukushinma and H. Masuda, *J. Coord. Chem.*, 1998, **44**, 269-279.
15. A. L. Spek, PLATON, A Multipurpose Crystallographic Tool, Utrecht University, Utrecht, The Netherlands, 2008.

16. M. Almasi, Z. Vargova, R. Gyepes, R. Varga and V. Zelenak, *J. Inorg. Chem. Commun.*, 2014, **46**, 118-121.
17. P. Budhani, S. A. Iqbal, S. M. M. Bhattacharya and L. Mitu, *J. Saudi Chem. Soc.*, 2010, **14**, 281-285.
18. Y. Liang, L. Li and N. Xu, *Synth. React. Inorg. Met. Org. Chem.*, 2013, **43**, 96-101.
19. Molecular Structure and Dimensions, Interatomic Distances, N. V. A. Oosthoek's Uitgevers Utrecht, Vol. A1, 1960-1965.
20. M. Sekizaki, *Acta Cryst.*, 1973, **B29**, 327.
21. P. Segla, M. Jamnicky, M. Koman, and T. Glowiak, *Polyhedron*, 1998, **17**, 4525-4533.
22. Z. Vaskova, Z. Padekova, M. Mazur, D. Valigura and J. Moncol, *Transit. Metal Chem.*, 2001, **36**, 883-889.
23. H. J. M. Bowen, J. Donohue, D. G. Jenkin, O. Kennard, P. J. Wheatley and D. H. Whiffen, *Spec. Publ. Chem. Soc.*, 1958, **11**, M18.
24. C. J. Connor, C. L. Klein, R. J. Majeste and L. M. Trefonas, *Inorg. Chem.*, 1982, **21**, 64-67.
25. S. M. Y. El-Medani, O. A. M. Ali, H. A. Mohammed and R. M. Ramadan, *J. Coord. Chem.*, 2005, **58**, 1429-1437.
26. M. R. Maurya, S. Sikarwar, T. Joseph, S. B. Halligudi, *J. Mol. Catal. A: Chem.*, 2005, **236**, 132-136.
27. G. B. Barlin, *The Pyrazines: The chemistry of heterocyclic compounds*, Vol. **41**. John Wiley & Sons, New York, 1982, p.372.
28. J. Jing, L. Dan, L. Lei, F. S. Zhong, L. Dongwei, N. Shuyun and Z. Guangning, *Acta Chim. Sinica*, 2011, **69**, 2108-2116.
29. X. Hu, Y. P. Li, Y. J. Wang, W. J. Du and J. X. Guo, *J. Chem. Crystallogr.*, 2010, **40**, 846-851.

30. P. Koczon, J. Piekut, M. Borawska, W. Lewandowski, *J. Mol. Struct.*, 2003, **651**, 651-656.
31. H. A. Tajmir-Riahi and D. M. Boghai, *J. Inorg. Chem.*, 1982, **45**, 73-84.
32. K. Nakamoto and A. E. Martel, *J. Chem. Phys.*, 1960, **32**, 588-597.

Chapter 6

Concluding Remarks

6.1 Conclusion

The significant role of metals and the recognition of their complexes as important bioactive compounds *in vitro* and *in vivo* has aroused an ever-increasing interest in these agents as potential drugs for therapeutic intervention in various diseases.

This study was undertaken to develop metal complexes of anti-tubercular drugs with improved solubility and absorption properties. A high rate of absorption for improved bioavailability of these drugs is necessary for efficacy against resistant TB strains. In the present study, Cu(II), Ni(II) and Zn(II) complexes of a series of anti-tubercular drugs, namely isoniazid (ISO), ethambutol (EMB), p-aminosalicylic acid (PAS), pyrazinocarboxamide (PZA) and rifampicin (RFN) were studied with the aim of increasing their lipophilicity and permeability.

Bioavailability is an essential measurement tool since it determines the correct dosage for administration of a drug. It refers to the degree and rate at which an administered drug is absorbed by the body's circulatory system. For metal ions, there is the added complication that the bioavailability depends on the speciation or distribution of the metal ion amongst all possible species in solution. It is not possible to measure the metal ion speciation *in vivo* because the number of such species is so large and their concentrations are often below the detectable limits of modern analytical chemistry. However, knowing the thermodynamics, reflected in the equilibrium constants for the metal ion - ligand interactions, it is possible to calculate the speciation under steady-state conditions.

The protonation/deprotonation constants and the equilibrium of the ligand and metal-ligand complexes were measured in aqueous solution at $25 \pm 0.01^\circ\text{C}$ and an ionic strength of 0.15 M (NaCl) using glass electrode potentiometry. The measured protonation constants for ISO were 3.67 and 10.95, and these constants correspond to the protonation of the pyridine nitrogen and the hydrazide group. The equilibrium constant for the deprotonation of CuISOH ($\log \beta_{\text{MLH}^-}$

$\log \beta_{\text{ML}} = 13.77 - 8.98$) was determined as 4.79. This value is similar to the pK_a of pyridine (5.21) which suggests that it is the pyridine that is deprotonated to form ML from MLH. Thus, CuLH is formed by the coordination of the isoniazid carbonyl oxygen and hydrazide amino nitrogen atoms, while the pyridine group is protonated.

The $\log \beta$ value for CuISO is 8.98, which is much higher than the stability constants of $[\text{Cu(II)(NH}_3\text{)}]^{2+}$ (4.8), $[\text{Cu(II)(pyridine)}]$ 2.49, and $[\text{Cu(II)(benzylhydrazide)}]$ 1.73, suggesting that the ligand is not monodentate. The $\log \beta$ value is quite close to that of $[\text{Cu(II)(en)}]^{2+}$ (10.5) suggesting that the ligand has a similar binding mode. The stability constants ($\log \beta$ values) of ML species of ISO with Cu(II), Ni(II) and Zn(II) are 8.98, 4.92 and 5.50 respectively. The difference in stability of some 3.5-4.0 log units is observed between Cu(II) and the *in vivo* competitors Ni(II) and Zn(II). The explanation for this observation is that the arrangement of the ligand donor atom is such that the Cu(II) ion is constrained to adopt a square-planar coordination geometry and Zn(II) prefers a tetrahedral coordination geometry, as observed in most simple systems and metalloenzymes.

In the deprotonation of ML to form MLH₋₁, for Ni(II) and Zn(II), the calculated pK_a ($\log \beta_{\text{ML}} - \log \beta_{\text{MLH-1}}$) values were 8.96 and 7.60. These values are 0.90 and 1.57 log units lower than the first hydrolysis constant of Ni(II) ($pK_a\text{-OH}$) = 9.86 and Zn(II) ($pK_a\text{-OH}$) = 9.17 respectively. This suggests that the deprotonation comes from a coordinated water molecule in the complex.

EMB has been found to take up two protons in the pH range 2-11. The two pK_a values of 6.52 and 9.63 arise from the two amino nitrogen groups. The $\log \beta$ value for ML in Cu(II) EMB (10.4) and $[\text{Cu(II)(en)}]^{2+}$ (10.5) are similar, suggesting similar binding modes. A noticeable feature about the complexation of EMB with Cu(II), Ni(II) and Zn(II) is the prevalence of the ML species. The difference in the stability observed between the metal ions with EMB was 3-4 log units, and the trend agrees with the Irving-Williams stability order for transition-metal

complexes. The $\log \beta$ value of ML_2 (15.42) compares well with that for $[Cu(II)(en)_2]^{2+}$, namely 15.9, again suggesting a similar coordination mode. The ML_2 can coordinate through the two amino nitrogen atoms from the two ligands. The calculated Cu(II)-assisted deprotonation constants associated with the formation of ML_2H_{-1} and ML_2H_{-2} are 8.77 and 10.01 respectively. The deprotonation could be due to loss of protons from coordinated water molecules since the pK_a is close to the hydrolysis constant of $[Cu(OH_2)_6]^{2+}$.

P-aminosalicylic acid displays two pK_a values of 3.78 and 1.85 arising from the carboxylic acid group and the amino group respectively. The value of the equilibrium constant for the deprotonation reaction of CuPASH ($\log \beta_{MLH} - \log \beta_{ML} = (5.59 - 2.21) = 3.38$), suggests that the amino nitrogen is protonated in the formation of MLH. The deprotonation of ML leads to the formation of MLH_{-1} with a pK_a of 4.96. The deprotonation occurs at a much lower pH than the deprotonation of the phenolic OH group of the free ligand, suggesting a metal ion - induced proton loss.

The protonation constants of rifampicin (RFN) and pyrazinecarboxamide (PZA) could not be detected under the conditions of our experiment. The metal complex species of ISO, EMB and PAS showed significantly different coordination behaviour at physiological pH.

Since the distribution of the species has been determined from the potentiometric result, it is important to ascertain the structure of the complexes using UV-Visible spectroscopy. The maximum wavelength (λ_{max}) and the absorptivity (ϵ) of different metal-ligand complexes in solution were used to predict the structures of complexes of EMB with Cu(II) and Ni(II) and those of ISO and PAS with Cu(II). The visible spectra obtained are typical of Cu(II) in a distorted octahedral environment, and the molar extinction coefficients are also typical of Cu(II) complexes and reflect the distortion of the metal-ion environment. The Ni(II) EMB spectra display a shift of the complex from octahedral to square-planar.

The λ_{\max} value for CuISOH (746 nm) is similar to that for [Cu(NH₃)(OH₂)] (745 nm), suggesting that the amine nitrogen atom of ISO is coordinated to the copper, which means that the pyridine nitrogen atom is protonated. The experimental λ_{\max} values and molar extinction coefficients for ML and MLH₋₁ are estimated as 743 nm, 28.33 dm³ mol⁻¹ cm⁻¹ and 736 nm, 8.35 dm³ mol⁻¹ cm⁻¹ respectively.

In the UV-spectrum of CuPAS, there is a decrease in the λ_{\max} value of MLH₋₁ when compared to ML, which can be attributed to deprotonation of the phenolic OH group of the coordinated ligand. For this to occur at such a low pH, the metal ion must be involved in a metal ion - induced proton loss, resulting in the spectral change. The results of the spectroscopic studies are in agreement with the proposed structure from the potentiometric results.

Knowing that metal complexes of ISO, PZA, PAS and RFN are stable and having some idea as to the structures of the complexes, it is important to study their permeability and bioavailability. Partition coefficients are often used as an indication of tissue permeability as they are easier to measure than membrane permeability using a Franz cell. This method measures the ratio of the concentration of metal-ligand complexes in the lipid phase (octanol) to their concentration in the aqueous phase (water). The partition coefficients of ISO and PZA, as well as those of their metal complexes, have log values below zero, indicating that the ligands and their complexes are hydrophilic. The values of log $P_{\text{oct/aq}}$ for PAS and RFN and their metal complexes are positive, signifying that they are lipophilic.

One of the objectives of the study was to develop metal complexes that could improve the bioavailability of the parent drugs. This was evaluated by measuring the effect of the metals on the rate of diffusion of the ligands through Cerasome, an artificial membrane as a model for the skin, using a Franz cell. The presence of Cu(II), Zn(II) and Ni(II) metals enhanced the permeation of ISO through the artificial membrane, while zinc improved the permeability of

PAS with an enhancement ratio of 2. The presence of Cu(II), Zn(II) and Ni(II) did not affect the permeability of PZA. Cu(II) improved the permeability of RFN 20-fold.

Potts and Guy¹ have developed an empirical relationship between $\log P_{\text{oct/aq}}$, $\log K_p$ and size (MW) of a drug. We tested this relationship with our results and found that the multiple linear regression analysis of $\log K_p$ upon $\log P_{\text{oct/aq}}$ and MW gave an R^2 value of 0.77, which means that there is a correlation between $\log K_p$ and $\log P_{\text{oct/aq}}$ or MW .

The average value of the intercept diffusivity $\log (D^0/h)$, the constant which accounts for the difference between the partitioning domain presented by octanol and the membrane lipids (f), and conversion factor for the substitution of molecular weight for molecular volume (β') found in the present studies were 0.26, 0.76 and 0.00078 respectively. These values were compared to the values of $\text{Log}(D^0/h)$ (-2.72), f (0.71), and β' (0.0061) values obtained by Flynn for 90 drugs.² The diffusivity of these charged complexes of the present studies are higher than expected and f is similar as the charge of the complex has a similar effect on the octanol and membrane partitioning. This further supports the conclusion that for a labile drug and its complexes, factors other than size and partition coefficient are significant.

Since intravenous (IV) administration requires trained personnel, anti-TB drugs are usually administered in tablet form. For this reason, efforts were made to synthesize the metal complexes of the drugs in solid form. Techniques which included co-precipitation, refluxing and mechanochemistry (neat and liquid-assisted co-grinding) were employed in an attempt to synthesise Cu(II), Ni(II) and Zn(II) complexes of the chosen series of anti-tubercular drugs. However, upon analysing the products of the experiments using chromatographic and X-ray diffraction methods, it was observed that the products obtained were all physical mixtures of the starting materials. This prompted the use of the solvothermal method as an alternative synthetic technique. The syntheses *via* this method for the targeted metal complexes of

isoniazid and pyrazinecarboxamide resulted in the formation of complexes containing 2-pyrazine-carboxylato (pyrazinoate) and 2-pyridine-carboxylato (isonicotinate) ligands respectively. It was therefore inferred, based on the probable mechanism of transformation, that the solvothermal method is unfavourable for obtaining the target complexes.

The overall results of this study are encouraging and merit further evaluation of metal ions to improving the lipophilicity and permeability of anti-tubercular drugs. It is hoped that this study has contributed to the understanding of some aspects and factors involved in the development of metal complexes for improving absorption of anti-tubercular drugs.

References:

1. R. O. Potts, R. H. Guy, *Pharm. Res.*, 1992, **9**, 663–669.
2. Dermal Exposure Assessment: Principles and Applications, United States Environmental Protection Agency, EPA Interim Report, EPA/600/8-91/011B, January 1992.